Electromagnetic Modelling for the Active and Passive Remote Sensing of Polar Ice Sheet and Signal of Opportunity (SoOp) Land Observation

by

Haokui Xu

A dissertation submitted in partial fulfillment
of the requirements for the degree of
Doctor of Philosophy
(Electrical and Computer Engineering)
in the University of Michigan
2024

Doctoral Committee:

Professor Leung Tsang, Chair
Assistant Professor Aline Eid
Professor Amir Mortazawi
Professor Chris Ru

Haokui Xu
xuhaoku@umich.edu

ORCID iD: 0000-0002-5924-8903

To my family and dear friends

Acknowledgments

I would like to express my sincere gratitude to my advisor, Prof. Leung Tsang, for his invaluable support and guidance throughout the research and writing of this thesis. His expertise, constructive feedback, and unwavering commitment have been instrumental in shaping and refining this dissertation.

I am also deeply thankful to Prof.Chris Ruf, Prof. Amir Mortazawi, and Prof. Aline Eid for serving on my dissertation committee and providing valuable suggestions to improve the thesis.

I want to acknowledge the scientific community to which I belong. The projects supported me financially enriched my life and mind, and the researchers offered me an agreeable friendship rooted in similar scientific goals and interests. Thank you to all those scientists and engineers who shared their insightful thoughts, invaluable data, and incentive encouragements with me. To name a few, I express my deepest appreciation to Prof. Joel T. Johnson and Prof. Kenneth C. Jezek from Ohio State University, Dr. Xiaolan Xu, Dr. Seung-Bum Kim, Dr. Simon H. Yueh, Dr. Rashmi Shah, and Dr. Son. V. Nghiem, from Jet Propulsion Laboratory, Dr. Steven Margulis from UCLA, Dr. Marco Brogioni and Dr. Giovanni Macelloni from the “Nello Carrara” Institute of Applied Physics (IFAC) of the National Research Council (CNR), Italy, Dr. Brooke Medley from the Goddard Space Flight Center.

I extend my heartfelt appreciation to my friends, who have been a constant source of encouragement and support throughout this academic journey. Your friendship has strengthened me during challenging times and made the joyous moments more memorable. Thank you for your understanding, laughter, and the countless ways you've enriched my life. Your presence has been

a cherished gift, and I am grateful for the camaraderie that has made this experience all the more fulfilling. Those include a list of people from my research group: Dr. Jiyue Zhu, Dr. Shurun Tan, Dr. Tai Qiao, Mr. Joonwoo Jeong, Mr. Firoz Borah, Ms. Ruoxing Gao, and Mr. Zhenming Huang. A group of people from EECS: Dr. Han Guo, Mr.Wenhao Peng, Mis. Ruiying Chai, Mr. Kaleo Roberts, and Mr. Aditya Varma. I want to thank the people who are always there to help: Dr. Yuting Gao, Mis. Fangjun Hou, Dr. Haolv Shang, Dr. Qicang Shen, Dr. Menglou Rao, Dr. Xin Zan, Mis. Ruiying Chai, and Mis Liang Yao.

Last but not least, I am mostly grateful for the love I received from my family. Without their lover and support, nothing is possible.

Table of Contents

List of Tables

List of Figures

Abstract

Climate has been changing dramatically over the past several decades. Terrestrial snow and polar ice sheets have been studied intensively as indicators of climate change. The following research supports two major objectives. The first objective is to use a new microwave remote sensing technique, P-band GNSS-SAR interferometry, to characterize the Snow Water Equivalent of Terrestrial. The second objective is to assist in estimating polar ice sheet mass balance using active and passive microwave remote sensing data.

To support the GNSS-SAR remote sensing of terrestrial snow, my research focused on simulating the P-band near specular bistatic scattering coefficients of mountainous areas. Given that reliable measurement of the near specular scattering coefficients of land surface in the P-band Signal of Opportunity concept will only be available in the future, simulation work is currently the only way to understand the near specular bistatic scattering in the P-band. The bistatic scattering coefficient of variance fields, denoted by γ_v, is calculated at various scattering azimuth angles. Simulations using AKS show that the $\boldsymbol{\gamma_v}$ can exceed 10 dB across a range of azimuth angles, $\boldsymbol{\phi_s}$. The values are much larger than those of radar backscattering, suggesting potential support for employing a Synthetic Aperture Radar (SAR) concept based on Signals of Opportunity, particularly with data acquisition near the forward direction. The much stronger surface scattering ability loosens the requirements of receiving antenna gain. Large swath sensing of terrestrial snow is thus possible.

Two subtopics are covered in my research to support the mass balance study. The first subtopic involved the density variation properties in the dry zone, while the second subtopic focused on the modeling work for the perennial firn aquifer.

Fluctuation of firn density near the surface is a major uncertainty in characterizing mass balance. Previous research has shown that firn density profiles can be represented using three processes: “long” and “short” length scale density variations and “refrozen layers”. My research shows that the short and long-scale firn processes can be modeled as 3D continuous random medium with finite vertical and horizontal correlation lengths. I also showed that there are refrozen layers in the firn, the number of which can be determined by radar echograms. The density parameters used for the long-scale profile to match the UWBRAD brightness temperature measurements are consistent with those from CFM modeling. Our model predictions also explain SMOS's V and H-pol multi-angle measurements at Dome-C, Antarctica. This work demonstrates that co-located active and passive microwave measurements can infer polar firn properties, which are important in characterizing the mass balance of the polar ice sheet.

In my research, a Full wave simulation approach at the L-band was used to characterize the effective permittivity as a function of liquid water content. At the same time, a radiative transfer model was implemented to relate the brightness temperature observed by SMAP with the liquid water content in the firn aquifer. Bi-continuous media-modeled aquifer structures show a different permittivity prediction from the classical mixing formulas. A radiative transfer model based on 3D density characterization explains the V/H pol data with a single set of parameters. The modeling work will help characterize liquid water content in firn aquifer and the hydrology study in the polar ice sheets. Eventually, the research will benefit the evaluation of the effects of aquifers on ice sheet mass balance.

Chapter 1 Introduction

The research has two ultimate objectives. For the first one, the ultimate goal is to use a new microwave remote sensing technique, GNSS-SAR, working in the P-band to characterize the Snow Water Equivalent of Terrestrial by interferometry. At the P-band, the scattered signal from the snow-covered ground is mostly from the land surface (Snow-land interface). Given a required Signal Noise Ratio (SNR) and transmitter power density, the product of radar cross-section of land surface and Antenna gain is a fixed number. As a result, modeling for the land surface scattering using measured profile data provides a valuable reference for the design of antennas before the ground measurement campaign data is available. The simulations can also help validate the model once the ground campaign is done. For the second objective, the goal is to help estimate polar ice sheet mass balance using microwave remote sensing data. Research for this objective focuses on density fluctuations in the dry zone and firn aquifer water content in the percolation zone. The dry zone of the ice sheet refers to the inner part of the ice sheet away from the coast, where melting in summer is rare. The property of density fluctuations is a quantity that affects the retrieval of the ice sheet temperature profile, an important parameter for the stability and stiffness of the whole ice sheet. These properties are also related to the accumulation process of the ice sheet, which determines its density profile. Density profiles are important for the mass loss evaluation. With the knowledge of firn density, elevation change measured by satellite missions(e.g., ICESTAT-2 laser altimetry) can be directly related to mass change. Firn aquifer is a layer of ice and water mixture existing in part of the percolation zone where melting happens every summer. This phenomenon

happens on the polar ice sheets due to a warmer climate. The aquifer is believed to accelerate the mass loss from polar ice. Still, quantitative analysis of how much it contributes to the acceleration could not be performed without the knowledge of aquifer hydrology. The liquid water content of the firn aquifer is one of the fundamental parameters that need to be quantitatively characterized over Greenland for a better understanding of the aquifer hydrology. Time series data from microwave radiometer has shown sensitivity to the existence of aquifer. A physical model is developed to interpret radiometer data.

1.1 Modeling near specular bistatic scattering for P-band SoOp land observations

Microwave remote sensing at P-band (216~415 MHz) can be used to retrieve root zone moisture [1], biomass [2],[3], snow water equivalent [4], and polar subsurface temperature [5]. The BIOMASS mission of the European Space Agency provides a resolution of 200 m using a P-band synthetic aperture radar (SAR) with the potential to measure biomass and root zone moisture.

However, the use of space-borne P-band radar for remote sensing over North America and most of Europe is restricted since the P-band remote sensing radar will inevitably interfere with the performance of US Space Objects Tracking Radar, which has been designated as the primary user of 435MHz band.

The proposal to use GNSS signals to perform scatterometry was first made in 1988 [6]. Five years later, GNSS-Reflectometry (GNSS-R) was used for mesoscale ocean altimetry [7]. The first experiment demonstrating ocean-surface wind sensing by GNSS-R was reported in 1998 [8]. In recent years, Signals of Opportunity (SoOp) has gained popularity because of the lower cost of using transmitters on existing navigation and communication satellites. For example, GPS, GLONASS, and Beidou are the GNSS satellites used as transmitters in the L band. Satellites with receivers have been launched to measure the reflected signals from the earth's surface in the specular

direction. At the L-band, the Global Navigation Satellite System Reflectometry (GNSS-R) has been extensively used since the launch of Techdemosat-1(TDS-1) by the U.K. in 2014[9].

Other GNSS-R missions include the Cyclone Global Navigation Satellite System (CYGNSS) [10], launched by NASA in 2016, Bufeng [11], launched by China in 2019, and Hydro-GNSS-R to be launched by Italy [12]. GNSS-R data have been applied to the retrieval of ocean wind speed [13], sea ice thickness [14,11], and monitoring wetland changes [15,12], and soil moisture [16]-[18]. Machine learning methods have also been applied to retrieve geophysical parameters [19]. However, the resolution of the GNSS-R systems is typically 20 to 30 km due to the bandwidth limits in both signal and Doppler shift. In addition, the L-band signals are strongly attenuated by the vegetation and forest coverage.

A SAR concept based on SoOp in P-band has been proposed [20] that utilizes the signal from the Mobile User Objective System (MUOS) [21]. MUOS has four operating satellites at geosynchronous altitudes, broadcasting at two frequencies (360-380 MHz and 240-270 MHz) within P-band. With a constellation of low earth orbit-based receivers, a high resolution of 100 m can be achieved [20]. The strength of bistatic scattering coefficients of land surfaces is crucial to achieve an adequate Signal Noise Ratio (SNR) for the P-band SoOp SAR. The land surface scattering needs to be studied to retrieve snow water equivalent (SWE) in mountainous terrain where seasonal snow resides. The measurements utilize an interferometric method through the phase difference of snow-free and snow-on conditions. Unlike classical GNSS-R systems, the SAR concept would also need the knowledge of bistatic scattering off the specular direction, usually in the azimuthal scattering direction.

In our previous reflectometry studies of land surfaces at L- band [22], we decomposed land surfaces into three spatial scales. The smallest scale (f_1) is random and has a scale with a typical

root mean square (rms) height under 4 cm and a correlation length several times the rms height. The largest scale (f_3) is around 30 meters. The f_3 is deterministic and is planar with well-defined slopes in both x and y directions. An intermediate scale (f_2) is used to bridge the gap. In this paper, we use Lidar measurements [23] with a typical spatial resolution of 3 meters to provide a characterization of f_2 . For the present case of P-band with a wavelength(81cm) much larger than $f_1(h_1 < 4cm)$ we ignore f_1 in this study.

The rough surface and topography effects on GNSS-R data at L-band have been studied by the Geometric Optics(GO) method [24-27], the Improved GO method [28], and the SAVERS model [29]. We have also developed two methods: (i) NKA (Numerical Kirchhoff Approach) [30] and (ii) AKS (Analytic Kirchhoff Solution) [22]. Inter-comparison studies have also been made on these methods [31].

Major differences exist in rough surface scattering between radar (monostatic) backscattering and the forward (bistatic) scattering used in reflectometry. The scattering geometry for radar backscattering and near specular scattering and GNSS-R near specular scattering are presented in Figure 1-1(a) and (b), respectively. The former has a large difference in horizontal k vector between the incident direction and the return direction, which is opposite to the incident direction [22,24]. The contributions of monostatic radar come primarily from diffuse scattering due to rough surface features smaller than or comparable to the wavelength. In the case of reflectometry, the bistatic scattering direction is near the specular direction. At a 40-degree incidence angle, the radar cross-section of a rough surface in the vicinity of the specular direction is expected to be much larger (~20 dB) than for backscattering in the L-band, which is typically in the range of -10 to -20 dB). As shown in previous L band studies [31], topography and random roughness strongly influence the radar cross sections in reflectometry.

To investigate the characteristics of surface scattering at the P-band near the vicinity of

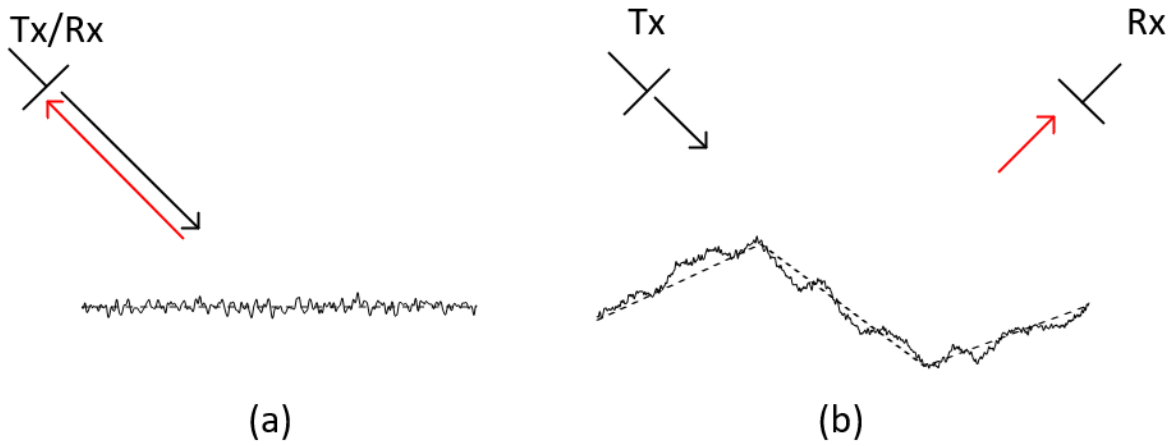

Figure 1-1 Geometry of observation for classical radar backscattering(a) and GNSS-R near specular scattering(b). The classical radar backscattering observes the scattered wave from a single roughness on a horizontal plane. For the GNSS-R observations, instead of collecting the scattered field in the backscattering direction, the receiver collects fields in the near specular direction. Different from the radar backscattering case, the scattered field collected by the receiver is also affected by the topography of the land surface, along with the random roughness.

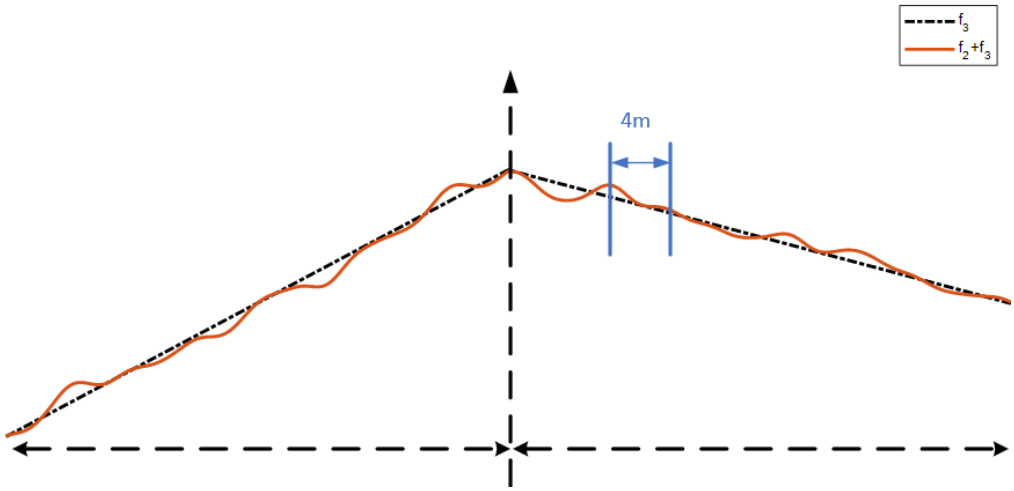

Figure 1-2 Profile of $f_2 + f_3$. f_3 profile represents the topography of the surface, while f_2 represent the random rough profile mounted on the topography.

specular direction ($\phi_s \; from \; 0 \; to \; 10 \; degs$), in the context of mountainous terrain as represented in Grand Mesa, Colorado, NKA[30] and AKS[22] are applied. The investigation performed for other specular azimuthal angles is much larger than the usual GNSS-R system. We use Lidar data collected during the NASA SnowEx 2020 project [23] to derive f_2 and f_3. The properties of f_2

and f_3 are used for the input of Kirchhoff models. Figure 1-2 shows the combined profile of $f_2 + f_3$.

Kirchhoff approximation uses the local incident and reflected field to approximate the electric and magnetic field on the rough surface. The scattered wave is then calculated using Huygens's principle. In both Kirchhoff methods, f_2 is considered a random profile, while f_3 is considered deterministic. As shown in Figure 1-2, f_2 is mounted on the tilted planar patches(f_3). Effects of f_2 and the tilting of f_3 are both included in the modeling. In NKA, the integral in Huygens' principle is calculated over the specific profile of a random rough surface with a discretization of $\frac{1}{10}\lambda$. Due to the random nature of the rough surface realization, the scattered field calculated through NKA will inevitably fluctuate. The Monte Carlo method is used to smooth out the fluctuations. On the other hand, the Analytical Kirrchhoff Solution performs the averaging through the rough surface's statistical properties (rms height and correlation function) analytically. Due to the different methods used in averaging, NKA is much slower than AKS but can be used as a benchmark to validate the correctness of AKS. AKS is used to simulate the near specular scattering over the land surface.

Lidar data provides a measurement of surface heights over the Grand Mesa area. The Lidar data is used to extract the statistical properties, namely the rms heights and correlation functions, which serve as input parameters to the AKS.

The incoherent scattering coefficients are evaluated according to different resolution sizes by averaging the incoherent scattering coefficients for several f_3 patches within the particular resolution. Coherent scattering needs to be evaluated according to specific instrument parameters; thus, it will not be discussed in this study. Simulation results show that the AKS and NKA results agree with each other. We will illustrate the simulated bistatic scattering coefficients over Grand

Mesa over a range of azimuthal angles. The bistatic scattering is found to be of significance.

1.2 Radiative transfer modeling for the ice sheet emission with 3-D density variations

Over the entire twentieth century, the global mean sea level has increased by approximately 1.5mm yr^{-1}[32-36]. Since the 1990s, a significant acceleration in the rise of sea level has been observed[37,38]. In the study of climate change, the mass balance of polar ice sheets stands as a major topic, given its crucial role in estimating current mean sea level changes, which is primarily attributed to their status as the largest contributors. [39,40]

The most recent assessment of the mass balance of the Greenland and Antarctic Ice sheets confirmed a loss of ice to the ocean at a rate of 320 Gt/year, equivalent to a 1 mm sea level rise yearly since 2003 [40]. The quantification of uncertainty in ice-sheet volume change between NASA's first- and second-generation Ice, Cloud, and land Elevation Satellites (ICESat, ICESat-2) is a testament to the precision of these laser altimeters. For example, uncertainties for the grounded AIS and GrIS are currently ~5 and 3 km^3 yr-1, respectively, compared to volume changes of -111 and -235 km3 yr-1[40]. Currently, the largest source of uncertainty in altimetry measurements of mass balance stems from the volume-to-mass conversion within which firn processes dominate [40,41].

When snow falls on the ice sheet, it slowly densifies into solid ice with increasing depth in a manner that is dependent on the pressure imparted by subsequent snowfall, the physical temperature, and any refreezing of infiltrated liquid water. The resulting transitional material is referred to as firn. Firn typically ranges in thickness from 10's to >100 meters over ice sheets [42,43]). The density of the firn column at a given location varies in response to short and long-term-scale variations. Because the material density of the firn column is much less than that of solid ice[40,44], its thickness variations often manifest as a much larger portion of the total column

thickness change than ice dynamic change. For instance, yearly snowfalls cause fluctuations in firn density profiles at various depths[45]. As depth increases, the fluctuation amplitude becomes smaller and more rapid because of densification effects.

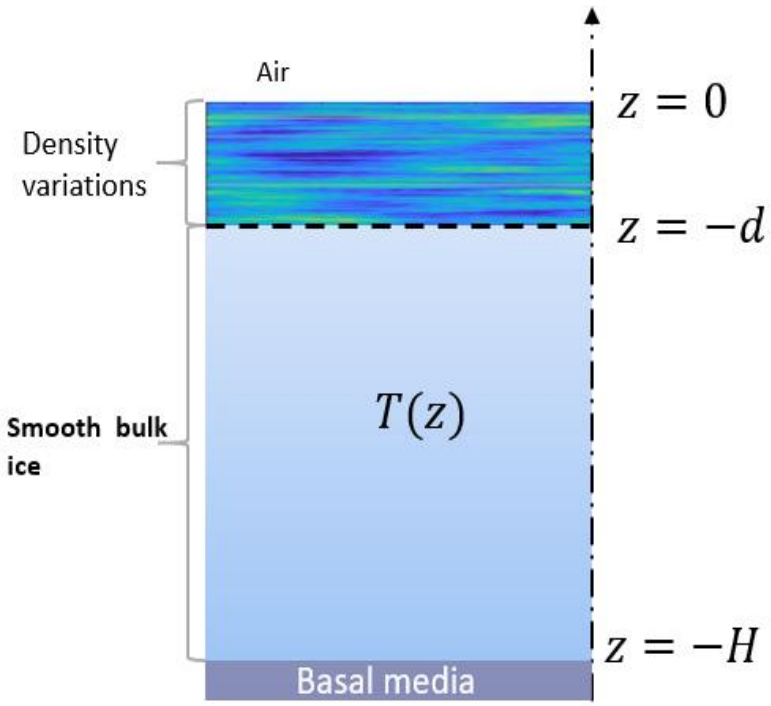

Figure 1-3 Characterization of polar ice sheet with 3-D density variations.

Because of the large spatiotemporal variations in firn column properties, it can be extremely difficult to measure at the spatial scales required to support detailed modeling efforts. In situ measurements of the firn depth-density profile exist sporadically across both ice sheets in time and space [46]. While these observations provide a snapshot of firn properties, direct evidence of their evolution through time at sufficient resolutions applicable to altimetry studies (seasonally) remains a major challenge. Modeling efforts have filled some of these knowledge gaps [47, 43]. Still, their ability to realistically simulate firn processes remains incompletely understood without extensive in-situ observations.

Active and passive microwave sensors can also inform us about the scattering and emission properties of the firn over large scales [48-51]; these properties are ultimately related to the physical properties of the firn. For example, the strongest echoes in a radar echogram show the positions of abrupt permittivity changes that usually correspond to the positions of refrozen melt layers [52 53]. Several studies have used active microwave remote sensing to track the firn's internal stratigraphy (radar reflection horizons related to density contrasts) to infer spatiotemporal variations in snow accumulation rates [54 -57]. Although radar echoes can position internal firn layers, using the radar data only to study firn densification quantitatively remains challenging.

Passive microwave brightness temperature measurements in the 0.5-2 GHz range can also reflect the effects of internal density fluctuations [58 59]. In our previous work, Ultra-Wide Band software defined RADiometer (UWBRAD) was used to sense the subsurface temperature profile, in which case the reflections caused by firn density fluctuations are nuisance effects [60]. Unlike radars, which observe scattered powers only in the backscattered direction, radiometer brightness temperature observations are sensitive to scattering in all scattering directions within the firn, as Kirchhoff's Law shows [61].

We use co-located Snow Radar echoes (acquired in Greenland during the Operation Ice Bridge Campaign 2017, [62] and 0.5-2 GHz brightness temperature data (the latter collected by UWBRAD in 2017) to evaluate firn density fluctuations in the Greenland ice sheet quantitatively. Since high-resolution measurements are not available, the firn density properties derived from microwave sensor data in Greenland are compared with simulated profiles from the Community Firn Model (CFM). The CFM simulated profiles are first evaluated by comparing them to in-situ measurements. A radiative transfer model with 3D density variation effects is implemented to interpret the measured brightness temperature. The problem is described in Figure 1-3. Unlike the

one-dimensional stochastic profiles used in previous brightness temperature modeling studies [63,59], a horizontal correlation length, l_ρ, is introduced for the short (due to temporal effects) and long-scale (due to yearly snow fall) processes to represent their variations in horizontal directions. This approach results in a continuous random medium description of the firn instead of the past stochastic layered medium description. "Refrozen layer" effects (high or low-density density discontinuities) were also not included in [63,59] but are included.

The model then shows the effects of the long-scale and refrozen layers to be significant, while those of the short-scale process are negligible, and the impact of the long-scale process depends on the microwave frequency. The number of freezing layers and their positions used in the model are determined from Greenland radar echo data. The results also show that freezing layers introduce a frequency dependence in 0.5- 2 GHz brightness temperatures that differs from that of the long-scale process.

The developed model also suggests combining active and passive microwave measurements to sense properties of firn density profiles in areas lacking in situ measurements. The method first estimates the number and location of freezing layers using radar echo measurements. The impact of these layers is then removed (based on the partially coherent model), and properties of the long-scale density fluctuations are estimated by matching model predictions to 0.5-2 GHz measured brightness temperatures. Results suggest that the long-scale vertical correlation length can be estimated this way.

The H and V brightness temperature measurements over DOME-C, Antarctica, are also discussed, where the effects of melt events are considered insignificant. By modeling the density variation as 3D, the polarization dependence of the measurement can be explained. This fact indicates the ability to predict V and H channel brightness temperature at off-nadir directions.

1.3 Electromagnetic Modeling for the perennial firn aquifer

During the summers, surface melt happens over the percolation facets of polar ice sheets in both GrIs and AIS. As the climate changes, the presence of meltwater over the GrIS and AIS will potentially become more frequent. For example, the extreme melting event in 2012 produced a surface melting over the entire GrIS [64]. Melting water is either refrozen locally within the firn or runs off into the ocean, contributing to rising sea levels. Meltwater generated at the surface of the firn percolates down into the deeper part of the firn. As a porous structure, firn can hold the melt water as the water fills the space between ice. Under certain conditions, a layer of ice-water mixture can remain unfrozen over the winter seasons and is called the Perennial firn aquifer. The perennial firn aquifer is one environment where liquid water exists in the polar ice sheet. A major discovery of an aquifer occurred in 2011 on the southeastern coast of Greenland during the Arctic Circle Traverse expedition by the drilled borehole. If drained, the Greenland aquifer could contribute up to 0.4mm of sea level rise [65]. Studies have shown an average age of aquifers of 6.5 years [66]. Instead of simply acting as a meltwater store, the water flows and drains the aquifer quickly [67]. This indicates that the aquifer is not buffering the mass loss or the rise of the sea level but perhaps delaying its contribution. Understanding the aquifer's water content can help close the mass balance of Greenland and the meltwater routing mechanism.

Remote sensing techniques have been used to study this form of water in the polar ice sheets. The mapping of the aquifer has been studied using the airborne GPR data in Operation Ice Bridge[68,69]. The thickness and the water content are estimated when the lower bound reflection can be observed [69]. The studies are limited to the flight paths, and the GPR data are gathered only once yearly in the late spring. Mapping for the horizontal extent of the firn aquifer from satellite data was first performed by using the Sentinel-1 C band SAR data [70]. High-resolution time series observations over the percolation zone have indicated a different time series signature

of firn aquifer from other percolation zone components: a logistic-like increase of backscattering coefficient from late summer to the late spring of next year.

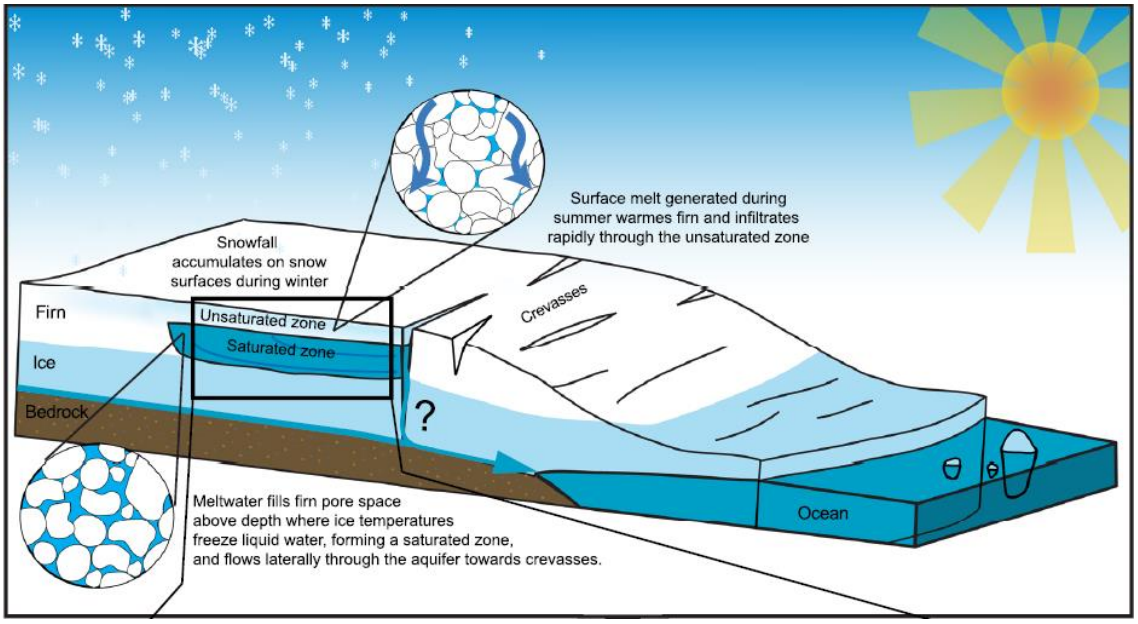

Figure 1-4 Process of forming firn aquifer in the percolation facet of the polar ice sheet. Firn aquifers are usually discovered near the coastlines in both Greenland and Antarctica. [66]

The physical process can be explained in Figure 1-4: During the summers, meltwater from the surface makes the firn wet from the surface to the bottom of the perennial firn aquifer. Starting from the end of summer, as the surface freezes up, the interface of the dry and wet firn starts to move downward, and the water level eventually reaches its lowest position. In this process, the dry frin contributes more back-scattered signals to the radar than the surface melting condition. As the dry/wet firn interface moves down, the total volume of dry firn increases, thus increasing the backscattering. The whole process eventually leads to a logistic-like time series of backscattering coefficients. Over the aquifer region, it takes months to let the backscattering coefficient increase from the minimum to maximum in a summer-winter circle. In contrast, for other components in the percolation zone(e.g., subsurface ice slab regions), the backscattering coefficient increases to

its maximum within a few days. However, due to the strong volume scattering from the ice structures, C-band SAR is not likely to observe the response from the aquifer.

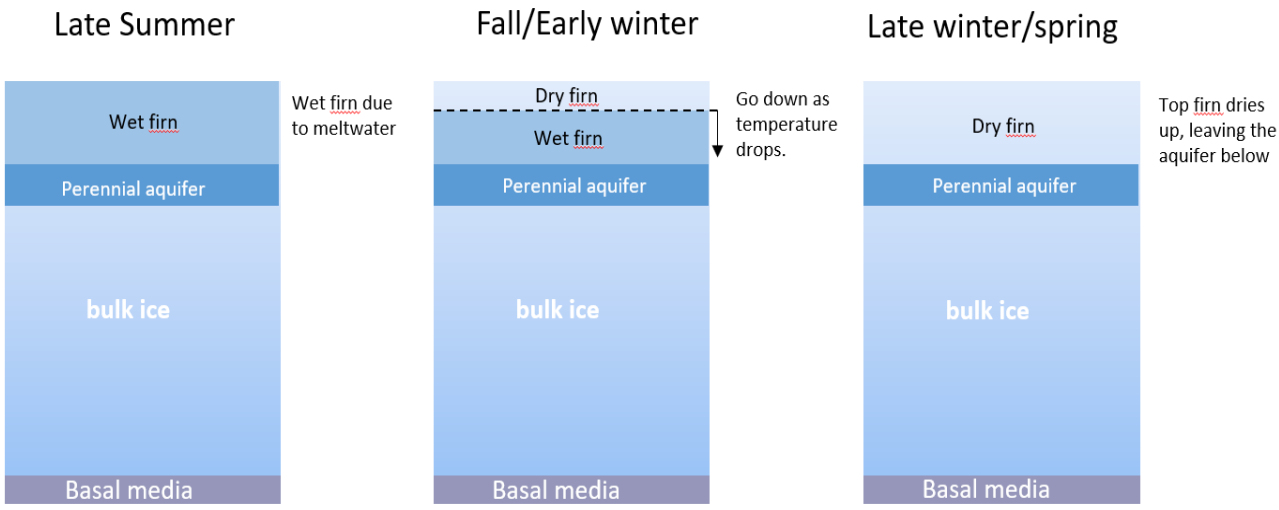

Figure 1-5 Seasonal profile change of aquifer region. In the later summer, surface meltwater makes the firn above the aquifer wet. As time goes by to the fall and early winter, dropping temperatures make the surface start to freeze

Lower microwave frequencies have better penetration through the dry firn and can directly interact with the aquifer. The enhanced resolution data of the Soil Moisture Active and Passive (SMAP)[71] radiometer at the L-band [72] has also shown a sensitivity to the aquifer region in the time series. Unlike the radar data, the brightness temperature data shows a logistic-like decrease in brightness temperature from late summer to late spring of the next year due to increased scattering from dry firn[73,74]. Based on the time series signatures, the enhanced resolution SMAP brightness temperature data is used to study the horizontal extent of the aquifer over Greenland. These works of SMAP data merely addressed the decrease of brightness temperatures due to freezing but have not addressed nor retrieved the water content of the aquifer during the winter/spring seasons. This can be due to the lack of physical models for the aquifer permittivity or the thermal emission process.

In modeling the thermal emission of the aquifer region, the properties of 2 components need to be characterized. The first part is a permittivity model of the firn aquifer, which is the key parameter

that relates the firn-aquifer interface reflection to the water content of the aquifer. The second part is a radiative transfer model that accounts for the reflection of thermal emission due to the firn-aquifer interface and the density variations in the dry firn. Reflection from the firn-aquifer interface is a function of the aquifer and dry firn permittivity. Once the properties of the dry firn are obtained, the reflection of the firn-aquifer interface can be separated from brightness temperature data. Using the permittivity model, we can estimate the water content of the firn aquifer.

1.3.1 Full wave simulation for the aquifer permittivity

In remote sensing, the permittivity of mixtures is important since natural media is usually complex. For example, in the remote sensing study of soil moisture, the amplitude of electromagnetic signal scattered by the land surface is proportional to the soil permittivity, which is highly affected by the water content. A relationship that describes the permittivity and water content is thus important for water content retrieval. One of the objectives in ocean studies is to evaluate ocean salinity, which is a remarkable index for understanding polar ice sheet mass loss. The loss factor of wet snow is also a topic of interest for hydrology studies.

The study of mixed media permittivity can be dated back to the early stage of electromagnetic theory. Over the years, researchers have proposed analytical theories to predict the permittivity of mixed materials under different assumptions. One of the most famous and commonly used formulas is the Maxwell-Garnett formula [75,76], which applies the quasi-static approximation, requiring the inclusions to be small compared to the wavelength in the background medium. The commonly used inclusion shapes are spheres and ellipsoids, where needles and discs are two special cases, as shown in Figure 1-6. Due to its anisotropic nature, ellipsoidal inclusion causes depolarization, which is accounted for in the mixing formula as depolarization factors, N_j where j stands for x,y, and z directions in the Cartesian coordinate system. The Maxwell-Garnett

formula has a concept of background material and inclusion material, treating them differently. Another well-known model is the Polder Van Santen or Bruggeman equation [75,77,78]. The formula also has the name of the De Loor equation [77,79]. The Polder Van Santee equation has no preference for inclusion or background when introducing the factors f_v and 1-f_v, where f_v is the volume fraction of one of the mixing components. The Polder Van Santen formula also requires a definition of the shape of the inclusion particles.

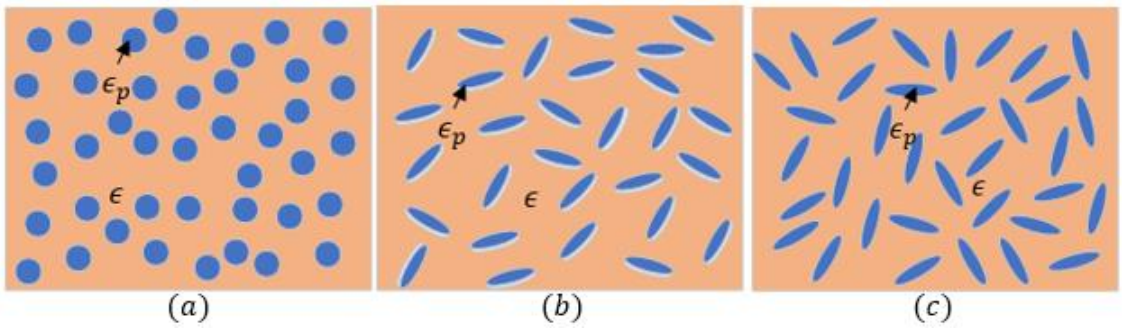

Figure 1-6 Different shapes of inclusions used in the classical mixing formulas. (a) Spheres, (b) discs, (c)Needles. Nature material does not necessarily have a definite shape of the inclusions.

Another method to relate the permittivity of the mixture to the volume fraction of a particular component, measurements for the permittivity of mixtures, have been performed. The empirical models are built for different natural media based on the measurement results. Dobson and Ulaby[77,80] provide a soil permittivity model as a function of water content based on low-frequency measurements. Mironov provided a soil permittivity model with broader applications based on measurements.[81] For the brine water, a double Debye model was built. Ulaby has also measured wet snow with up to 12% water content. [77,82]

When people first discovered perennial firn aquifer, studies for the extent and water content using remote sensing methods were carried out using GPR data. However, a quantitative study of the aquifer water content has not been performed using satellite microwave data due to the lack of permittivity information. Usually, the empirical wet snow model is used to characterize the firn

aquifer permittivity [82]. However, the model's validity in the L band remains questionable since it is claimed to be working in frequencies greater than 3GHz. Microscopic study over the firn structure [83,84] (Figure 1-7) has indicated that the space between ice has no definite shape. Thus, using the classical mixing formula with spheres or other shapes of inclusions is not appropriate.

Figure 1-7 The microstructure of space(black) between ice(white) from microscopic imaging[83,84].

Bi-continuous media is a computer-generated structure by the summation of random standing waves. The computer-simulated structure is consistent with the complex structures, as will be discussed in Chapter 4.

Given these facts, we propose to study the permittivity of the firn aquifer using full-wave simulation methods. Structures of aquifers are modeled as bi-continuous [85] media media. We use full wave methods to calculate the scattered waves of the highly heterogeneous media of the aquifer. The mixture is truncated into a sphere. The normalized scattering cross-section and absorption cross-section are calculated and compared to a Mie scattering. The effective permittivity of the mixture is then obtained by adjusting the permittivity of the Mie scatterer to match Q_{scat} and Q_{abs} , which are the normalized scattering and absorption cross-sections.

The numerical results show consistency with the Maxwell-Garnett formula prediction when the inclusions are set as spheres. Full wave solution using bic-continuous media provides

permittivity values different from classical mixing formulas. This theoretical work can help study water content in perennial firn aquifers.

1.3.2 Radiative transfer modeling for the aquifer thermal emission

The thermal emission problem of the perennial firn aquifer region can be represented by Figure 1-8, where the firn aquifer is below a layer of dry firn with 3-dimensional density variations, as is discussed in the dry firn problem. Due to the large loss factor of water and the typical thickness of the aquifer of 10-20m, thermal emission from the lower part of the bulk ice is blocked by the aquifer and thus will not be included in the modeling process. As a mixture of ice and water, the physical temperature of the aquifer stays at 273.15K. This is the condition where the definition of 0 degrees Celsius applies. The multiple borehole measurements for the temperature profiles also validate this fact. In the dry firn, the temperature varies slowly from 258K[65] at the top to 273K at the bottom. Ice has a very low loss factor. At the thermal equilibrium state, absorbed heat equals the heat radiated. As a result, the dry firn does not have a major thermal emission contribution compared to the emission from the aquifer.

The change of permittivity at the aquifer-firn interface and the density variations in the dry firn part would reflect the emitted power from the aquifer, reducing the brightness temperature observed by the radiometer. At the aquifer/firn interface, part of the thermal emission is reflected, and the density variations in the dry firn region then modulate the rest. To model this process, a radiative transfer model is developed to quantitatively evaluate the thermal emission. As the observation area is in the percolation zone, melting happens much more frequently than in the dry zone, the inner part of Greenland. The percolation and freeze and thaw processes shall create more horizontal variations than the dry zone. Also, the density variations are more significant in these

areas due to the refreezing of water. Thus, we use the 3-D density variation model to characterize the scattering in the dry firn.

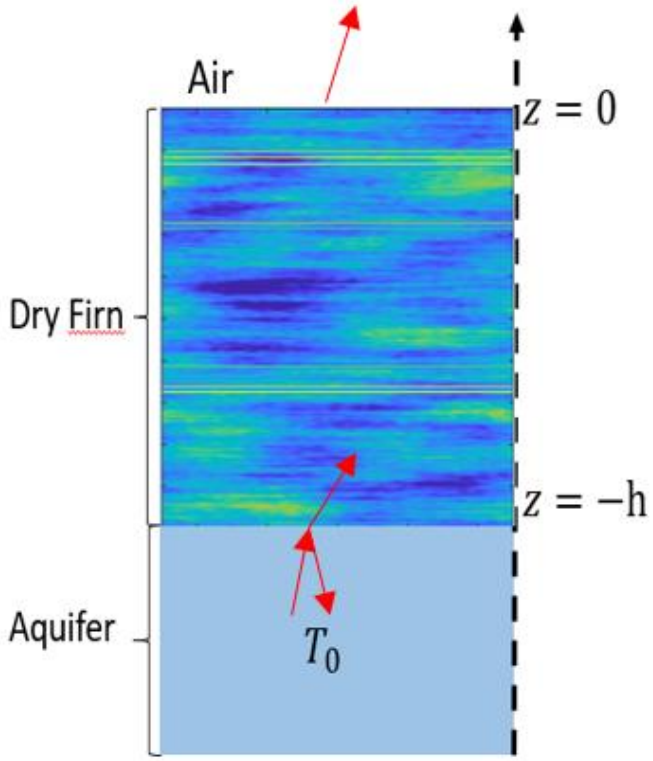

Figure 1-8 Description of thermal emission problem for firn aquifer

In formulating the radiative transfer equation, different from the emission problem in the aquifer-free area where the lower boundary of the density variation is non-reflective, the firn-aquifer interface is required to be considered as reflective due to the permittivity difference of dry firn and aquifer.

Positions of the aquifer upper boundary also need to be considered since they define the total thickness of the dry firn and affect the total reflection from the density variations. This information can be obtained either from borehole measurements or GPR echograms. Borehole measurements of water table depth have shown a different value from GPR estimations. This is due to the uncertainty of wave speed in the firn. Calibration of the depth needs to be performed for the study over the region without borehole measurements.

Simulation results over southeast Greenland near borehole site FA-13 have shown a good agreement with the SMAP enhanced resolution data collected in April 2016 for both V and H polarizations. This work provides a modeling basis for the quantitative retrieval of firn aquifer water content. Simulation results over FA-13 match with the SMAP V/H observations.

Chapter 2 Modeling Near Specular Bistatic Scattering for P-Band SoOp Land Observations

This chapter provides the details of the simulations of the near specular bistatic scattering coefficients. The Kirchhoff approaches are first discussed, followed by the steps to extract the surface properties of the intermediate scale, represented by f_2, and the slopes of topographical scales, denoted as f_3. The numerical simulation results for a single tilted planar patch are discussed in section 2.3, and finally, the incoherent bistatic scattering coefficients are discussed in section 2.4.

2.1 Surface scattering model

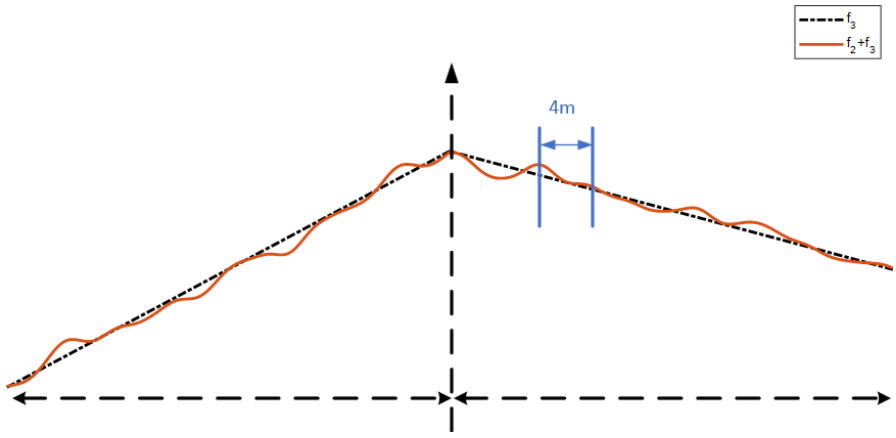

Figure 2-1 Land surface represented with multiple scales. Black dash line: coarse topography f_3, projection on x-y plane (e.g. 30 m). Yellow line: $f_2 + f_3$, where the "4 m" in the figure is an example of the correlation length of f_2. In this paper, the small scale f_1 is ignored due to its smallness compared to wave length at the P-band(81cm)

Details of the AKS and NKA are documented in [22] and [30], respectively. Here, we summarize the key characteristics of AKS. The representation of the land surface is first described in this model.

As shown in Figure 2-1, for the P band, the land surface is decomposed into two scales: $f(x,y) = f_2(x,y) + f_3(x,y)$. The topography is approximated by deterministic planar patches f_3. Each of the f_3 planar patches have definite slopes in the horizontal (x, y) directions. By approximation, it means that the size of the planar patch in f_3 must be small enough to correctly approximate the topography. For the results in this chapter, a size of 30m x 30m for a single f_3 patch is adequate. Thus, we have a total of 14,400 30m by 30 m f_3 patches within the study area of 3.6 km by 3.6 km. The scales f_2 are modeled as random profiles superimposed on f_3.

Since the study is designed to provide results in support of a SAR concept with a spatial resolution of about one hundred meters [20], the bistatic scattering coefficients for several 30m patches are of interest. In this paper, we use resolutions of 60 m, 120 m, and 240 m to assess the impact of spatial resolution limited by SAR processing as examples.

In AKS and NKA, we have both coherent field contributions and incoherent field contributions. The coherent and the incoherent are the mean and variances of the field, respectively. In the main text, we will discuss the incoherent field.

The bistatic scattering coefficient of the scattered field for right-hand circularly polarized incidence and left-hand circularly polarized scattering for the incoherent component of a single 30m x 30m f_{3n} is given by

$$\gamma_v^n = \frac{\cos\theta_i}{\pi}\left|\frac{R_v(\theta_i) - R_h(\theta_i)}{2}\right|^2 2\pi k^2 \int_0^\infty d_\rho \rho J_0\left(\rho\sqrt{(k_{dxn} + k_{dzn}p_{n3})^2 + \left(k_{dyn} + k_{dzn}q_{n3}\right)^2}\right) \{\exp\left[-k_{dzn}^2 h_{2n}^2(1 - C_{2n}(\rho))\right] - \exp\left(-k_{dzn}^2 h_{2n}^2\right)\} \quad (2\text{-}1)$$

where n denotes the index of the 30m f_3 in the total 14,400 f_3 patches within the area, $R_v(\theta_i)$ and $R_h(\theta_i)$ are the Fresnel reflection coefficients, respectively, for vertical and horizontal polarization with an incident angle at θ_i , and k is the wave number for the frequency of 370 MHz. The integral accounts for the effects of f_2 and f_3. Inside the Bessel function (J_0), The incident

direction is defined by θ_i and the scattering direction is defined by θ_{sn} and ϕ_{sn}, the wave vector for the incident and scattering waves are given as the following:

$$\overrightarrow{k_i} = k\sin\theta_i\hat{x} - k\cos\theta_i\hat{z}$$

$$\overrightarrow{k_s} = k\sin\theta_{sn}\cos\phi_{sn}\hat{x} + k\sin\theta_{sn}\sin\phi_{sn}\hat{y} + k\cos\theta_{sn}\hat{z}$$

The difference is thus given as $\vec{k}_{dn} = \vec{k}_{in} - \vec{k}_{sn}$. The parameters p_{n3} and q_{n3} are the slopes of this particular $f_3(x,y)$ patch, accounting for the tilting of f_3 patches. They are defined as the derivatives of $f_3(x,y)$ in x and y directions. h_{2n} and $C_{2n}(\rho)$ are the rms height and correlation function obtained from Lidar data on this particular f_3 patch.$C_{2n}(\rho)$ is constructed with Lidar data. Details on obtaining these parameters from Lidar data are discussed in section 2.2.

After the bistatic scattering coefficients are computed for each 30m patch, γ_v^{Np} for each resolution is obtained by the following equation:

$$\gamma_v^{N_p} = \frac{1}{N_p}\sum_{n=1}^{N_p}\gamma_v^n \qquad (2\text{-}2)$$

where $\gamma_v^{N_p}$ represents the bistatic scattering coefficient for N_p 30m x 30m patches within the resolution. For 60m, 120m, and 240m resolution in this paper, N_p corresponds to 4, 16, and 64, respectively. Each resolution will include the contribution from several 30mx 30m f_3 patches.

The bistatic scattering coefficient is defined as scattering cross section per unit area, and thus, the incoherent γ is independent of the observation area.

In AKS, we take the ensemble average overf_2, which is considered a random profile. The averaging is taken "Analytically" for which "A" stands. The average is taken with a rms height and a correlation function. [26-31].

NKA is used to validate the AKS solution. As from [30], the equation for NKA is as follows:

$$\vec{E}_s = \frac{ik\exp\left(ik(R_t + R_r)\right)}{4\pi R_t R_r}\sqrt{\frac{\eta P_t G_t}{2\pi}}\vec{p_s}\int dA'\exp\left(i\overrightarrow{k_d}\cdot\vec{r}'\right)\vec{F}(\alpha,\beta) \qquad (2\text{-}3)$$

where $\exp(i\overrightarrow{k_d}\cdot\overrightarrow{r'}) = \exp(i[k_{dx} + k_{dz}p_3]x' + [k_{dy} + k_{dz}q_3]y' + k_{dz}f_2(x', y'))$

In performing NKA, serval points need to be mentioned:

1) NKA performs the averaging of f_2 by the Monte Carlo method. Realizations of f_2 are generated based on the correlation function. The scattered wave from each realization needs to be computed using equation (2-3). Thus, results from NKA show speckle effects. In this chapter, several hundred realizations of f_2 are used.

(2) Averaging is taken over the realizations of the scattered field results. This is unlike AKS, where the averaging is taken analytically using the correlation function of the profile.

(3) On averaging over realizations, the speckle noise is decreased.

(4) In numerical averaging, we obtain the coherent field, which is the averaged field over the realizations. The incoherent field for each realization is obtained by subtraction of the mean field from the field. The variance of the field is then obtained using the incoherent field intensities for each realization.

(5) In NKA, the integral in equation (2-3) needs to be performed numerically over the profile. The discretization of the profile needs to be much smaller than a wavelength. In this paper, we use 5cm. Since the Lidar profile data f(x, y) data is of 3m resolution, we use a 2D cubic spline to interpolate the lidar profile of f(x, y) into 5cm. In generating the realizations, the random profiles are also at 5cm spatial discretization.

In both AKS and NKA, averaging is not taken for f_3 since f_3 representing the topography is deterministic. The bistatic scattering coefficients for multiple patches were previously given in our paper [22] for the GNSS-R application.

2.2 Extraction of correlation functions of f_2 and slopes of f_3 in x and y directions from Lidar Data

The properties of f_2 and f_3 presented here are derived from the ASO L4 Lidar Point Cloud 3-meter Digital Terrain model products. The lidar data were collected over Grand Mesa, Colorado (U.S.A) during snow-free conditions as part of the NASA/JPL ASO aircraft survey campaigns [23]. The data set provides a 3 m horizontal resolution elevation map with a 1.7 cm vertical resolution.

We select an area of size 3.6 km x 3.6 km in dimension, as shown in Figure 2-2, which is analyzed for the surface roughness properties examined herein.

The planar patches of f_3 are first extracted. Figure 2-2 shows the fitting of planar patches to the topography. The lidar data with 3m resolution is represented in blue, while the fitting lines to the profile, using different patch sizes, are indicated in orange. Figure 2-3 demonstrates that the 30m f_3 effectively represents the topography compared to the other three larger patch sizes. Larger patch sizes such as 60m, 120m, and 240m introduce significant errors in representing the topography. Hence, in this paper, a size of 30m is utilized for each f_3 planar patch size.

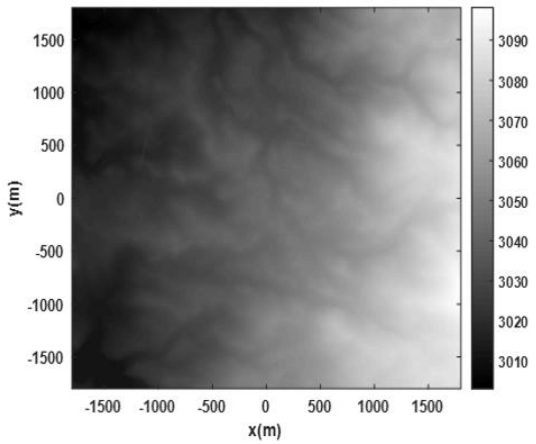

Figure 2-2 Lidar elevation data (in meters) for the selected 3.6 km x 3.6 km area in Grand Mesa (39.05N 108.13W)

The Lidar data is treated as a profile of $f_2(x,y) + f_3(x,y)$.To acquire the land surface properties of a single segment of 30m x 30m, several steps were taken and Figure 2-4 will be used as an example to illustrate the steps. First, the land surface is divided into 30m x 30m patches in the x-y plane. Figure 2-4(a) depicts a segment of Lidar data with a size of 30m x 30m in the x-y plane. The segment of Lidar data is subsequently fitted to a plane of the same size on the x-y plane, as illustrated in Figure 2-4 (b) to evaluate the slopes,p_{n3} and q_{n3}, which are the slopes of $f_3(x,y)$ in the x and the y directions respectively. The planar patch in Figure 2-4 (b) is the $f_3(x,y)$ for this particular 30m x30 m data, where the patch defines a single value of the slopes in the x and y directions. The f_3 profile could be anisotropic since slopes in the x and the y directions can be different.

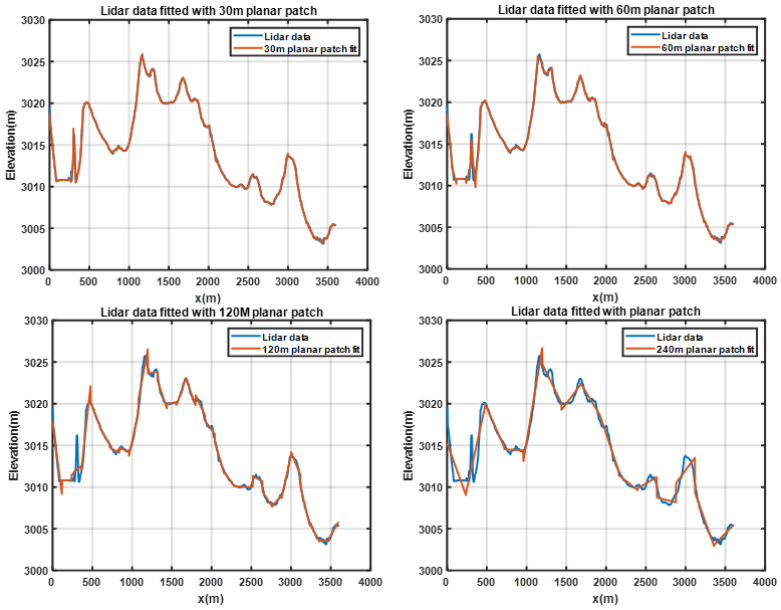

Figure 2-3 Representing the land surface with different patch sizes. A 30m patch size represents the land profile well. The other three larger patch sizes have significant errors.

Following subtracting out $f_3(x,y)$, what remains is the profile $f_2(x,y)$. The next step is to evaluate the rms height and correlation function for $f_2(x,y)$ of this 30m x 30m segment. To assess the rms height and correlation function, the profile is interpolated into a 5cm horizontal

resolution using 2-D interpolation over the f_2 (x, y). Thus, over a 30 m by 30 m patch, there are 600 by 600 =360,000 points in f_2(x,y). Using these 360,000 points, the rms height and correlation function of this $f_2(x, y)$ segment is calculated as follows.

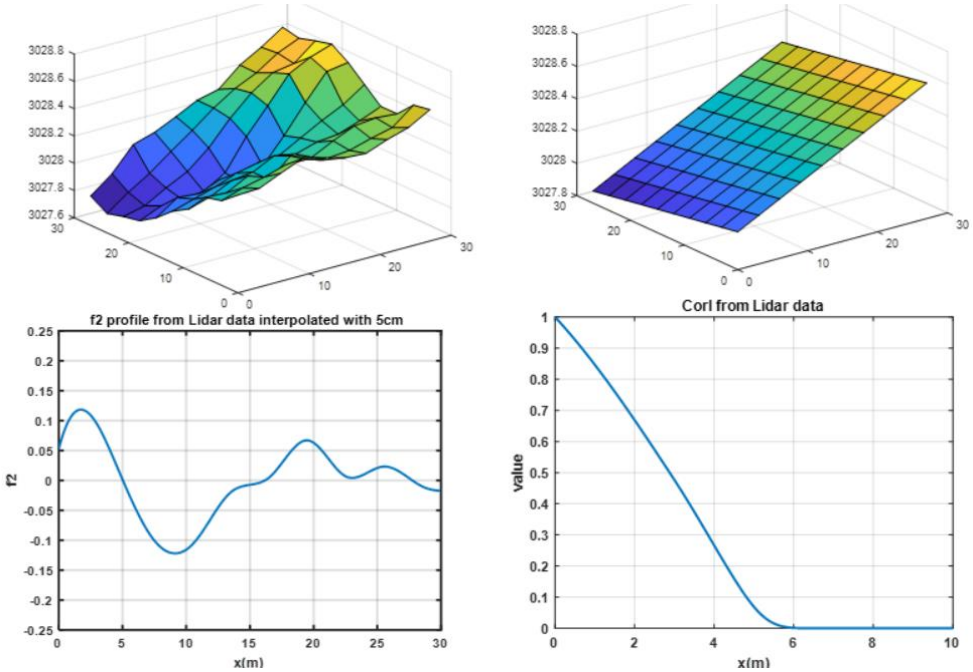

Figure 2-4 Extraction of surface properties from lidar data. (a) 30 m x 30 m patch size in the x-y plane, and (b) f_3(x,y) for the 30 m x 30 m patch. The planar surface is obtained by fitting the lidar data to a patch as in (a). (c) Example of the 1D (x) profile. (d) Example correlation function

There are 600 1-D profiles in the x direction and 600 1D profiles in the y direction, respectively. An example of the 1D profile is shown in Figure 2-4Figure 2-3 (c). We calculate the rms height of the 2D profile $f_2(x, y)$ for this patch as h_{2n}. To evaluate the correlation function of $f_2(x, y)$ on this patch, the following setps are taken. First, a 1-D profile along the x direction with y index, i, is taken. This profile is denoted as $f_{2x}^i(x)$. Then, The correlation function of this particular 1-D profile is then calculated as $C_{2x}^i(x)$. Thirdly, $C_{2x}^i(x)$ is normalized with respect to the peak value. For every profile with index i in the range of 1-600, the correlation functions are calculated. For the next step, the correlation function in the x direction for this segment of $f_2(x, y)$ is obtained by $C_{2x}(x) =< C_{2x}^i(x) >$ over i. After calculating $C_{2x}(x)$, the steps above are repeated

for each of the 600 1D profiles in y direction to obtain $C_{2y}(y)$. Finally, the correlation function of this particular f_3 is then obtained by $C_2(\rho) = \sqrt{\frac{1}{2}(C_{2x}^2(x) + C_{2y}^2(y))}$.

The correlation length, l_2, is thus obtained from the correlation function $C_2(\rho)$ when $C_2(l_2) = e^{-1}$. Rms height and correlation length of f_2 is provided in Figure 2-5 as maps and histograms. It is observed that f_2 is relatively isotropic, with only a minor difference between the x and y directions. As depicted in Figure 2-6, the ratio of correlation lengths in the x and y directions is centered in the range of 0.9 to 1.1. This is unlike f_3 which is anisotropic and exhibits different slopes in the x and y directions

To illustrate the distribution of combinations of h_2n and l_2n, a density plot is generated, as shown in Figure 2.7. As can be observed, the typical values of h_2 and l_2 are 7cm and 3.55m, respectively. Notice that the input to AKS is the correlation function $C_2(\rho)$ rather than the correlation length l. In this study, we use the extracted correlation function for each patch.

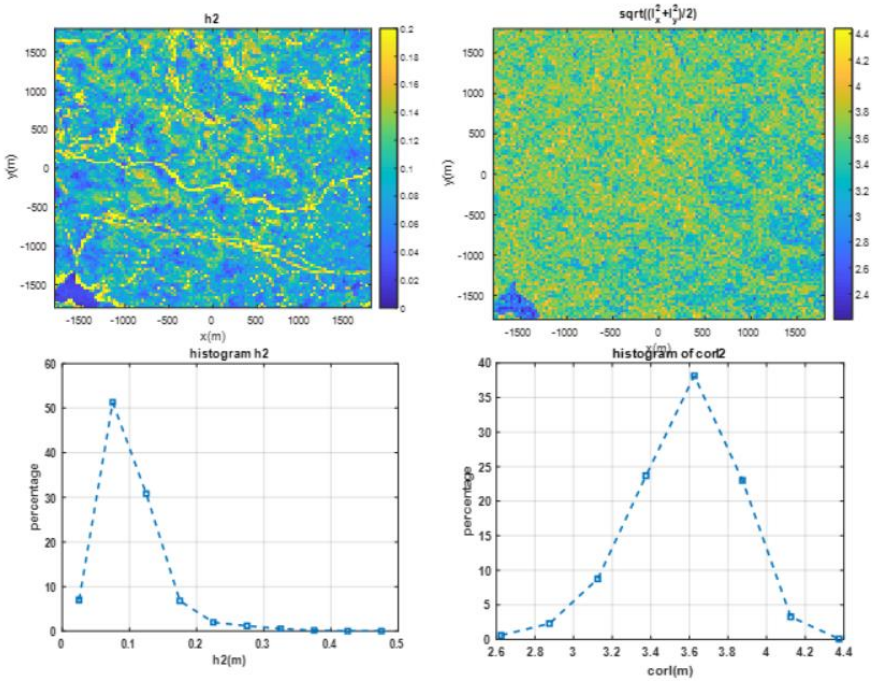

Figure 2-5 Properties of f_2 (x,y) using a 30 m patch size. The upper two panels show the rms height and correlation length for each 30 m x 30 m patch in the 3.6 km x 3.6 km area.

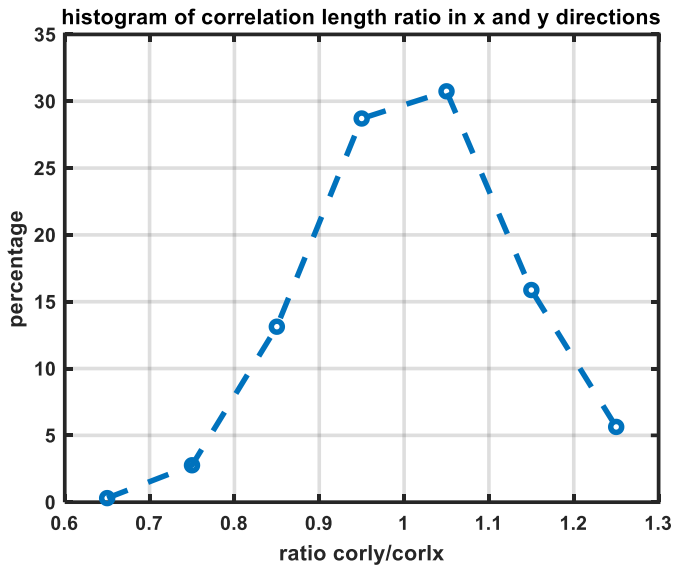

Figure 2-6 Histogram of correlation length ratio for x and y directions. It is shown that most of the ratios lie in the range of 0.9 to 1.1. Showing that the land surface is close to isotropic

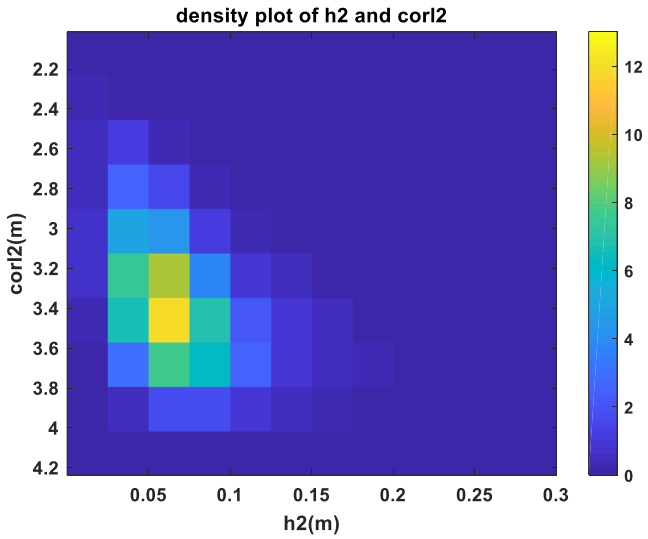

Figure 2-7 Density plot of h2 and corl2 for f_2(x,y). The typical number would be h=7cm, corl=3.55m (Color scale: percentage)

For the area 3.6 km by 3.6 km by 3.6 km, there are 120 by 120=14,400 planar patches. A total of 14,400 correlation functions have been extracted using the lidar data. These 14,400 calculated correlation functions, one for each patch, are utilized for the evaluation of bistatic scattering coefficients over the 3.6 km by 3.6 km area. This approach thus accounts for the surface inhomogeneity in this particular 3.6km x 3.6km study area.

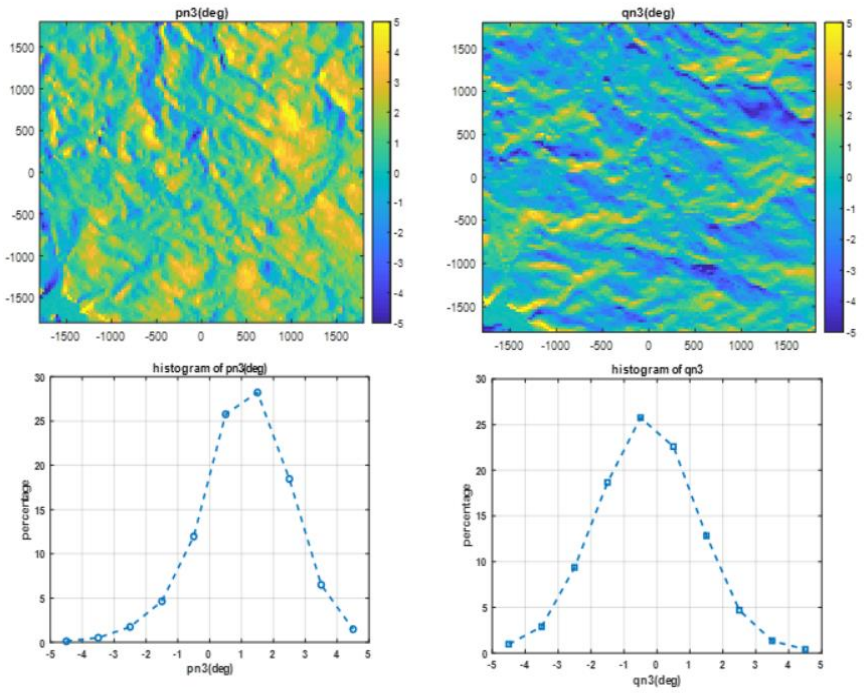

Figure 2-8 Slopes of f3 (x,y) patches with 30m patch sizes.

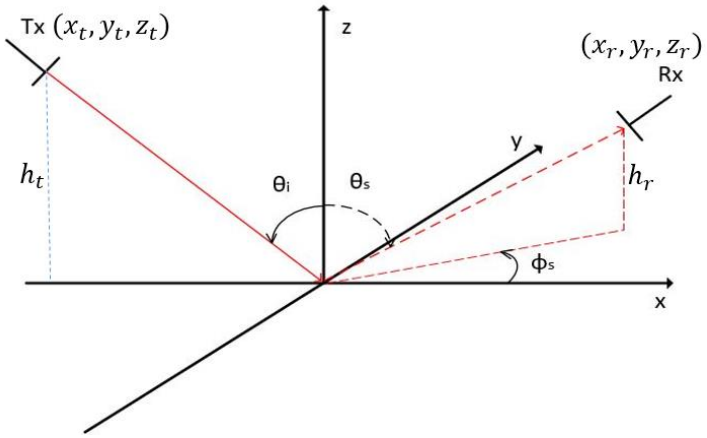

Figure 2-9 Set up for the scattering geometry. The specular point is the origin of the coordinate system. θ_i,θ_s are polar angles for incidence and scattering. ϕ_s is the scattering azimuthal angle.(x_t, y_t, z_t),(x_r, y_r, z_r) are the locations for transmitter and receiver

In Figure 2-8, the distributions of slopes in the x and y directions for 30 m patches are depicted. It can be observed that the slopes in the x (east-west) and y (north-south) directions are slightly different. The slope distribution in the y direction is centered near zero, while there is a positive mean slope in the x direction. This fact is consistent with the elevation map shown in

Figure 2-2, which shows a decreasing elevation from east to west.

Over the whole area, p_{n3} has a mean value of 1.2° and a standard deviation of 1.33°. The mean of q_{n3} is 0° with a standard deviation of 1.5°. Typically, for each patch, the x and y slopes differ significantly, indicating that the topography is generally anisotropic. On the other hand, the f_2 correlation functions are more isotropic in the x and y directions. The results from this section will be used for the bistatic scattering study with AKS.

2.3 Bistatic results for a single patch

In this section, the results of individual patches are illustrated. The bistatic scattering coefficients are studied for the cases with and without f_3 and also for varying distances of patches from the center of the scene. The scattering geometry setup is provided in Figure 2-9. The bistatic scattering is illustrated as a function of the azimuth scattering angle ϕ_s. We use the typical number of $h_2 = 7cm$ and the correlation function that has the typical value of 3.57m correlation length. AKS and NKA are both used. The permittivity is 5.5+2i. For NKA, a profile of f_2 is needed as input for each realization. We take the Fourier transform of the correlation function to obtain the power spectrum density and then generate profiles as input to NKA. The generation of the surface is discussed in appendix A. 400 profiles of f_2 are used to generate the second moment of scattered waves. To reduce the effects of the coherent field, when calculating the variance of the fields, the patch size is enlarged to 60m to reduce the angular spreading of the mean-field. For the f_2 only case, ϕ_s equals to 0-degree is not calculated for NKA due to the large peak from the mean field. The results in Figure 2-10 and Figure 2-11 are for the case when the patch is at the center with (x,y)=(0,0) of the scene. Figure 2-10 uses the typical number of p_{n3} and q_{n3} slopes while in Figure 2-11, an artificial slope $p_{n3}$of 3.4deg is used to show the effect of large slope.

For the effects of f3, we add the f_2 onto a tilted patch with $p_{n3} = 2deg$ and $q_{n3} = -1deg$,

which are typical slopes in this area. The results of AKS and NKA results are shown in Figure 2-10. The AKS and NKA results are in good agreement. Thus, the AKS results are validated by NKA. The effects of slopes are also shown. The f_3 slopes reduce the peak value of the bistatic scattering coefficients. The f3 slopes can also shift the peak value.

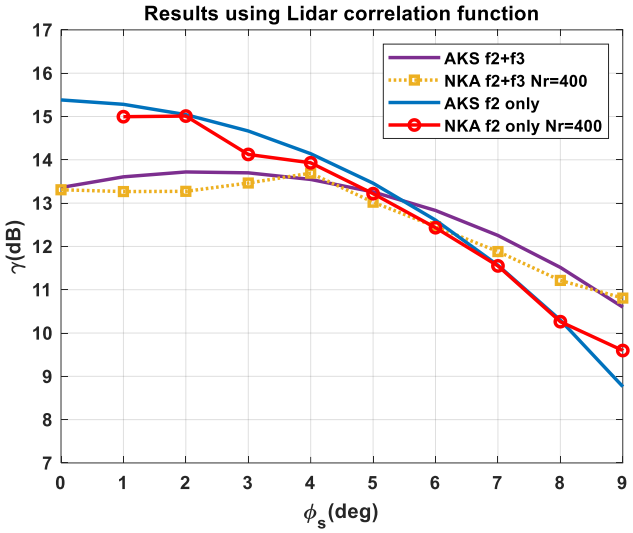

Figure 2-10 AKS and NKA results for a single patch with and without f3. The planar patch f3 has a tilting effect.

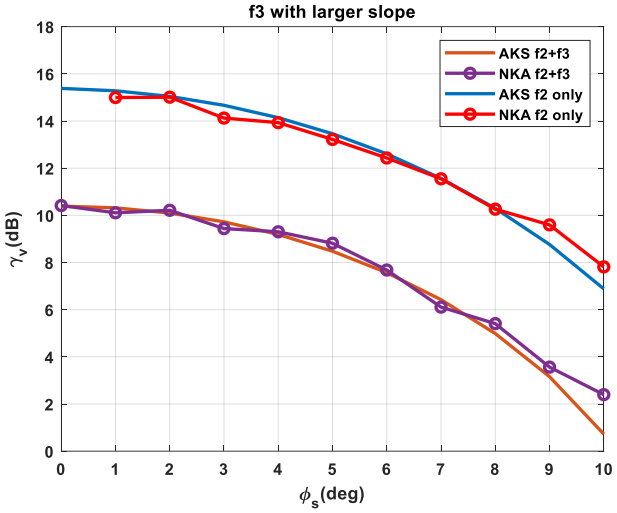

Figure 2-11 Incoherent bistatic scattering coefficients with or without the effects of large f3 slope. With an artificial slope of 3.5deg in the x direction, a reduction of 5 dB is observed. This is to show the effects of a large slope on the bistatic scattering coefficients

NKA and AKS results are also provided for a case where a large f_3 slope is used. The results are shown in Figure 2-11, where a planar patch f3 with an artificial p_{n3} value of 0.06 (or

3.4 deg) is used, which has a small fraction of patches in this area. The goal is to show the effects of large slope effects on the bistatic scattering coefficients. A large reduction of 5 dB is observed in the bistatic scattering coefficients in the near specular direction. This shows that the topographical slopes have strong effects on the bistatic scattering coefficients near the specular direction.

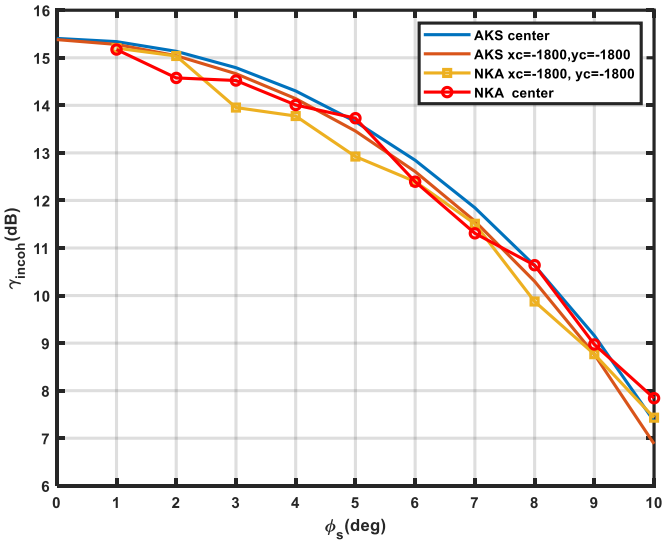

Figure 2-12 Bistatic scattering coefficients for 30m patch at and away from center(x-1800,y-1800). Due to the smallness of the area compared to the height of the transmitter and receiver, the incident and scattering directions do not have major changes. The difference is small.

We next examine the bistatic scattering coefficients when the patch is placed at the corner of the observation area with coordinates (x,y)=(1.8km,1.8km). The results are shown in Figure 2-12. There are no significant changes from the case where the patch is at the center of the scene. This is due to the high elevation of the transmitter and receiver compared to the size of the observation area.

2.4 Bistatic scattering coefficients over Grand Mesa

In this section, we discuss the bistatic scattering coefficients computed using AKS for the entire scene of 3.6 km by 3.6 km. We use the 14,400 calculated correlation functions, the $h_2 s$ and

also the p_{n3} and q_{n3}s, one for each patch. The setup of simulations is shown in Figure 2-9. For the soil permittivity, we use a value of 5.73+0.73i, corresponding to a volumetric soil moisture of about 10%. A local scattering coordinate system is created with the origin at the center of the 3.6 km x 3.6 km area. The transmitter is set at the position of $(\mathrm{x_t}, 0, \mathrm{z_t})$ on the geostationary orbit. The receiver is set at the position of $(\mathrm{x_r}, \mathrm{y_r}, \mathrm{z_r})$ on the lower earth orbit. The coordinates on the x-y plane for the transmitter and receiver are determined by the incidence angle (θ_i) and scattering angles (θ_s), respectively. The coordinates are provided as follows: $z_t = h_t, x_t = -\tan(\theta_i)\, h_t, z_r = h_r, x_r = \tan(\theta_i)\cos(\phi_s)\, hr, y_r = \tan(\theta_i)\sin(\phi_s)$, the annotations are provided in Figure 2-9.

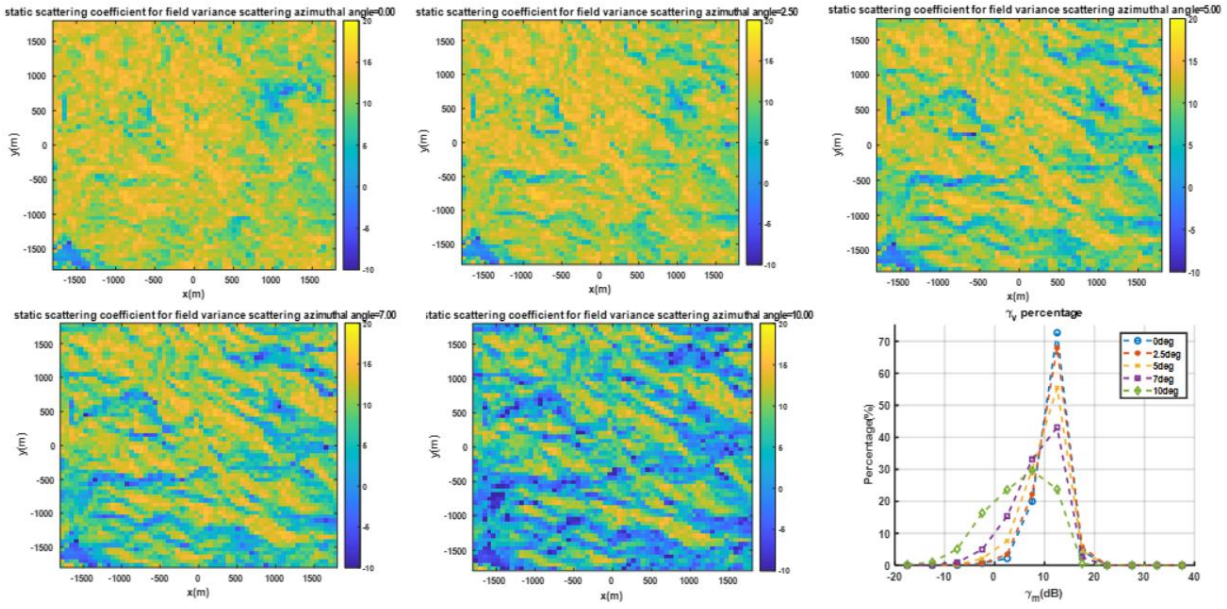

Figure 2-13 γ_v (in dB) for 60 m x 60 m resoltuion over the 3.6 km x 3.6 km area using the results from Fig 5 and Fig 8. From panel (a) through (e), $\theta_i = \theta_s = 40^\circ$, while ϕ_s are 0° to 2.5 degrees, 5 degrees, 7 degrees, and 10 degrees. γ_v decreases as the ϕ_s increases. The distribution of γ_v in dB is in panel f. It can be observed that the peak of γ_v decreases as ϕ_s increases.

We first study the effects of the azimuth angles in the observation direction. In the simulation, we set $\theta_i = \theta_s = 40^\circ$ at the position of the center of the area of interest. The bistatic scattering coefficient of each 30m f_3 is calculated with (2-1) using the h_{2n}, $C_{2n}(\rho)$, p_{n3} and q_{n3}

obtained from section 2.2. For azimuth angles, $\phi_s$is set as 0, 2.5, 5, 7, and 10 degrees to calculate γ_v and γ_m. We look at the resolutions of 60m, 120m, and 240m. The results are obtained based on (2-2). That means each resolution needs to average over 4, 16, 64, 30m x30m γ_vs within that particular resolution.

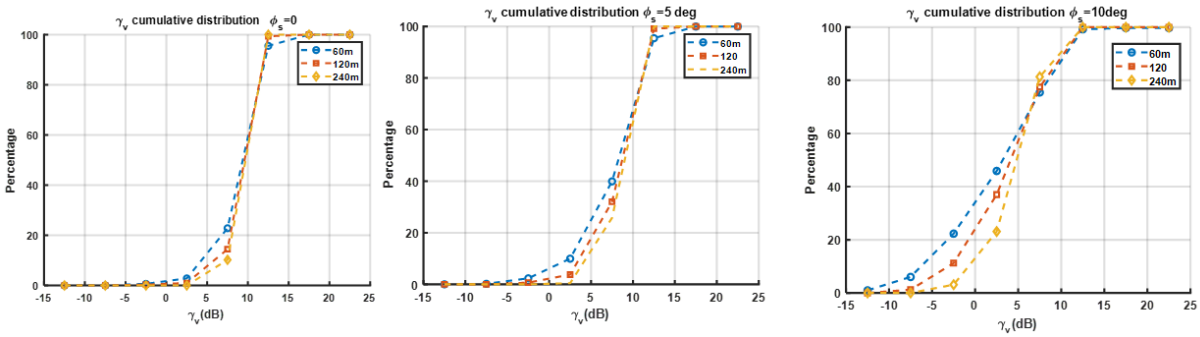

Figure 2-14 Cumulative distribution of γ_v for different resolutions. The distributions are consistent.

Results for γ_v from (2-2) for the 3.6 km x 3.6 km area with 60 m x 60 m resolution are illustrated in Figure 2-13. As shown in Figure 2-13 (a) (specular direction), γ_v can be as large as 20 dB and is mostly above 10 dB. It can be observed that in the region around (1000 m, 500 m), a low γ_v region is shown. This is mainly due to the large slopes for the corresponding region (Figure 2-8). The slopes of pn_3 in that region is larger than the other regions, reducing the scattered power in the receiver direction. This reduction is not due to the properties of f_2 since the rms height and correlation length do not show many differences compared to other regions. The spatial patterns of γ_v at the azimuth angles of 2, 5, 7 and 10 degrees are similar; however, γ_v decreases with the increase of ϕ_s as shown in Figure 2-13(f). The peak of the histogram gradually moves to the lower value bins. But as shown in the case of $\phi_s = 10^{\circ}$, about 10% of the patches within the region still have a value γ_v above 10dB.

To further compare the effects of different resolutions, the cumulative distribution of the bistatic scattering coefficients is presented in Figure 2-14. Azimuthal scattering angles of 0, 5, and

10deg are provided with different resolutions. It is shown that the three resolutions are consistent with each other.

For a given radar system, the swath of measurement and the ability to detect the signal is determined by the gain pattern of the receiving antenna. High-gain antennas usually have a small beam width, which makes the footprint on land (swath) small, while antennae with smaller gain will have a larger swath. For a given SNR, the large value of γ_v reduces the requirement of antenna gain, which allows a broader swath on land.

2.5 Conclusions

In this chapter, we study the bistatic scattering coefficients for the mean and variance of the bistatic scattered field near the specular direction for P-band frequencies. Simulation parameters are obtained from the Lidar measurements over Grand Mesa. 30m planar patches f_3 size is an appropriate choice for approximating land topography in Grand Mesa. Using the lidar data, we calculate the correlation function of f2 for each 30-meter by 30-meter patch for the 3.6km by 3.6 km scene. AKS results are calculated for each 30-meter by 30m patch using the 14,400 calculated correlation functions.

Simulation results show that γ_v is of the highest significance: the value can be as large as 10 dB over a wide range of azimuth angles. The value decreases as ϕ_s increases but can still be significant with a value greater than 0 dB. Results show significant values of γ_v within 5 to 10 degrees in azimuth from the specular direction, which will lead to a generally high SNR for SoOp reflectometry over a range of cross-track distances (swath), which is proportional to the feasible range of azimuth angle. The choice of f3 can be adjusted based on the topography as f_3 profile is composed of planar patches that approximate the topography. The size of f3 can be larger when

the topography has smaller slopes than those of Grand Mesa. The size of the planar patches in f_3 can be smaller when the topography has larger slopes than those of Grand Mesa. The same AKS model can still be applied to such cases.

Appendix A: Generation of Random Profiles for NKA

We discuss the generation of random profiles, f_2, based on the correlation functions. The correlation function obtained from Lidar data is symmetrical in the x and y directions. We thus perform a 2D Fourier transform to obtain the power spectrum density of the surface. Since the resolution of Lidar data is 3m, Wk components that are greater than 2.1 are ignored. With the Wk, we follow the method in [86] Chp.4 to generate the random profiles of $f_2(x, y)$. Examples of Wk and generated random profiles compared with Lidar data are shown in Figure 2-15 and Figure 2-16, respectively.

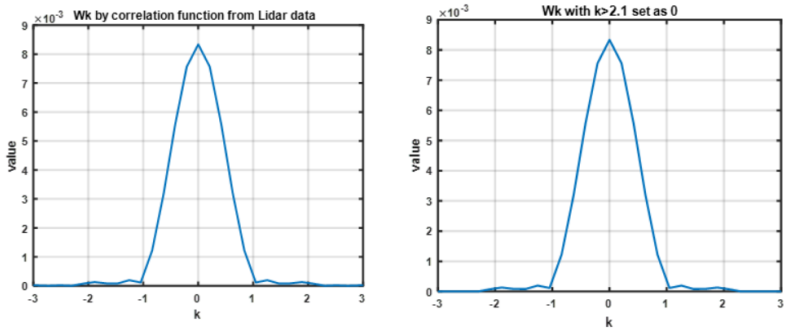

Figure 2-15 Power spectrum density before and after truncating at 2.1, corresponding to 3m of the Lidar resolution.

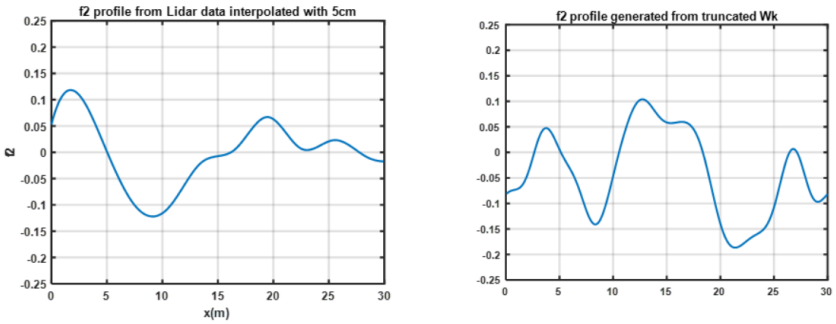

Figure 2-16 Profile from Lidar data and Wk generation

Appendix B: Results of Mean-Field

The coherent field gamma is given in (2-4).For the mean field of each f_3 patch, the bi-static scattering coefficient is provided as:

$$\gamma_m^n = \frac{\cos\theta_i}{\pi}\left|\frac{R_v(\theta_i) - R_h(\theta_i)}{2}\right|^2 \mid kL\exp\left(-\frac{k_{dzn}^2 h_2^2}{2}\right) \qquad (2\text{-}4)$$
$$\sin\ c\left[\left(\frac{k_{dnx}}{k_{dnz}} + p_{n3}\right)\frac{k_{dnz}L}{2}\right]\sin\ c\left[\left(\frac{k_{dny}}{k_{dnz}} + q_{n3}\right)\frac{k_{dnz}L}{2}\right]\Bigg|^2$$

Where the term $\exp\left(-\frac{1}{2}k_{dzn}^2 h_2^2\right)$ account for the decay due to surface roughness. The sinc functions account for the beam width and the direction of the mean field.

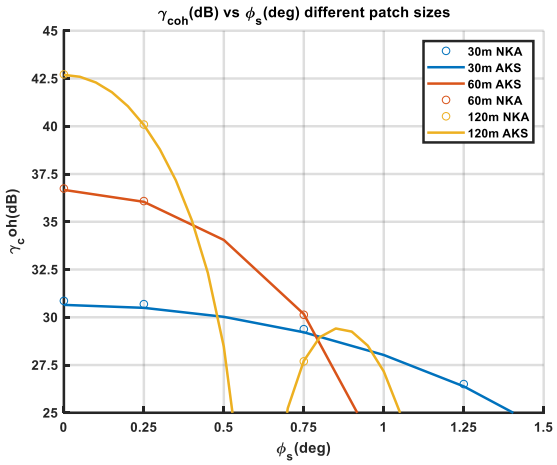

Figure 2-17 Bistatic scattering coefficient of mean field vs different $\phi_s(deg)$ patch sizes

In the comparison of (2-1) and (2-4), it can be observed that γ_v is independent of area, however for γ_m, it is a function of the area. γ_m thus 1) increases with area, 2) becomes exponentially small with the increase of h_2 3) is sharply peaked in the specular direction with decreasing angular width as observation area increases, and 4) decreases sharply when there is a tilting due to f3 because the receiver is away from the specular direction of patch f3.

Figure 2-17 shows the scattering pattern of the mean field from AKS and NKA. Only f_2 is calculated with the profiles placed in the center of the observation area. Different patch sizes of 30m, 60m, and 120m are used. The rms height and correlation function used is the same as in section 4. As stated previously, the bistatic scattering coefficients of the mean-field are proportional to the area in the specular direction. The angular width of the mean field is also sharpened as the planar patch size increases. The inclusions of bistatic scattering coefficients of the coherent field need to be considered together with the instrument characteristics of the receivers of the P-band reflectometry.

Chapter 3 Polar Firn Properties in Greenland and Antarctica and Related Effects on Microwave Brightness Temperatures

In this chapter, we study the brightness temperature of polar ice sheets. We first discuss the data used for analysis and then discuss the 3-Dimensional density variation model for the forward simulation of brightness temperature. Finally, the forward simulation results are compared with measurements.

3.1 Method

3.1.1 Ultra-wide Band software defined Radiometer(UWBRAD) and Snow Rdar data

UWBRAD measures ice sheet 0.5-2GHz brightness temperatures in a nadir viewing geometry [87]. The cumulative effects of the temperature profile, density fluctuations, and the effects of refrozen layers are all included in the sensed brightness temperature. Two measurement flights were taken over Greenland in 2016 and 2017. The 2016 flight path ended near Camp Century, while the 2017 flight has a much longer patch that covers not only Camp Century but also NEEM and NGRIP.

The University of Kansas Snow Radar [88] included in Operation IceBridge campaigns operates over the 2-6.5 GHz frequency range. Because the corresponding 4.5 GHz bandwidth enables a 2 cm vertical resolution of firn echoes, snow radar data can help to characterize the near-surface properties of the firn.Begining in the summer of 2013, great melt events occur over the entire Greeland, reating refrozen layers in the firn. In particular, high dielectric contrast refrozen layers that extend over larger horizontal distances produce significant radar backscatter, enabling their

characterization with radar measurements. The effects of these finite number of high frozen layers in the radiometer have never been included. The depths and number of refrozen layers within the firn can also be inferred based on the time delay of the associated radar echo. Radar measurements, however, are not optimal for sensing moderate density fluctuations within the firn because such fluctuations do not produce high backscattered power levels due to their low dielectric contrast.

Overlapping location index (North to south)	Latitude	Longitude
1	77.266N	49.121W
2	76.563N	44.778W
3	76.168N	44.329W
4	75.535N	42.7948W

Table 3-1: Latitude and Longitude for crossover locations of 2017 UWBRAD and Snow Radar Measurements

To assess the potential utility of combined active and passive measurements of firn properties, locations one through four, as listed in Table 3-1, were identified based on the 2017 flight paths depicted in Figure 3-1, where Snow Radar and UWBRAD were nearly co-located over Greenland. An X-ray tomography data near the first location compared with the radar echo to validate the existence of refrozen layers.

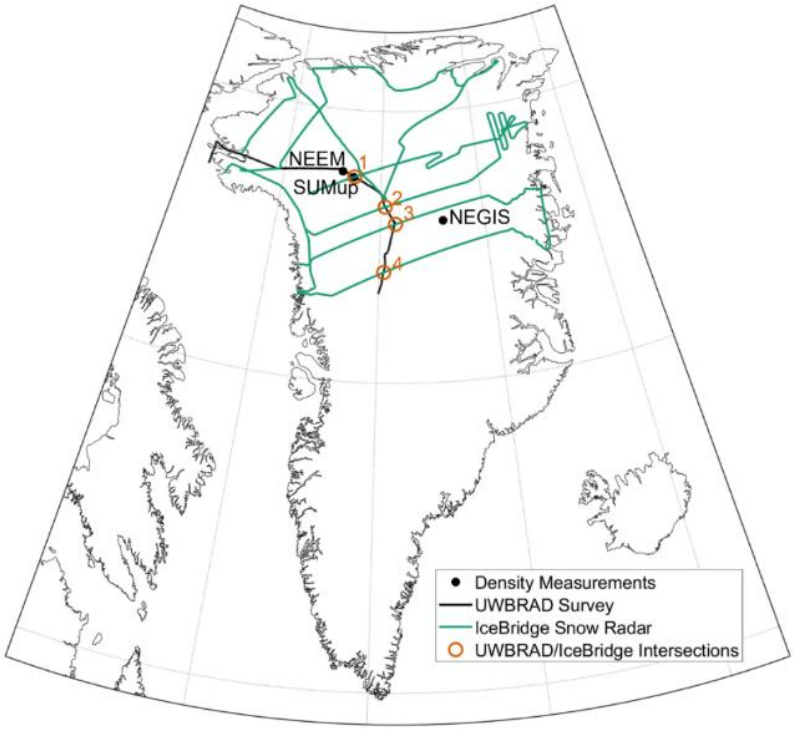

Figure 3-1 Flight paths of UWBRAD and Snow Radar in 2017.

3.1.2 The Community Firn model and In-situ measurements

The locations where active and passive measurements are both available are presented in Figure 3-1. Although lots of in-situ measurements of snow density are available, they are dispersed over a large spatial and temporal scale [46]. Previous studies have shown that thermal emission at 0.5-2GHz is highly influenced by density fluctuations in the centimeter scale range. However, in-situ measurements are usually taken on a scale of tens of centimeters, which does not fit the need

to characterize the density statistics on the microwave scale. Thus, to evaluate the inferred density fluctuations from microwave sensor data, we use the modeled firn profile as a reference.

We use the Community Firn Model v1.1.6 (CFM) [45] to simulate the firn column density profile at several locations across the ice sheet. The CFM was built as a resource to the glaciology community and consists of a modular, open-source framework for Lagrangian modeling of several firn and firn-air-related processes [45]. CFM simulations are set up as detailed in [44], where the model is forced by a modified version of the MERRA-2 global atmospheric reanalysis [89] at a 5-day temporal resolution. The only difference between the CFM simulations from [44] and those presented here is that a time-varying initial density ρ_0 of the firn column is introduced using the parameterization in [104]: $\rho_0 = 362.1 + 2.78\,T_a$, where T_a is the atmospheric temperature in °C at each time step. When comparing CFM-generated density profiles with observations, we use the simulated profile that is most contemporaneous with the observations. For a detailed description of the CFM set up, see [44]. The vertical density profile of the firn can be characterized by $\rho(z) = \rho_m(z) + \rho_f(z)$, where $\rho_m(z)$ is a mean profile that gradually increases with depth and $\rho_f(z)$ is a fluctuating profile which fluctuates around $\rho_{\mathrm{m}}(z)$ and is characterized by standard deviation $\Delta\rho(\mathrm{z})$ and correlation length $\mathrm{l_z}(z)$.

We selected 3 locations to compare in-situ measurements and CFM simulations. The first profile was collected at T41 (71.08N,37.92W) along the EGIG line by Morris [90] in 2004 using a neutron probe. Data was collected up to 13 meters below the surface at a vertical resolution of 1 cm, and significant fluctuations in density in the upper firn were clearly shown. The second profile and third profiles are from a 2009 borehole measurement at the NEEM site [91](NEEM Firn Core 2009S2 Density and Permeability) with a vertical resolution of ~90 cm and from a 2012 measurement at the NEGIS [92] site having ~1 m increments. The goal is to evaluate whether the

CFM simulation can provide a density fluctuation and a mean profile, which are physically compared to the real world.

3.1.3 Analytical Partially coherent model

To interpret the brightness temperature, an analytical partially coherent model is implemented. An illustration of the ice sheet thermal emission problem is shown in Figure 3-2. A firn layer of thickness d_1 (region 1) exists near the ice sheet surface. The density of the firn layer is modeled as $\rho(\vec{r}) = \rho_m(z) + \rho_f(\vec{r})$ with $\rho_m(z)$ the mean density profile. As a result of the significant melt events that commenced in 2012, refrozen high-density layers have emerged in the area, which is traditionally regarded as a dry zone. The effects of these layers are also considered. The fluctuating profile is described as $\rho_f(\vec{r}) = \rho_{fs}(\vec{r}) + \rho_{fl}(\vec{r})$. Notice that the fluctuating profile varies in three dimensions and has two scales: short (ρ_{fs}) and long (ρ_{fl}). The real and imaginary parts of the microwave permittivity of the firn are related to the firn density using the models in [93][94]. The correlation function for each scale of the fluctuating density is described by

$$\left(\Delta\varepsilon_{rf}\right)^2 C\left(\left|\vec{r} - \vec{r'}\right|\right) = \left(\Delta\varepsilon_{rf}(z)\right)^2 \exp\left(-\frac{|z-z'|}{l_z(z)}\right) \exp\left(-\frac{(x-x')^2+(y-y')^2}{l_\rho^2}\right) \qquad (3\text{-}1)$$

in which $\Delta\varepsilon_{rf}(z)$ is the standard deviation, $l_z(z)$ is the permittivity vertical correlation length, and l_ρ is the horizontal correlation length. The correlation function is described as having a Gaussian form laterally and an exponential form vertically based on the model used in [86]. The exponential form for the vertical correlation function is adopted based on analyses showing similar properties for the firn density itself [86]. Both $\Delta\varepsilon_{rf}(z)$ and l_z are modelled as functions of depth due to the compaction of the firn, while l_ρ is modelled as independent of depth.

Below region 1, the main ice body can be multiple km thick with a temperature profile that varies in depth. Thermal emission from the main ice body is calculated using the existing partially coherent model [59] and the temperature profile obtained in [60]. The temperature in region one is modeled as a constant value, T_0 . Although the top 10-20 m of firn experiences seasonal temperature changes, these variations have little effect on brightness temperatures at frequencies less than 2 GHz due to the limited emission directly from the firn layer.

Applying the radiative transfer theory of microwave emission and scattering, the upward and downward propagating specific intensities $\vec{T}_u$ and $\vec{T}_d$ in region one satisfy:

$$\begin{aligned}\cos\theta\frac{d}{dz}\vec{T}_u(\theta,z) &= -\kappa_a(z)\vec{T}_u(\theta,z) - \bar{\kappa}_s(\theta,z)\vec{T}_u(\theta,z) + \kappa_a(z)\bar{T}_0 + \int_0^{2\pi}\sin\theta' d\theta' \overleftrightarrow{F}(\theta,\theta,z)\vec{T}_u(\theta',z) \\ &\quad + \int_0^{2\pi}\sin\theta' d\theta' \overleftrightarrow{B}(\theta,\theta',z)\vec{I}_d(\theta',z) \\ -\cos\theta\frac{d}{dz}\vec{T}_d(\theta,z) &= -\kappa_a(z)\vec{T}_d(\theta,z) - \kappa_s(\theta,z)\vec{T}_d(\theta,z) + \kappa_a(z)\bar{T}_0 + \int_0^{2\pi}\sin\theta d\theta' \overleftrightarrow{B}(\theta,\theta',z)\vec{T}_u(\theta',z) \\ &\quad + \int_0^{2\pi}\sin\theta' d\theta' \overleftrightarrow{F}(\theta,\theta',z)\vec{T}_d(\theta',z)\end{aligned}$$

(3-2)

with the boundary conditions:

$$\begin{aligned}\vec{T}_d(\theta,z=0) &= \overleftrightarrow{r_{10}}(\theta)\vec{T}_u(\theta,z=0) \\ \vec{T}_u(\theta,z=-d_1) &= T_2\end{aligned} \qquad (3\text{-}3)$$

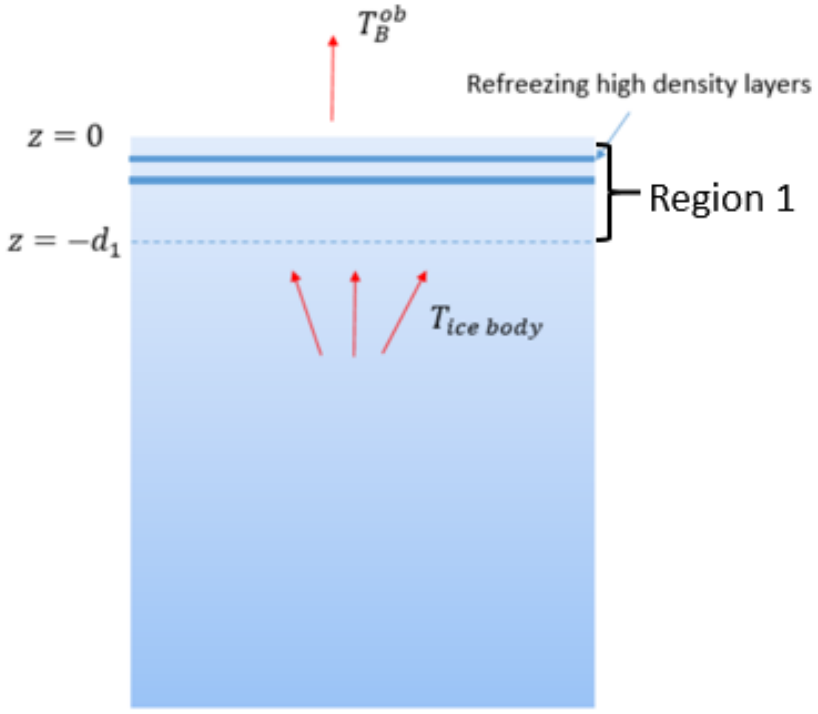

Figure 3-2 Thermal emission from an ice sheet

In the above equations, $\vec{T}_u$ and T_d are 2 x1 vectors in which the upper row is for vertical polarization and the lower row is for horizontal polarization. $\kappa_a(z)$ is the absorption coefficient determined by the mean density profile, while $\overline{\overline{\kappa_s}}(\theta, z)$ is the scattering coefficient due to the randomly fluctuating portion of the density profile. The phase matrices $\overline{\overline{F}}$ and $\overline{\overline{B}}$ couple specific intensities from other directions θ' into the direction of interest θ in the forward or backward propagating hemispheres. The boundary conditions specify that the firn-to-air interface at $z = 0$ is reflective, which is characterized by the reflection coefficient tensor, $\overleftrightarrow{r}_{10}(\theta)$ and that the compacted firn to ice interface at $z = -d_1$ with $d_1 = 100m$ is not reflective. An iterative approach is then used to solve the equations. Since the permittivity variation is small, the first-order solution, together with the zeroth-order solution, provides sufficient accuracy. A detailed solution of the equations can be found in Appendix A. The method is partially coherent because

the phase matrices are obtained using a coherent formulation of the continuous medium scattering problem. High-density refrozen layers are included by incorporating their additional reflections as

$$T_{ob} = (1 - r_{10})(T_u^{(0)}(\theta = 0, z = 0) + T_u^1(\theta = 0, z = 0)) \prod_n (1 - r_n^{ref}) \quad (3\text{-}4$$

where $\prod_n (1 - r_n^{refrez})$ accounts for the transmission from each layer. This multiplicative approach is reasonable because the microwave wavelength in the range of 0.5~2GHz is larger than the typical layer thickness.

The resulting model captures coupling between scattering in different directions and polarizations through the phase matrices, $\bar{\bar{F}}$ and $\bar{\bar{B}}$. The previous "random layer" 1D formulation of [59] captures neither of these effects.

3.2 Results

3.2.1 Firn density measurements at borehole sites and the associated CFM profiles

The high-resolution profile (1cm resolution) at T41 enables an estimation of the standard deviation $std(\rho)$ and correlation length l_z of the fluctuating profile every meter in depth (Tabel 2). The coarser profiles (~1m resolution) at Sites 2 and 3 do not allow such analysis, but information on the depth at which a "critical" density (i.e., 550 kg m^{-3}) is reached can be obtained.

In Figure 3-3, the profiles from T41 high-resolution measurements and CFM simulation are plotted. The standard deviation of density and its correlation length based on every 1-meter segment is provided in Table 2. Both the in-situ and CFM profiles at T41 show small and fast variations superimposed on the larger but relatively slowly varying mean profile. One-meter density standard deviations ($\boldsymbol{std(\rho)}$) in Table 2 for the neutron probe and CFM are comparable, with most of the values around 0.03 g/cm^3. Vertical correlation lengths obtained both from the

Morris' profile and the CFM simulation are <20 cm with mean values of 14.2 and 9.4cm, respectively. The results from CFM are usually used to evaluate the mean firn density.

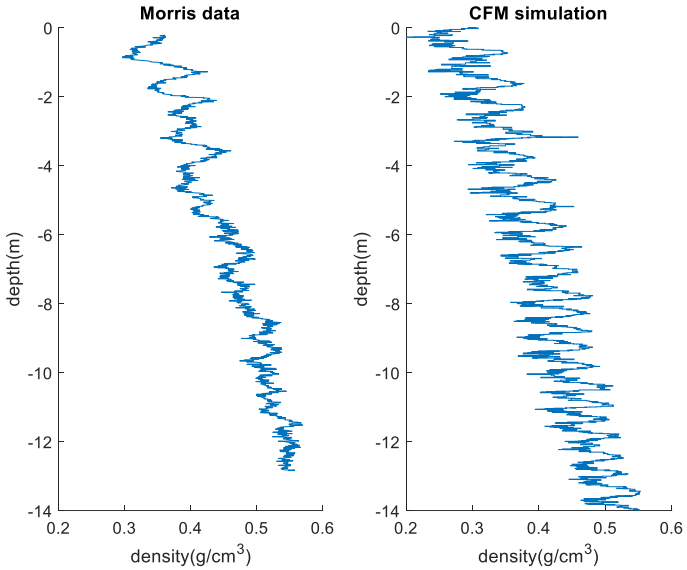

Figure 3-3: (left) Morris and Wingham, 2011 density profile measured near Summit station, Greenland, Summer 2004 (right) corresponding CFM model simulation

Depth(z)	Neutron Probe data		CFM	
	$std(\rho)(\frac{g}{cm^3})$	l_z(cm)	$std(\rho)(\frac{g}{cm^3})$	l_z(cm)
0	0.028	16	0.03	9.6
2	0.019	17	0.027	12
4	0.01	12	0.029	11
6	0.012	17	0.028	9
8	0.011	12	0.028	7.5
10	0.0086	11	0.023	7

Table 3-2: Estimated density standard deviations (std(ρ)) and correlation lengths ($\boldsymbol{l_z}$) estimated using 1 m of data beginning at the specified depth for Summit Station, Greenland, from the Neutron Probe dataset of Morris and Wingham, 2011 and the CFM

The comparison here is to show that: 1. the CFM is not generating very large fluctuations ((ρ)>$mean(\rho)$) since the observed density profile shows an rms density of fluctuation smaller than the mean profile.2. The simulated profile is not changing too slow compared to the measurements. If the profile is changing too slowly ($l_z\ CFM$>$2l_z measured$), this means that the simulated CFM profile is not able to characterize the density changes. This shows that CFM results are reasonable compared to measured data. The comparison here is performed for the statistics of "long scale" (l_z of several cm), which is mainly due to the yearly snowfall. The "short scale"(l_z <2cm), despite the observed fluctuations in the profile, cannot be captured because the data resolution is comparable to the correlation length.

Site	Critical density depth: In-situ (m)	Critical density depth: CFM (m)
NEEM	15.8	14
NEGIS	18.11	18.13

Table 3-3 Estimated depth at which mean density profile reaches critical density value of 550 kg m-3 for NEEM and NEGIS In-situ Measurements and corresponding CFM simulations

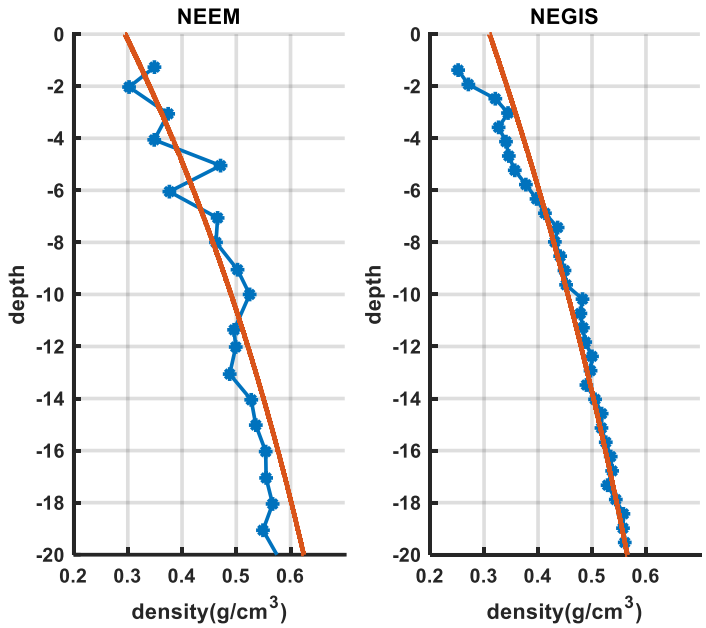

Figure 3-4: In-situ and CFM density profiles for the NEEM site In-situ and CFM density profiles (blue: ice core data, orange: fitted mean profile from CFM simulation) for the NEGIS site.

In Figure 3-4, we show the ice core measurement of NEEM(left) and NEGIS(right) plotted together with the mean profile generated from CFM. We fit the ice core data with an exponential function of depth that was then extrapolated to find the depth at which the exponential function reached 550 kg m-3. The resulting depths from NEEM and NEGIS and from the corresponding CFM simulations are shown in Table 3-3. Figure 3-4 shows reasonable agreement as observing the CFM simulated mean profile plotted together with the borehole measurements. The NEEM site shows a difference of 1.8m in the position of critical density. This is due to fitting the two stages of densities with a single exponential.

The results of this section suggest that the CFM, when run at a high time resolution, can produce firn density profiles that are in reasonable agreement with in-situ measurements. The mean profiles, as shown in the comparison, are in good agreement with the measurements.

3.2.2 Refrozen layers in the upper frin region

As stated earlier, the great melt events create refrozen layers in the “dry” zone of Greenland. In this section, we compare the Snow Radar echogram with the CFM simulated profiles. An X-ray tomography profile near location 1 collected in 2015[46] is also compared with the radar echo. Figure 3-5 plots three example radar echo profiles near location 1 in Figure 3-1, along with an echogram showing multiple profiles versus position along the flight path. Individual echo profiles show multiple significant backscatter peaks in the upper firn, but the echogram demonstrates that returns can fluctuate significantly from location-to-location CFM profile simulations also account only for large-scale climate properties in simulating firn profiles, so that a spatial average of radar measurements is also reasonable. Besides, UWBRAD measurements also correspond to a footprint of 1 km in diameter. These facts validate the averaging over 1km data.

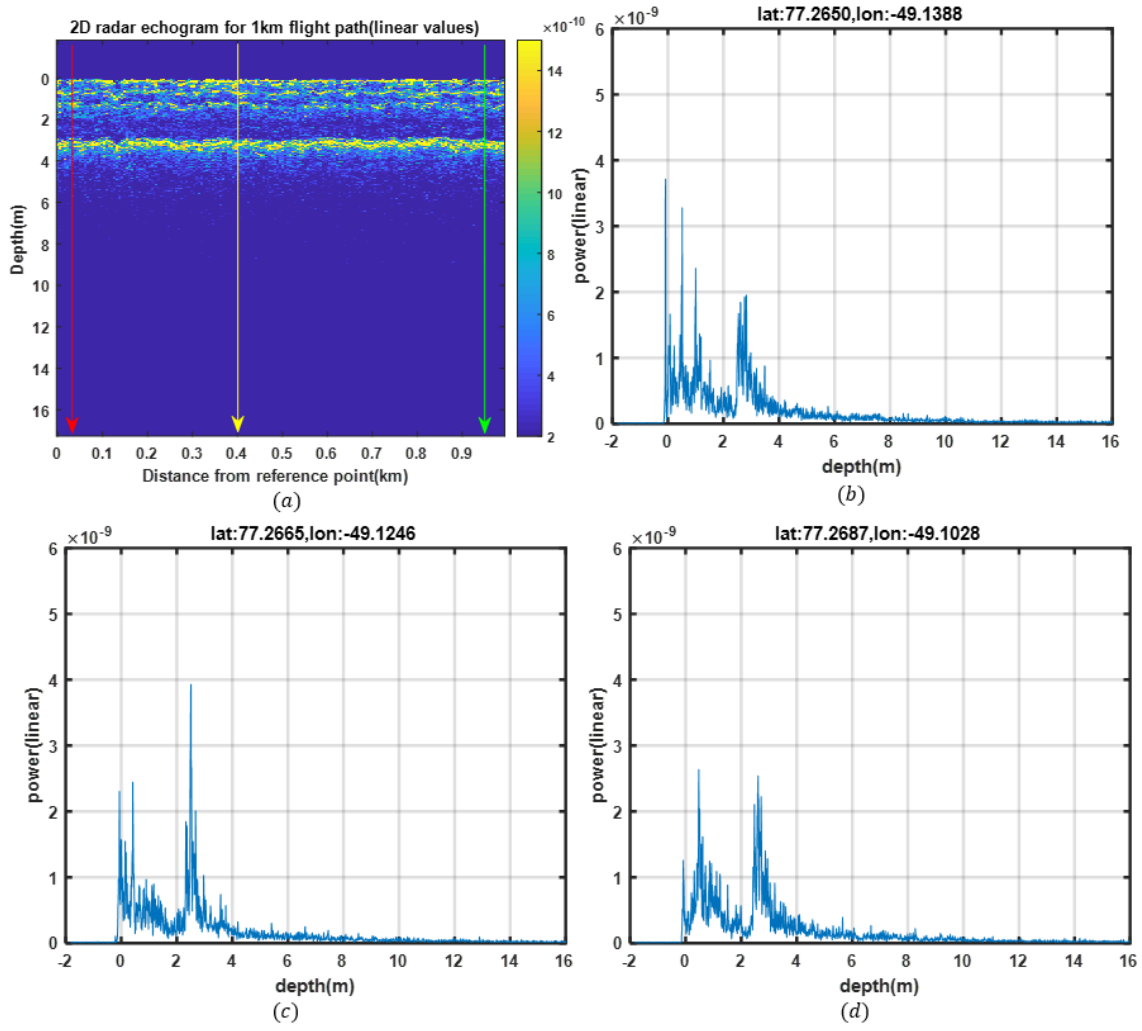

Figure 3-5 (a) Snow Radar echogram versus depth in the firn along the flight path. (Other plots) Three selected echo profiles from the echogram positions are denoted as red(b), yellow(c), and green(d). The echogram shows bright edges near the surface, which can be attributed to the refrozen layers with higher dielectric contrast.

Figure 3-6 and Figure 3-7 compare CFM simulated density profiles for cross-over locations 1-2 (Figure 3-6) and 3-4 (Figure 3-7) with the 1 km averaged radar echoes as a function of depth. All locations show secondary backscatter peaks at depths 2-2.5 m that correspond to peaks in the CFM density profiles. These peaks have amplitudes comparable to the snow-air interface, which is likely to be caused by the refrozen layers created in the melt events starting in the year of 2012. The Snow Radar also observes backscatter peaks at shallower depths that do not correspond to similar density features in the simulated profiles, potentially due to inaccuracies in the climate forcing

used for recent periods. Additional smaller backscatter peaks appear at 6-8 m depth that, in many cases, have matching CFM density peaks, but the lower level of the backscatter returns makes a direct comparison with CFM information more challenging.

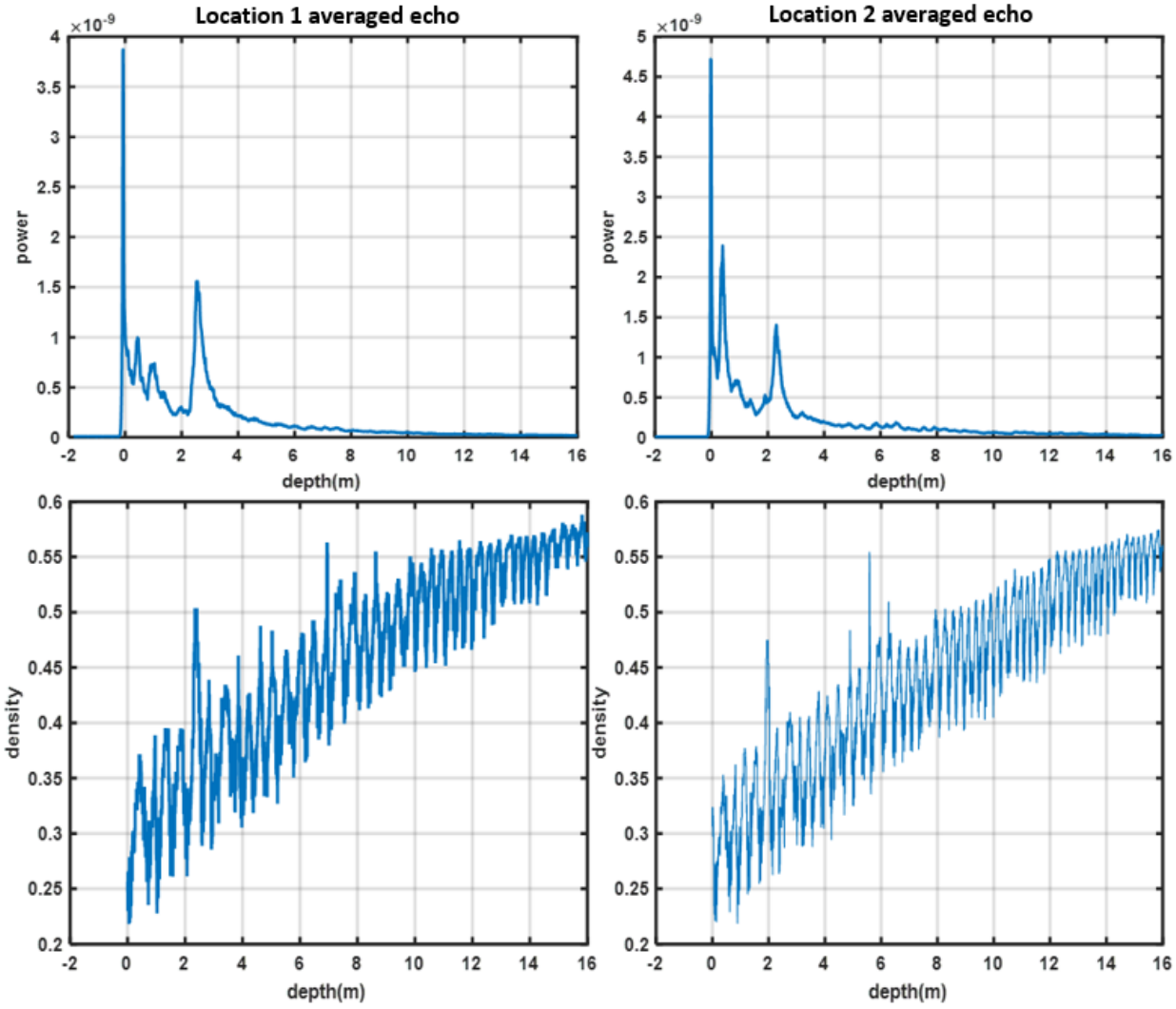

Figure 3-6 Averaged radar echos for cross-over points one and two (upper left and right plots) and corresponding CFM simulated density profiles (lower left and right plots)

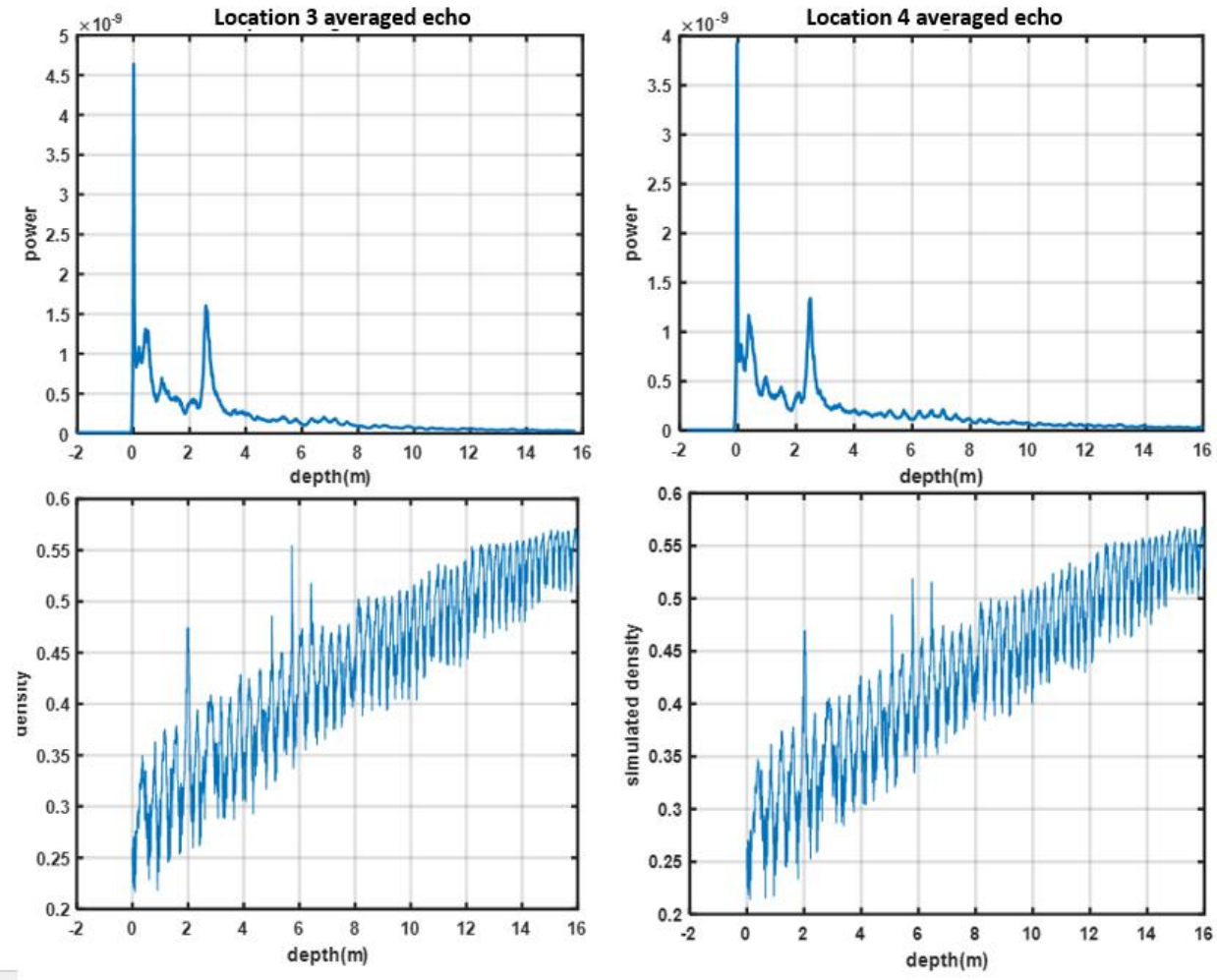

Figure 3-7 Averaged radar echoes for cross-over points three and two (upper left and right plots) and corresponding CFM simulated density profiles (lower left and right plots)

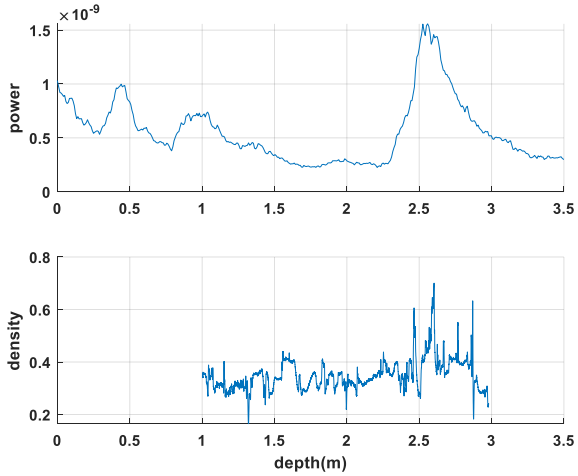

Figure 3-8 Averaged Snow Radar echo (upper plot) compared to X-ray high-resolution tomography density data (lower data) near cross-over location one

2015 X-ray tomography data providing a snapshot of the upper 2 meters of the firn for a location near cross-over location 1 is shown in Figure 3-8. The X-ray profile was shifted 1 meter in depth to compensate for snowfall between the 2015 tomography and 2017 radar measurements. The strong radar echo near 2.5m depth again collocates well with X-ray density features near this depth related to the 2012 melt event. It is noted that the tomographic profile corresponds only to a single location rather than the 1 km average used in the radar echo, so the detailed features in the tomography profile are not observed in the averaged radar measurement, although similar detailed features can be identified in some individual radar echo profiles. Table 3-4 presents a summary of the number of peaks detected in the averaged Snow Radar echogram at each of the four cross-over sites.

	Point1	Point 2	Point 3	Point 4
Number of peaks	3	2	2	2

Table 3-4: Peaks in Snow Radar echoes

The results of this section suggest that strong echoes observed by the Snow Radar are due to refrozen layers in the firn. CFM simulated density peaks are shown to correspond reasonably to the high backscatter echoes. This indicates a potential melt event happened in 2012. X-ray tomography data also shows the impact of the 2012 melt event and correlates well with radar measurements [95].

3.2.3 Studies of the impact of each density component on 0.5-2 GHz brightness temperatures

In this section, we use the radiative transfer model to study the frequency response of different components in the firn. The reflection is evaluated for long scale, short scale, and the refrozen

layers. The model was first applied to simulate the impact of "long scale" density fluctuations on 0.5-2 GHz brightness temperatures. Figure 3-9 shows example reflections resulting from long-scale firn density variations at the snow-air interface, using the parameter in Table 3-5. The maximum and minimum of the reflection within the bandwidth are 0.126 and 0.118, with a difference of 0.008. The reflection is unit less as a ratio of reflected power to incident power. The reflectivity is significant but remains approximately constant in frequency in this case.

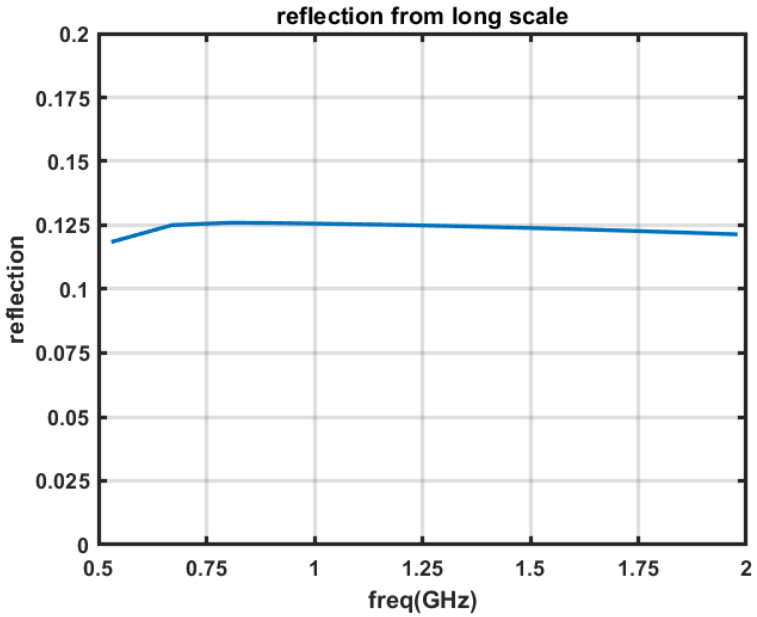

Figure 3-9 Reflections from the long scale and snow-air interface; the results are almost constant in frequency

A similar study for short-scale variations using the parameters is presented in Figure 3-10**Error! Reference source not found.**. The parameters of the $std(\rho)$ and l_z is from the results of [59]. We used a small horizontal correlation length for the short scale since these kinds of small variations are hard to pertain horizontally in the scale of 10s of centimeters. We also assume the short scale exists in a shorter vertical range due to the densification effect. The small reflectivity values obtained suggest that the contribution of short scales is negligible compared to the long scale.

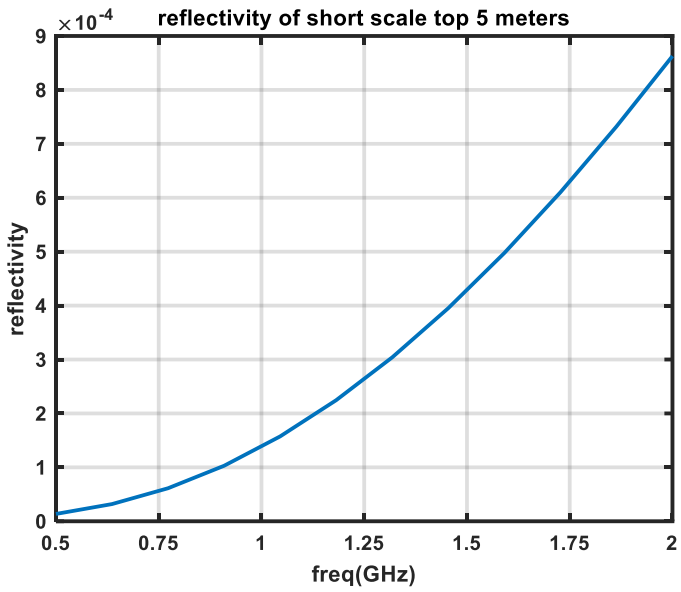

Figure 3-10 Reflectivity from short-scale fluctuations in the top five meters

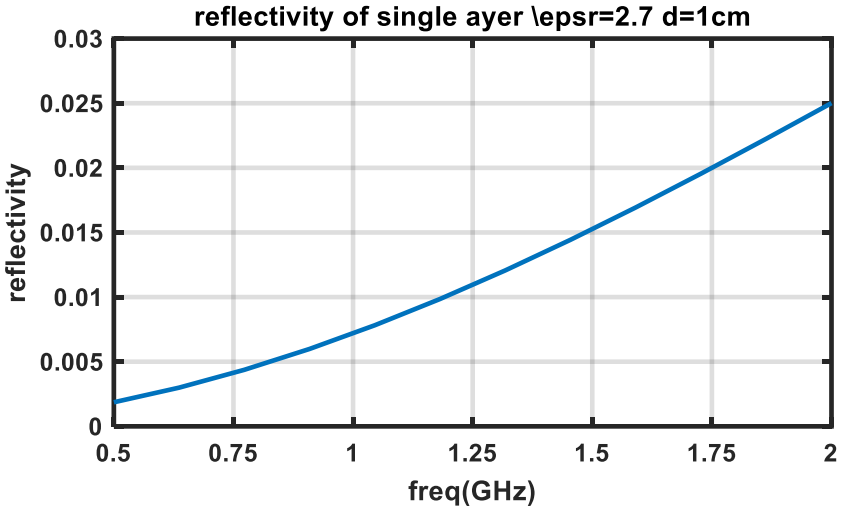

Figure 3-11 Reflectivity of a single layer with permittivity 2.7 and 1cm thickness in a mean permittivity of $\epsilon_r = 1.63$(0.35g/cm^3 in density)

The reflectivity resulting from a single refrozen layer of relative permittivity 2.7 and 1 cm thickness in a background of relative permittivity 1.63 is shown in Figure 3-11. These results show a significant variation in frequency, ranging from 0.002 to 0.025 from 0.5 to 2GHz, suggesting that refrozen layers can be important contributors to the frequency variation in 0.5-2

GHz brightness temperatures. Table 3-5 provides a further summary of insights obtained from Figures 3-9 to 3-11 and other similar simulations.

Scales Deterministic or random 3D or layered measurements	l_ρ **(not modelled by CFM, a hypotheses) , l_ρ/l_z**	**$\Delta\rho(g/cm^3)$ l_z or thickness(cm)**	**Extent in depth**	**Number of reflections**	**Reflections Magnitude (i) each (ii) Total**	**Included in Community Firn Model (CFM)?**
Short scale (random 3D) borehole	$2\ cm$ $\frac{l_\rho}{l_z}=1$	$0.01\ g/cm^3$ $2\ cm$	5m	250	2.5e-5 0.00625=250x2.5e-5	Not modeled because of small variance and small correlation length
Long scale (random 3D) borehole	23 cm $\frac{l_\rho}{l_z}=2.3$	$0.05\ g/cm^3$ $10\ cm$	30m	300	5e-4 0.15=300x5e-4	yes
Frozen layers (deterministic , 1D) From radar echo in the time domain	$l_\rho > 10\lambda$	$0.3 g/cm^3$ 1cm	2m	3	[0.002~0.025] 0.006~0.075	yes

Table 3-5: Properties of the short scale, long scale variations in density and high-density layers

With the understanding that the refrozen layers are contributing to the reflection change within the 0.5-2GHz range, we now look at the UWBRAD measurements taken at the 4 locations in Figure 3-1. Figure 3-12 plots UWBRAD 0.5, 1.1, and 1.8 GHz brightness temperatures at the four cross-over locations. The frequency variations of brightness temperatures at location one (rightmost point in Figure 3-12) are larger than the other three points, which can be related to the number of radar echo peaks at these locations (Table 3-4).

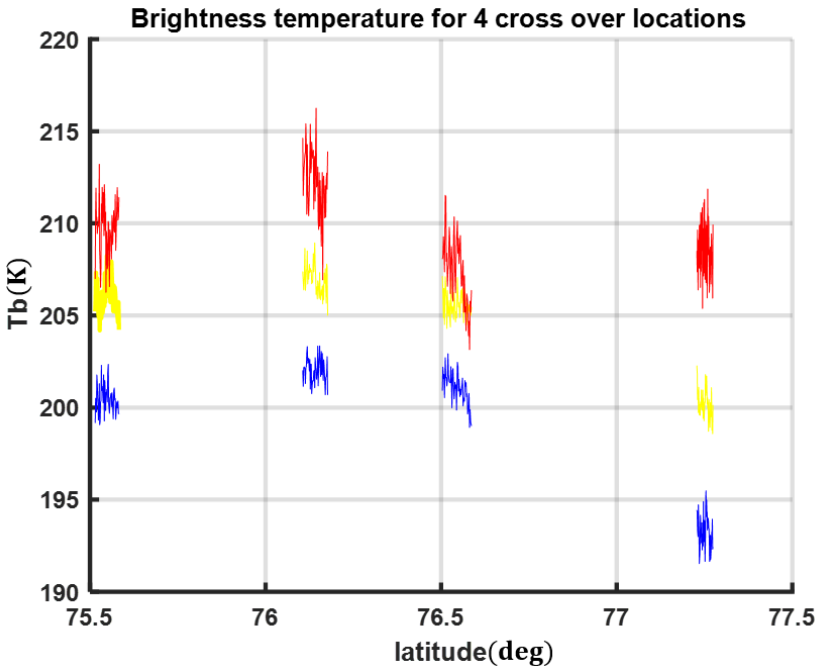

Figure 3-12 Brightness temperature for three channels of 0.5GHz (red), 1.1GHz (yellow) 1.8GHz (blue). Cross-over locations 1 to 4 are from right to left in the figure.

3.2.4 Comparisons of Modelled and Measured Brightness Temperatures

In this section, the analytical partially coherent model was first used to simulate UWBRAD-acquired brightness temperatures. Then, the input parameters are compared with the profiles from CFM simulations.

To simulate UWBRAD brightness temperatures, temperature profiles from NGRIP to NEEM retrieved in [60] (see Appendix B) are used with the partially coherent model [59] to

provide the upward going brightness temperature at depth $z = -d$. A mean profile of $\rho_m(z) = 0.917 - 0.5748\exp(0.0263z)$ is also used for all four cross-over locations based on analysis of CFM outputs for the 4 locations, which were found to have similar mean density behaviors.

An iterative process was used to refine model parameters in order to obtain a reasonable match to the UWBRAD measurements, as shown in Figure 3-13. It is noted that UWBRAD variations at these sites can be approximately 3K, so the agreement achieved is comparable to the measurement accuracy.

Table 3-6 summarizes the parameters obtained. Note that $std(\rho)$ and l_z were decreased in depth through multiplication with the functions $exp\,(z/33)$ and $exp\,(z/55)$, respectively where z is the depth in meters for the large scale and by $exp\,(z/5)$ for the short scale. Numbers in the exponential functions are in terms of meters. The selection of the exponential decay function for the $std(\rho)$ long scale is to make sure that the density fluctuations would disappear when the firn is very close to the ice. For the short scale, the decay is much faster due to densification, believing the effects are negligible. The decrease in correlation length is a tuning parameter to make sure the $std(\rho)$ becomes 0 before l_z becomes too small $(4k_m'^2 l_z^2 \ll 1)$. The horizontal correlation length for the long-scale variations was obtained as $l_\rho = 23cm$, which appears consistent with reports from in-situ investigations and is similar to the properties of firn surface horizontal variations. The permittivity and thickness of the high-density layers used in simulating the brightness temperature are also listed in Table 3-6**Error! Reference source not found.**; the number of high-density layers at each site was selected based on the radar analysis in Table 3-4.

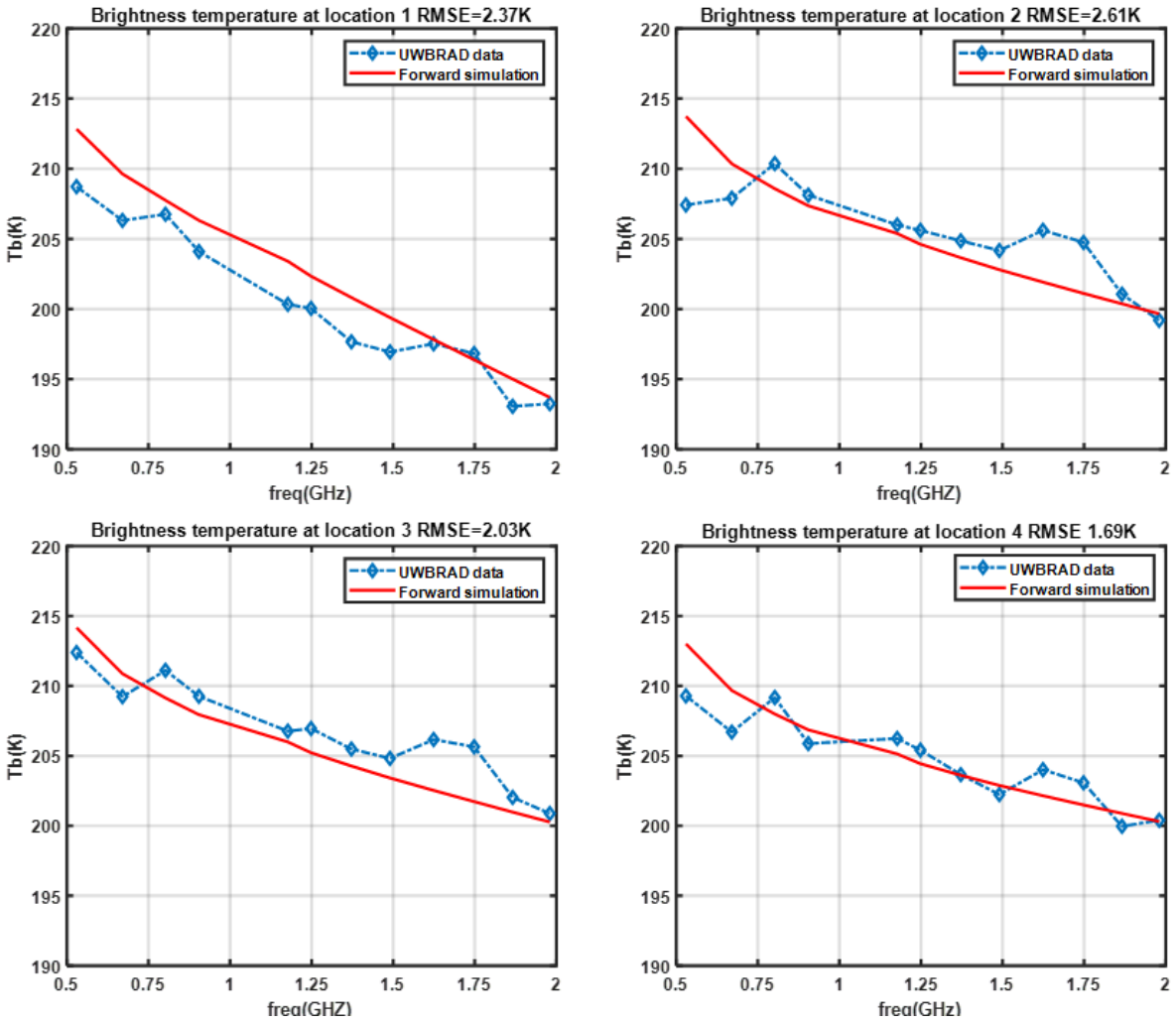

Figure 3-13 Brightness temperature over the four overlapping positions. The simulated results are plotted together with the UWBRAD data.

Long-scale density fluctuation parameters inferred from the CFM are listed in Table 3-7 **Error! Reference source not found.** for comparison. For Location 1, the microwave estimated $std(\rho)$ is $0.058g/cm\text{^}3$ with $l_z = 11.5cm$, while the corresponding values for Location 2 through four are $0.053g/cm\text{^}3$ with correlation length ~ $9cm$. The CFM results show $std(\rho)$ values of 0.036g/cm^3 with $l_z = 10.5cm$ for Location 1 and $0.033g/cm\text{^}3$ with vertical correlation length close to 7cm for the other locations. While the $std(\rho)$ used in the forward model is about 0.02g/cm^3 higher than the CFM, $std(\rho)$ values in both cases agree in the higher $std(\rho)$ and l_z values at location 1. While differences in the microwave-derived and CFM-derived density

fluctuation values are significant, the relative agreement achieved suggests that 0.5-2 GHz brightness temperatures can provide information on firn density fluctuations if refrozen layer effects are accounted for using radar-derived information.

		Location 1	Location 2	Location 3	Location 4
Long scale	$std(\rho)(z = 0)$(g/cm^3)	0.058	0.053	0.053	0.054
	$l_z(z = 0)(cm)$	11.5	9.1	9.3	9.2
Refrozen layers	Permittivity	2.6;2.7;2.7	2.6;2.7	2.6;2.7;	2.6;2.6
	Thickness (cm)	0.9,1.1,1.1	0.95,0.9	0.95,0.9	0.85,0.9

Table 3-6 Parameters used in forward modeling brightness temperature, the decrease of $std(\rho)$ and $l_z(z)$ follows $exp(z/33)$

	Location 1	Location 2	Location 3	Location 4
$std(\rho)$(g/cm^3)	0.036	0.033	0.0325	0.0325
l_z(cm)	10.5	6.2	7.14	7.2
Accumulation (m, i.e., yr^{-1})	0.293	0.148	0.148	0.193

Table 3-7: Near-surface long scale properties from CFM simulation and Accumulation rate

3.3 Discussion

Modeling the density fluctuations with a horizontal variation on the scale of wavelength enables the coupling between the emission of V and H-polarized brightness temperature. To show this effect, we compare the forward modeling results using finite l_ρ and $l_\rho = \infty$ with SMOS data collected over Dome C, Antarctica, where in-situ studies have been performed [96], [97]; The V

and H polarized brightness temperature was modeled in [63]; however, the 1D random media model could not explain the H polarized TB.

Forward model predictions were also compared with brightness temperatures at Dome C measured by the SMOS satellite. SMOS operates at 1.4 GHz and has both V and H channels. The synthetic aperture technique in SMOS makes multi-angle observations possible, as provided in the SMOS L1C data product. Firn properties at DOME C are very different from those in Greenland. The accumulation rate of Dome C is 0.1m/year [96] in contrast to the higher accumulation rates in Greenland shown in **Error! Reference source not found.**. A shorter correlation length, therefore, should be expected as compared to Greenland, and temporal effects on the firn will be less significant compared to Greenland. Refrozen layers at this site are also neglected, as significant melt events are not expected. A comparison of the firn properties used in Greenland and at Dome C is provided in Table 3-8 to summarize these discussions.

Scales	Greenland	Dome C
Short scale(z=0)	$0.01 g/cm^3$,$l_z = 2cm, l_\rho = 2cm$	No short scale
Long scale(z=0)	$0.05 g/cm^3$,$l_z = 10cm$, $l_\rho = 23cm$,$\frac{l_\rho}{l_z} = 2.3$	$0.053 g/cm^3$,$l_z = 8.2cm$,$l_\rho = 10cm$
Frozen layers	$0.3 g/cm^3$ 1cm thick, $l_\rho > 10\lambda$ Three layers,	No Frozen layers

Table 3-8: Firn properties in Greenland and at Dome C

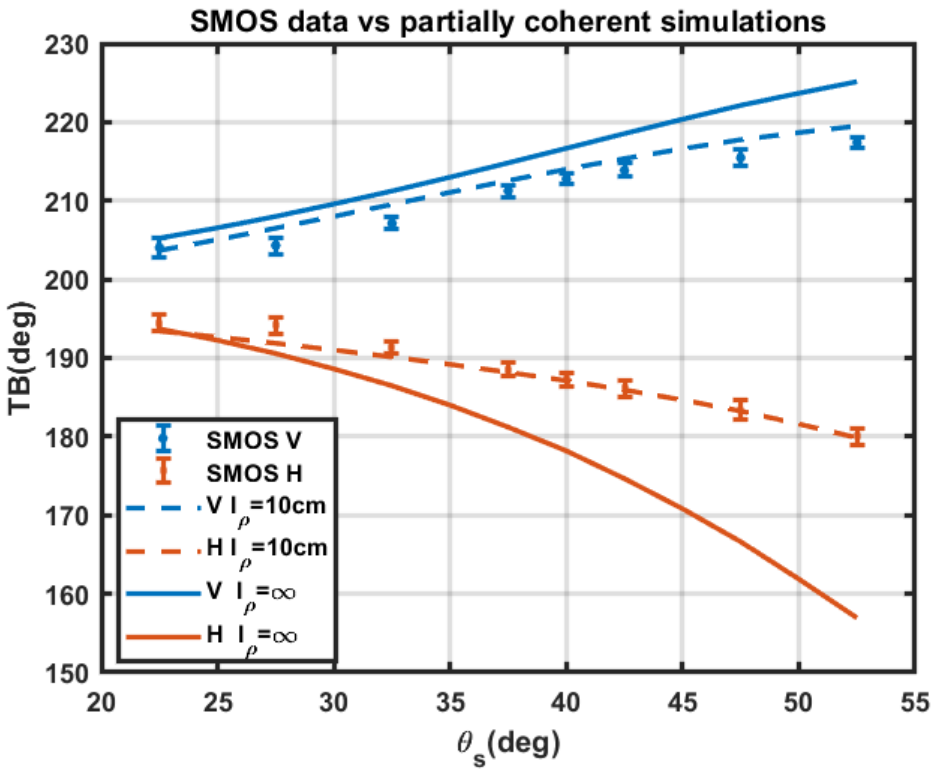

Figure 3-14 10-year averaged SMOS data compared with partially coherent model forward simulations.

Forward model predictions of 1.4 GHz brightness temperatures versus angle are shown in Figure 1-1Figure 3-14 using $l_\rho = 10cm$ and $l_\rho = \infty$, along with SMOS measurements averaged over a 10-year time period from 2011 to 2021. The SMOS error bars further indicate the expected accuracies of the SMOS data shown.

In simulating the results, the density parameters at z=0 are given in Table 3-8. The surface density fluctuation is selected between the ground measurements data at Dome C [96] and the values obtained in [97]; note that information on the density correlation length is not provided in these works. The mean profile density follows [96], and a Robin-model temperature model is used. We assume that $std(\rho)$ and l_z have dependence of exp $(z/30)$ and exp $(z/40)$ respectively to model the process of densification.

The results show that the model predictions with $l_\rho = 10cm$ provide a good agreement with SMOS data in the range 22.5- 52.5 degrees incidence angle, and with RMS difference over angle of 1.4K in V and 0.8K in H. The one dimensional $l_\rho = \infty$ results, in contrast, show up to 17K differences in the H-pol simulations. These results show that including the effects of finite horizontal correlation length allows the coupling between angle and polarization effects necessary to reproduce SMOS observations.

The analysis of UWBRAD data over Greenland and Dome-C Antarctica has shown the strong effects of density fluctuations over the brightness temperature in the L-band. This shows that the passive microwave can be used as a tool to infer the density fluctuations remotely. Previously, density properties could only be obtained by in-situ measurements (e.g., snow pit), which can only be taken over several places for a given period of time in a year. Characterizing the density fluctuation change can help characterize the mass balance of the firn, given that the elevation change of the firn can be due to the density change.

The radiative transfer model developed here can also be used to analyze the time series brightness temperature over the regions where perennial firn aquifer exists. Resolution-enhanced time series brightness temperature collected by SMAP over these regions has shown an exponential-like pattern from the end of the melting season to the early Spring of the next year [66] [67]. Physical modeling work for the V and H TB data from SMAP has been performed by [98], but the forward-modelled results show a much larger TB difference in the V and H channels. Based on the model in this paper, we can try to better interpret the SMAP observations physically.

As in the previous studies, density fluctuations have also affected the retrieval of temperature profiles of the ice sheet. The retrieval can be improved by knowing the density better.

3.4 Conclusions

The results of the work suggest a combined active and passive method for sensing long-scale fluctuations in the firn density. These fluctuations contain information on accumulation and densification within the firn. The Community Firn Model was used to generate profiles for comparison and was shown to produce simulated profiles having a reasonable agreement with in situ measurements provided that appropriate high-resolution forcing data was available. Snow Radar echo measurements were shown to provide information on refrozen layers within the firn, which could then be accounted for in analyzing 0.5-2 GHz brightness temperature datasets. The analytical partially coherent model reported was found to provide reasonable agreement with measured 0.5-2 GHz brightness temperatures by including the effects of refrozen layers and long-scale density fluctuations. Comparisons with SMOS measurements at Dome-C, in particular, demonstrate the coupling between H and V polarizations that is captured by the continuous random medium description used in the model. This work shows that the co-located active and passive microwave data can be used to infer the polar firn properties that can further be compared with CFM predictions.

Appendix A: First-Order Iterative Approach for Firn Emission

In this appendix, we give the details of the first-order solution of radiative transfer equations with a varying mean and fluctuating profile. The density profile is defined by:

$$\rho(z) = \rho_m(z) + \rho_f(z)$$

Where $\rho_m(z)$ is the mean profile, which increases as the depth increases,$\rho_f(z)$ is the fluctuating profile with the standard deviation $std(\rho_f)(z)$ and vertical correlation length $l_z(z)$ decreases as z decreases. The radiative transfer equations for the density fluctuating region are given as:

$$cos\theta \frac{\mathrm{d}}{\mathrm{dz}} \vec{T}_u(\theta, z)$$

$$= -\kappa_a(z)\vec{T}_u(\theta, z) + \kappa_a(z)T_0 - \kappa_s(\theta, z)\vec{T}_u(\theta, z)$$

$$+ \int_0^{\frac{\pi}{2}} sin\theta' P_{uu}(\theta, \theta', z)\, \vec{T}_u(\theta', z) + \int_0^{\frac{\pi}{2}} sin\theta' P_{du}(\theta, \theta', z)\, \vec{T}_d(\theta', z)$$

And

$$-cos\theta \frac{\mathrm{d}}{\mathrm{dz}} \vec{T}_d(\theta, z)$$

$$= -\kappa_a(z)\vec{T}_d(\theta, z) + \kappa_a(z)T_0 - \kappa_s(\theta, z)\vec{T}_d(\theta, z)$$

$$+ \int_0^{\frac{\pi}{2}} sin\theta' P_{ud}(\theta, \theta', z)\, \vec{T}_u(\theta', z) + \int_0^{\frac{\pi}{2}} sin\theta' P_{dd}(\theta, \theta', z)\, \vec{T}_d(\theta', z)$$

The boundary conditions are given as the following:

$$\vec{T}_d(\theta, z = 0) = \vec{r}_{10}(\theta)\vec{T}_u(\theta, z = 0)$$

And

$$\vec{T}_u(\theta, z = -d) = T_2$$

The brightness vectors contain the first and second components of the Stokes vector. In the region we consider, which is about tens of meters below the surface, the physical temperature of the firn is nearly a constant value, denoted as T_0.

The expressions for the phase functions can be found in ([61]).To find the solution, we multiply $\exp\left(-\int_{z'}^{0} \kappa_a(z'')sec\theta dz''\right)$ to the equation of upward-going intensity and integrate the equation from $z' = -d$ to $z' = z$, after some math manipulations, we have the expressions for upward as:

$$\vec{T}_u(\theta,z) = T_2 \exp\left(-\int_{-d}^{0}\kappa_a(z'')sec\theta dz''\right) + sec\theta\int_{-d}^{z} dz'\kappa_a(z')T_0\exp\left(-\int_{z'}^{z}\kappa_a(z'')sec\theta dz''\right)$$

$$- sec\theta\int_{-d}^{z} dz'\kappa_s(\theta,z')\vec{T}_u(\theta,z')\exp\left(-\int_{z'}^{z}\kappa_a(z'')sec\theta dz''\right)$$

$$+\int_{-d}^{z} dz'\exp\left(-\int_{z'}^{z}\kappa_a(z'')sec\theta dz''\left[\int_{0}^{\frac{\pi}{2}} P_{uu}(\theta,\theta',z')\vec{T}_u(\theta',z')\right.\right.$$

$$\left.\left.+\int_{0}^{\frac{\pi}{2}} P_{du}(\theta,\theta',z')\vec{T}_d(\theta',z')\right]\right.$$

for the downward intensity, we multiply the downward equation with

$\exp\left(-\int_{-d}^{z'}\kappa_a(z'')sec\theta dz''\right)$ and integrate from $z' = z$ to $z' = 0$. The downward intensity is

then obtained as follows:

$$\vec{T}_d(\theta,z)$$

$$= \overleftrightarrow{r}_{10}(\theta)T_2\exp\left(-\int_{-d}^{0}\kappa_a(z'')sec\theta dz''\right)\exp\left(-\int_{z}^{0}\kappa_a(z'')sec\theta dz''\right)$$

$$+\overleftrightarrow{r}_{10}(\theta)\exp\left(-\int_{z}^{0}\kappa_a(z'')sec\theta dz''\right)sec\theta\int_{-d}^{0} dz'\kappa_a(z')T_0\exp\left(-\int_{z'}^{0}\kappa_a(z'')sec\theta dz''\right)$$

$$+ sec\theta\int_{z}^{0}\kappa_a(z')T_0\exp\left(-\int_{z}^{z'}\kappa_a(z'')sec\theta dz''\right)dz'$$

$$-\overleftrightarrow{r}_{10}(\theta)\exp\left(-\int_{z}^{0}\kappa_a(z'')sec\theta dz''\right)sec\theta\int_{-d}^{0} dz'\kappa_s(\theta,z')\vec{T}_d(\theta,z')\exp\left(-\int_{z'}^{0}\kappa_a(z'')sec\theta dz''\right)$$

$$+\overleftrightarrow{r}_{10}(\theta)\exp\left(-\int_{z}^{0}\kappa_a(z'')sec\theta dz''\right)sec\theta\int_{-d}^{0} dz'\exp\left(-\int_{-d}^{0} dz'\kappa_a(z')sec\theta dz'\right)$$

$$\left[\int_{0}^{\frac{\pi}{2}} sin\theta' P_{uu}(\theta,\theta',z')\vec{T}_u(\theta',z') + \int_{0}^{\frac{\pi}{2}} sin\theta' P_{du}(\theta,\theta',z')\,\vec{T}_d(\theta',z')\right]$$

$$-sec\theta\int_{z}^{0}\kappa_s(\theta,z')\vec{T}_d(\theta,z')\exp\left(-\int_{z}^{z'}\kappa_a(z'')sec\theta dz''\right)dz'$$

$$+sec\theta \int_z^0 \exp\left(-\int_z^{z'} \kappa_a(z'')sec\theta dz''\right)\left[\int_0^{\frac{\pi}{2}} sin\theta' P_{ud}(\theta,\theta',z')\vec{T}_u(\theta',z')\right.$$

$$\left.+\int_0^{\frac{\pi}{2}} sin\theta' P_{ud}(\theta,\theta',z')\vec{T}_d(\theta',z')\right]$$

The zeroth order solution for the upward and downward intensities are given as:

$$\vec{T}_u^{(0)}(\theta,z) = T_2 \exp\left(-\int_{-d}^0 \kappa_a(z'')sec\theta dz''\right)$$

$$+ sec\theta \int_{-d}^z dz'\kappa_a(z')T_0 \exp\left(-\int_{z'}^z \kappa_a(z'')sec\theta dz''\right)$$

And

$$\vec{T}_d^0(\theta,z)$$

$$= \overleftarrow{r}_{10}(\theta)T_2 \exp\left(-\int_{-d}^0 \kappa_a(z'')sec\theta dz''\right)\exp\left(-\int_z^0 \kappa_a(z'')sec\theta dz''\right)$$

$$+\overleftarrow{r}_{10}(\theta)\exp\left(-\int_z^0 \kappa_a(z'')sec\theta dz''\right)sec\theta \int_{-d}^0 dz'\kappa_a(z')T_0 \exp\left(-\int_{z'}^0 \kappa_a(z'')sec\theta dz''\right)$$

$$+ sec\theta \int_z^0 \kappa_a(z')T_0 \exp\left(-\int_z^{z'} \kappa_a(z'')sec\theta dz''\right)dz'$$

The first-order solution of the upward intensity is given as

$$\vec{T}_u^{(1)}(\theta,z) = -sec\theta \int_{-d}^z dz'\kappa_s(\theta,z')\vec{T}_u^{(0)}(\theta,z')\exp\left(-\int_{z'}^z \kappa_a(z'')sec\theta dz''\right)$$

$$+ sec\theta \int_{-d}^0 dz' \exp\left(-\int_{z'}^0 \kappa_a(z'')sec\theta dz''\right)\left[\int_0^{\frac{\pi}{2}} sin\theta' P_{uu}(\theta,\theta',z')\vec{T}_u^{(0)}(\theta',z')\right.$$

$$\left.+\int_0^{\frac{\pi}{2}} sin\theta' P_{du}(\theta,\theta',z')\vec{T}_d^{(0)}(\theta',z')\right]$$

The specific intensity at $z = 0$ is then given as:

$$\vec{T}_u(\theta, z = 0) = \vec{T}_u^{(0)}(\theta, z = 0) + \vec{T}_u^{(1)}(\theta, z = 0)$$

Appendix B: Robin Model Parameters for the Four Locations

This Appendix presents the Robin model input parameters for the 4 locations

Table 3-9 Robin parameters for firn physical temperature

	Total ice thickness	Surface Temp	M	G
Pt1	2656	242.5	0.38	0.0886
Pt2	3155	241.9	0.21	0.06
Pt3	2951	241.5	0.235	0.095
Pt4	3045	241.3	0.295	0.095

Chapter 4 Full Wave Simulation of Firn Aquifer Effective Permittivity

In this chapter, the effective permittivity of the perennial firn aquifer at L-band (1.4GHz) is studied using a full-wave simulation approach. The methodology is first discussed. The validity of the Finite Element Method (FEM)[99], Finite Difference Frequency Domain method[100] and Volume Integral Equation method with Discrete Dipole Approximation[86] is examined. The FEM method is commercially available through the ANSYS HFSS[101]. These numerical approaches are first validated by comparing the scattered field with the Mie scattering results of a homogenous dielectric sphere. Then, the methods are used to calculate the scattered field and the absorbed power of the random media. With the bic-media modeled firn aquifer structure, full wave simulations provide a permittivity that is different from the classical mixing formula results using pre-assumed inclusion shapes.

4.1 Methodology of Determining Equivalent Permittivity

To evaluate the effective permittivity of complex mixing structures, two scattering problems, problems A and B, as shown in Figure 4-1, need to be solved. Figure 4-1 (a) on the left represents problem A. The figure describes a random media placed in an artificial spherical boundary of diameter D. The black is the inclusion with permittivity ϵ_p and the white is the back ground media as ϵ_b. In our problem, the back ground media is either ice or air with the inclusions as water and ice-water mixture for firn aquifer and wet snow, respectively. A plane wave shines on the structure. Using the numerical solvers, the scattering field $E_s(\theta_s, \phi_s)$ into every direction and the internal field E_t in the inclusions are calculated. In Problem B, a homogeneous sphere with permittivity

ϵ_eff is considered. The scattered field and internal field can be obtained from analytical solutions using Mie scattering theory.

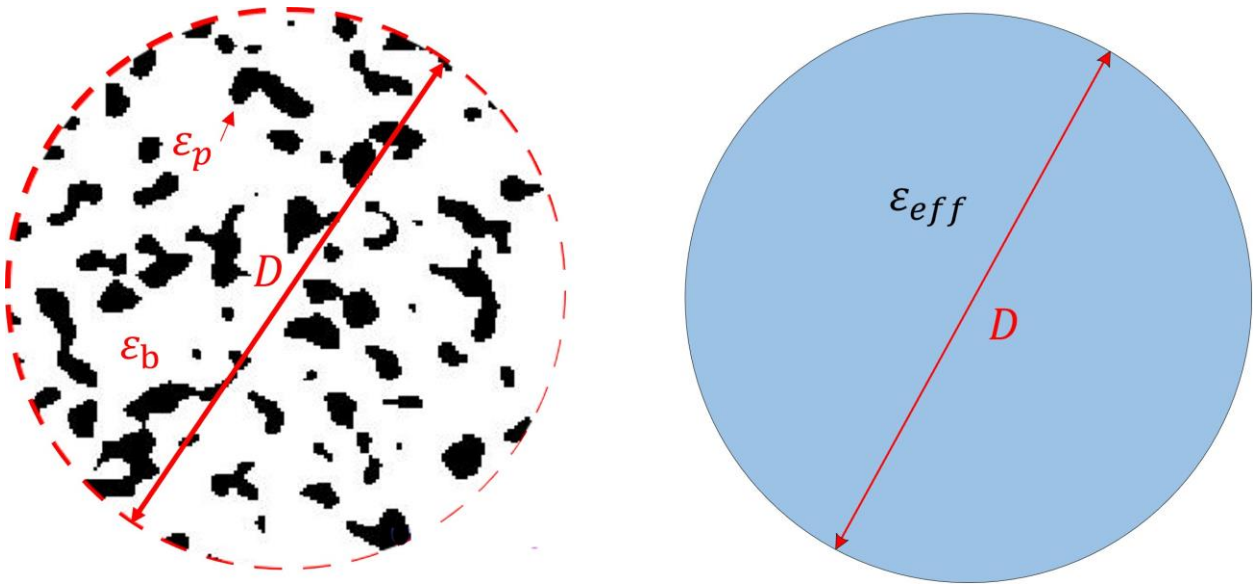

Figure 4-1 Problem A(left) and Problem(B) right. In Problem A, we place the random media in an artificial spherical boundary with diameter D. The background is with permittivity ϵ_b whether inside or outside the artificial boundary. The inhomogeneity is with permittivity ϵ_p. Plane wave incident on the object and thus the scattered wave and absorbed power are calculated for many realizations. The scattered fields and absorbed power are averaged over the multiple realizations to obtain the normalized scattering and absorption cross-sections. We then solve Problem B, the homogenous sphere with diameter D, analytically using the Mie scattering theory. We gradually change the permittivity to fit the normalized scattering and absorption cross sections that are from Problem A to find the effective permittivity of Problem A

In the topic of remote sensing, the sense of "equivalent permittivity" is more about the ability of scattering and absorption. Such abilities can be represented by the quantities of normalized scattering cross-section Q_{scat} and the normalized absorption cross-section Q_{abs} The generation expression for Q_{scat} and Q_{abs} are provided in equations (4-1) and (4-2).

The scattering Q_{scat} is:

$$Q_{scat} = \frac{1}{\pi\left(\frac{D}{2}\right)^2}\int_0^{4\pi} \left|f_{pp}(\theta_s,\phi_s)\right|^2 + \left|f_{qp}(\theta_s,\phi_s)\right|^2 d\Omega \qquad (4\text{-}1)$$

Where D is the diameter of the boundary, $f_{pp}(\theta_s, \phi_s)$ and $f_{qp}(\theta_s, \phi_s)$ are the scattering amplitudes for a p-polarized incident wave with p and q scattering wave polarizations as provided in the definition of scattering amplitude.

$$\begin{bmatrix} E_p^s \\ E_q^s \end{bmatrix} = \frac{e^{ikr}}{r} \begin{bmatrix} f_{pp} & f_{pq} \\ f_{qp} & f_{qq} \end{bmatrix} \begin{bmatrix} E_p^i \\ E_q^i \end{bmatrix}$$

The absolute values squared scattering amplitude is integrated over all solid angles, which means that the scattered fields in all directions are included in evaluating Q_{scat}.

Q_{abs} is calculated by the following volume integral:

$$Q_{abs} = \frac{k}{\pi(D/2)^2} \int \epsilon''(\vec{r}) |E_{int}(\vec{r})|^2 dV \qquad (4\text{-}2)$$

where ϵ'' is the imaginary part of the permittivity of the particle and E_{int} is the internal electric field.

The concept of effective permittivity is characterizing the mean statistical properties. Thus, for problem A, we use the Monte Carlo method to generate independent samples of the random media. The averaged scattered wave from the independent samples is used to calculate Q_{scat}^A. Q_{abs}^A is obtained by averaging over several realizations of the random media to capture the statistical mean. Detailed mathematical expressions are provided below.

For the scattering, we replace the $f_{pp}(\theta_s, \phi_s)$and $f_{qp}(\theta_s, \phi_s)$ with $\langle f_{pp}(\theta_s, \phi_s)\rangle$and $\langle f_{qp}(\theta_s, \phi_s)\rangle$ where:

$$\langle f_{pp}(\theta_s, \phi_s)\rangle = \frac{1}{N} \sum_{n=1}^{N} f_{pp}^n(\theta_s, \phi_s)$$

$$\langle f_{qp}(\theta_s, \phi_s)\rangle = \frac{1}{N} \sum_{n=1}^{N} f_{qp}^n(\theta_s, \phi_s)$$

are the averaged scattering amplitude from N realization of the random media.

As a result of this, Q_{scat}^{A} is expressed as the following:

$$Q_{scat}^{A} = \frac{1}{\pi\left(\frac{D}{2}\right)^{2}} \int_{0}^{4\pi} \left|\langle f_{pp}(\theta_s, \phi_s)\rangle\right|^{2} + \left|\langle f_{qp}(\theta_s, \phi_s)\rangle\right|^{2} d\Omega \qquad (4\text{-}3)$$

The normalized absorption cross section is obtained by averaging the quantity over the N realizations as:

$$Q_{abs}^{A} = \frac{1}{N}\sum_{n=1}^{N} Q_{abs}^{n} \qquad (4\text{-}4)$$

For problem B, we have a homogeneous sphere with permittivity. ϵ_{eff}. The normalized scattering and absorption cross-section can be obtained directly by analytical Mie scattering theory as $Q_{scat}^{B}$and Q_{abs}^{B}respectively. To find the effective permittivity of the random media represented in Problem A, we need to change the permittivity of the sphere in Problem B until we can let $Q_{scat}^{B}$and Q_{abs}^{B}matches with $Q_{scat}^{A}$and Q_{abs}^{A}.

The flow chart in Figure 4-2 shows the process of finding the effective permittivity of the random media provided in Problem A. After having the $Q_{scat}^{A}$and Q_{abs}^{A}we set an initial value of $\epsilon_{eff}$to the sphere in problem B. From Mie scattering, the $Q_{scat}^{B}$and Q_{abs}^{B} are obtained. We then calculate the sum of the absolute values of relative error as:

$$error_{rel} = \left|\frac{Q_{scat}^{A} - Q_{scat}^{B}}{Q_{scat}^{A}}\right| + \left|\frac{Q_{abs}^{A} - Q_{abs}^{B}}{Q_{abs}^{A}}\right|$$

The effective permittivity would be considered found if the relative error $error_{rel}$ is smaller than the required error criterion. Otherwise, the permittivity of the sphere in problem B is adjusted in the next trial. The permittivity values in the trials for Problem B are from 1+0i to 10+5i

with small steps in the real and imaginary parts. In our practice, we found that using the error is more sensitive to the image part of ϵ. Therefore, for the imaginary part, the step can be set as 10^{-4} and the real part can be set as 10^{-3} in order to obtain an error of less than 2%.

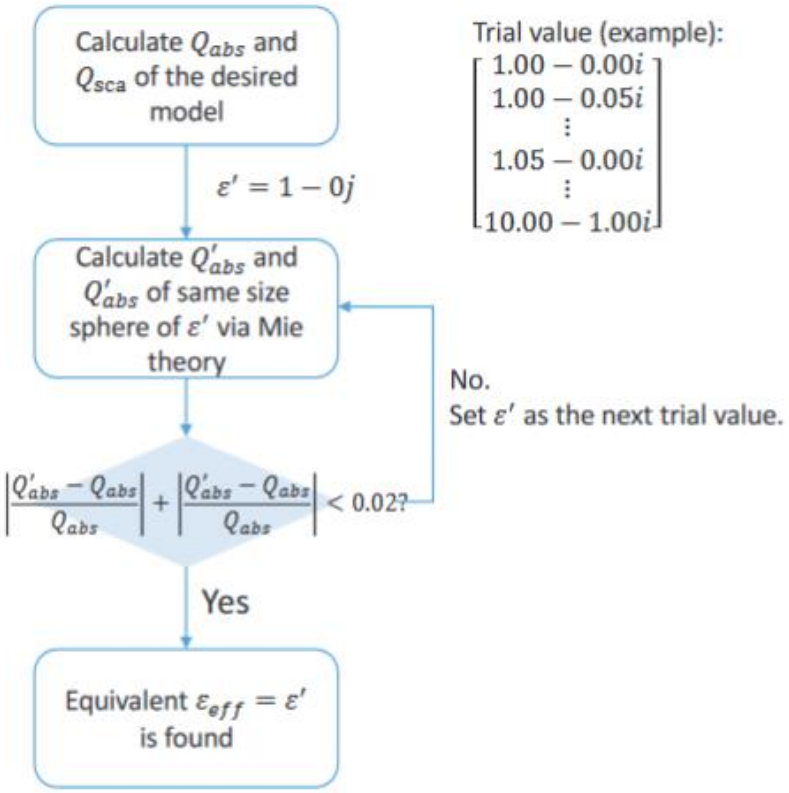

Figure 4-2 flow chart that describes the matching process to find effective permittivity

4.2 Generation of random media

In this section, the generation of random media is discussed. In this paper, three kinds of random media will be used: randomly positioned spheres, bi-continuous media, and tri-continuous media. The random spheres are used to validate the correctness of the method in comparison with the classical mixing formula. The bi-continuous media and tri-continuous media are used to model the geometry of the firn aquifer and wet snow.

4.2.1 Random Positioned Spheres

There are two methods to generate the randomly positioned spheres: one is the sequential addition method, and the other approach is the Metropolis technique [86]. The randomly positioned spheres have a pair distribution function that can be analytically obtained by the following equations:

$$(2\pi)^3 n_0 C_{PY}(p,b,f) = 24f\left\{\frac{\alpha+\beta+\delta}{u^2}cosu - \frac{\alpha+2\beta+4\delta}{u^3}\,sinu - \frac{2(\beta+6\delta)}{u^4}cosu + \frac{2\beta}{u^4} + \frac{24\delta}{u^5}sinu + \frac{24\delta}{u^6}(cosu-1)\right\}$$

$$H(p) = \frac{C_{PY}(p)}{1 - n_0(2\pi)^3 C_{PY}(p)}$$

$$g(r) = 1 + 4\pi\int_0^\infty dpp^2\left(\frac{sinpr}{pr}\right)H(p) \qquad (4\text{-}5)$$

where $C_{PY}(p)$ is the Fourier transform of the direct correlation function of Percus-Yevick hard spheres[86].$H(p)$ is the Fourier transform of the total correlation function. In the equation, several parameters need to be specified:

$$f = \frac{n_0 \pi b\text{^}3}{6}$$

$$\alpha = \frac{(1+2f)^2}{(1-f)^4}$$

$$\beta = -6f\frac{(1+f/2)^2}{(1-f)^4}$$

$$\delta = \frac{f(1+2f)^2}{2(1-f)^4}$$

$$u = pb$$

Where in the equations above, f is the volume fraction, n_0 is the number of particles per unit volume. b is the diameter of the particle. Usually, in generating the randomly positioned particles,

we need to define the volume fraction f_v and the particle number per unit volume n_0 first. The particle diameter is then defined. In the equations that describe the Fourier transform of direct and total correlation functions, p is the wave number.

For the sequential method, the positions of the spheres are generated as random numbers within a given volume. The newly added sphere needs to be checked with the other spheres to avoid overlapping; otherwise, the addition is not allowed, and the position of the sphere needs to be generated again. This method is simple to realize and is efficient for low-volume fraction cases. However, when the volume fraction of the particles is relatively high (e.g., 20%), this method may take many runs without meeting the volume fraction requirement.

Thus, to overcome this limit, the Metropolis method[86] is used to generate higher volume fractions of spheres. The approach takes the following steps:

Step (1): Consider the spheres placed randomly in a cubic volume with all three dimensions from [0,l] where l is the length of the cubic volume, N particles that meet the volume fraction requirement are placed inside.

Step (2) Change the system configuration by random displacement of the particles. The displacement of a particle to a new trial position is determined according to:

$$x \to x + \Delta\eta_1, y \to y + \Delta\eta_2, z \to z + \Delta\eta_3$$

where x,y, and z are the particle coordinates, and Δ is the maximum displacement allowed in each movement. η_1, η_2, η_3 are independent random numbers uniformly distributed within $[-l, l]$. Thus, after a displacement, the particle is equally likely to be anywhere inside $2l\Delta$, centered about its original position. Notice that there is a periodic boundary condition on all the boundaries of the cubic volume, which means that when the sphere is outside the boundary after the movement, it

enters the volume from the other side. The displacement Δ determines the acceptance rate,A_c, if Δ is too large, most of the displacements will be rejected.

Step (3): Check whether the displacements are accepted. If the displaced particle does not overlap with one of the other particles, the displacement is accepted, and the coordinates of the displaced particle are updated. Otherwise, the displacement is rejected, and the particle returns to its original position.

Step (4): Update the number of configurations generated. A new configuration means that every particle has to be subject to a single attempted displacement, even some of the displacements are not allowed. When all the particles have attempted to move once, we consider this as a configuration. Every N_c configuration is called a realization. Between 2 different realizations, every particle has been displaced on average of $N_c A_c$ times.

Step (5): Count the frequency of occurrence of different pair separations. Calculate the particle number in the range of $r + dr$ as a function of r, where r is the distance from a tagged particle. Many realizations are used to calculate the averaged pair distribution function.

The above process is repeated a large number of times to generate many different realizations and to record the frequency of occurrence of different pair separations.

An example of the generated randomly positioned non-sticky spheres is presented in Figure 4-3. To confirm that the generated random spheres follow the pair distributions that (4-5) predicts, we plot the pair distribution function from the analytical calculation and the Monte Carlo simulations together in Figure 4-4.

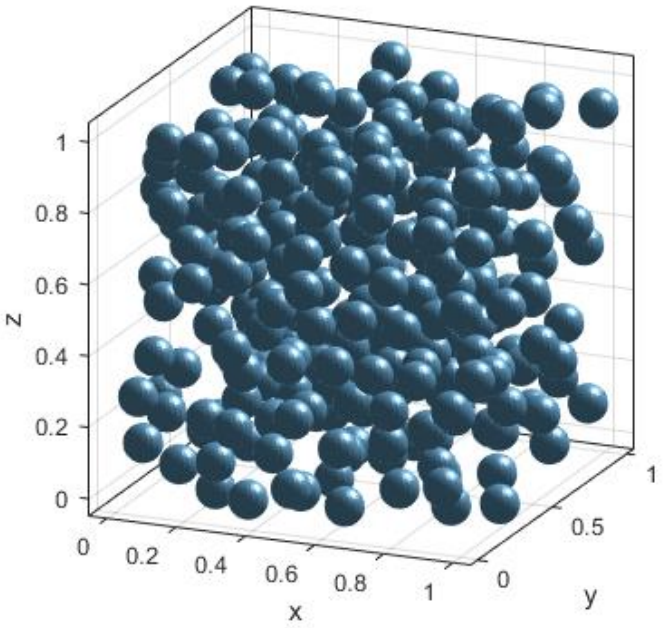

Figure 4-3 Computer-generated randomly positioned particles. The particles are randomly positioned without adhering to each other.

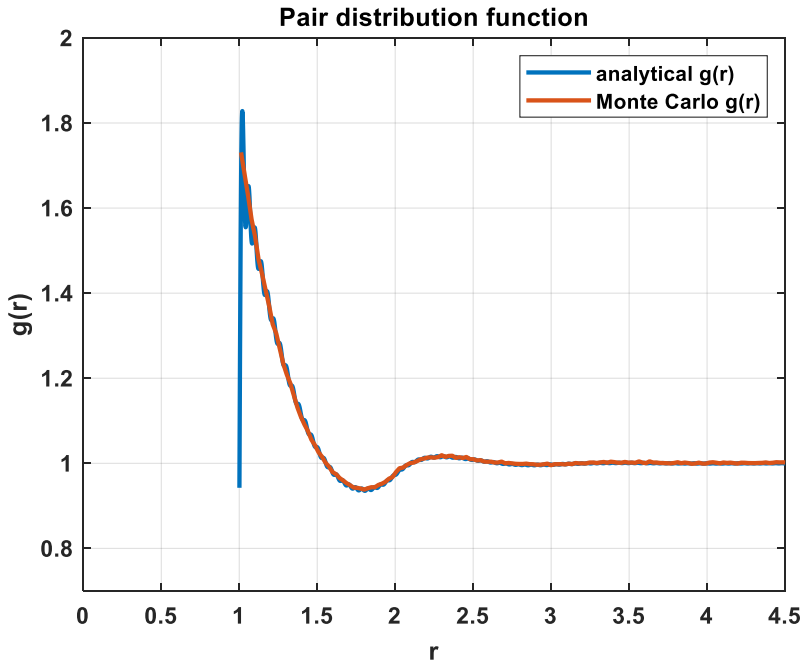

Figure 4-4 Pair distribution functions from analytical calculation and Monte Carlo simulations. The two agree well with each other. This confirms that the Monte Carlo method generates randomly positioned particles without stickiness.

4.2.2 Generation of Bi-Continuous media

The bi-continuous model is used to model the morphologies of random porous structures. Due to its similarity with the naturally formed geometry structure, research has been performed to simulate the properties of random structures by these kinds of structures. For the purpose of remote sensing theory studies, bi-continuous media is used to study the scattering of snow. In the beginning, the scattering of the unit volume of ice/air bi-continuous media is studied to find the phase matrix and absorption cross section as input to the radiative transfer equations. The calculation is based on the volume integral equation with discrete dipole approximation. Later, DDA is applied to larger snow packs in order to perform a full-wave simulation of snow. Active and passive microwave signatures are studied.

As mentioned previously, firn is obtained by the accumulation of snow. Filled with water in the pores, the firn aquifer is believed to have structures similar to those of the bi-continuous medium. Although there are no direct observations of the firn aquifer structure, microscopic studies of dry firn have indicated a similar structure with the computer-generated bi-continuous media.

Bi-continuous media[85] is obtained by leveling off the summation of random standing waves expressed as:

$$S(\vec{r}) = \frac{1}{\sqrt{N}} \sum_{n=1}^{N} \cos\left(\overrightarrow{\zeta_n} \cdot \vec{r} + \phi_n\right)$$

Where the unit vector of $\hat{\zeta_n}$ is randomly distributed over all directions. ζ_n is the wave number that is randomly distributed from 0 to ∞. Phase ϕ_n is uniformly distributed from 0 to 2π. The probability density of ζ is chosen as a gamma distribution:

$$p(\zeta) = \frac{1}{\Gamma(b+1)} \frac{(b+1)^{b+1}}{\langle\zeta\rangle} \left(\frac{\zeta}{\langle\zeta\rangle}\right)^{b} \exp\left(-(b+1)\frac{\zeta}{\langle\zeta\rangle}\right)$$

where $\Gamma()$ is the gamma function and $\langle\zeta\rangle$ is the mean value of the wave number. Physically speaking, the value of $\langle\zeta\rangle$ is inversely related to the mean particle size since when $\langle\zeta\rangle$ is large, high-frequency waves are expected to sum up together. Values of $S(\vec{r})$ is changing fast. The standard deviation of the wavenumber ζ is provided as:

$$\Delta = \frac{\langle\zeta\rangle}{\sqrt{b+1}}$$

The equation indicates that for a given $\langle\zeta\rangle$, the larger the b value, the more the distribution of particle sizes is centered near the mean value.

As discussed previously, the firn aquifer is a mixture of ice and water. The positions of ice and water are determined as follows:

$$S(\vec{r}) = \begin{cases} water, S(\vec{r}) > \alpha \\ ice, otherwise \end{cases}$$

Where α is the threshold and can be related to the volume fraction of water by:

$$f_{water} = \frac{1}{2}[1 - \mathrm{erf}(\alpha)]$$

An example of the firn structure has already been provided in Chapter 1. A comparison of the simulated bi-continuous media with the microscopic photo is provided here. It can be observed that the simulated media is consistent with the in-situ measurements. In modeling the aquifer, the permittivity of water is set as $85 + 10i$, which is a typical value of pure water in L-band. The

permittivity of ice is set as 3.2. We ignore the imaginary part of ice for this problem since it is quite small(10^-3) compared with the loss factor of water.

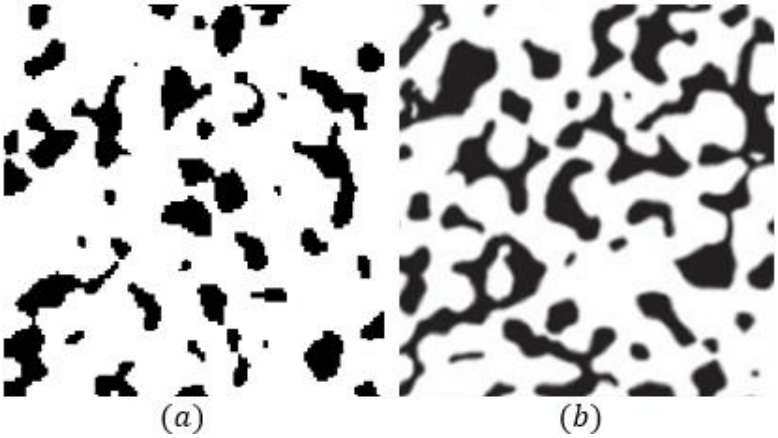

Figure 4-5 Computer-generated random media(a) in comparison with microscopic firn structure(b). The bi-continuous media shows consistency with in situ measurements

4.3 Classical mixing formulas

Classical mixing formulas are developed with pre-defined inclusion shapes. The commonly used inclusion shapes are spheres, discs, and needles. The analytical solutions of the effective permittivity should be obtained by the full wave approach once the assumptions are validated. We would use the simplest inclusion shape, sphere, to validate the approach discussed in the methodology session. The results are also compared with the full-wave simulation results for the bi-continuous media-modeled aquifer.

4.3.1 Maxwell Garnett mixing formula

The Maxwell Garnett mixing formula was developed to find the equivalent permittivity of composites for the inhomogeneities with permittivity ϵ_p appear in a background media with permittivity ϵ_b. Starting from the classical relationship of

$$\langle D \rangle = \epsilon_{eff} \langle E \rangle + \langle P \rangle$$

The famous Clausius-Mossotti formula can be obtained as:

$$\frac{\epsilon_{eff} - \epsilon_b}{\epsilon_{eff} + 2\epsilon_b} = \frac{n_0 \alpha}{3\epsilon_b}$$

Where ϵ_{eff} is the effective permittivity of the mixture, and n is the density of the number of inclusion particles in a unit volume. α is the polarizability that relates the external electric field to the dipole moment of the small particles.

In the case of small spheres, we have the expression as:

$$\frac{\epsilon_{eff} - \epsilon_b}{\epsilon_{eff} + 2\epsilon_b} = f\frac{\epsilon_p - \epsilon_b}{\epsilon_p + 2\epsilon_b}$$

This is a widely used formula to evaluate the permittivity of a mixture.

For the cases of non-spherical inclusions, the depolarization factor as $A_u, u = x, y, z$ are calculated by performing the following elliptical integral[75,77,102]:

$$A_u = \frac{abc}{2}\int_0^\infty \frac{dx}{(s+u^2)[(s+a^2)(s+b^2)(s+c^2)]^{1/2}}$$

Where $u = a, b\ or\ c$ for x,y,z axis.

For spheres, $A_a = A_b = A_c = \frac{1}{3}$

For circular discs, we have:

$$A_a = A_b = 0, A_c = 1$$

For needles, we have:

$$A_a = A_b = 0.5, A_c = 0$$

The permittivity of randomly oriented discs and needles can be evaluated using the following two equations[75]:

$$\epsilon_{eff}^{needle} = \epsilon_b + f(\epsilon_p - \epsilon_b)\frac{\epsilon_p + 5\epsilon_b}{(3-2f)\epsilon_p + (3+2f)\epsilon_b}$$

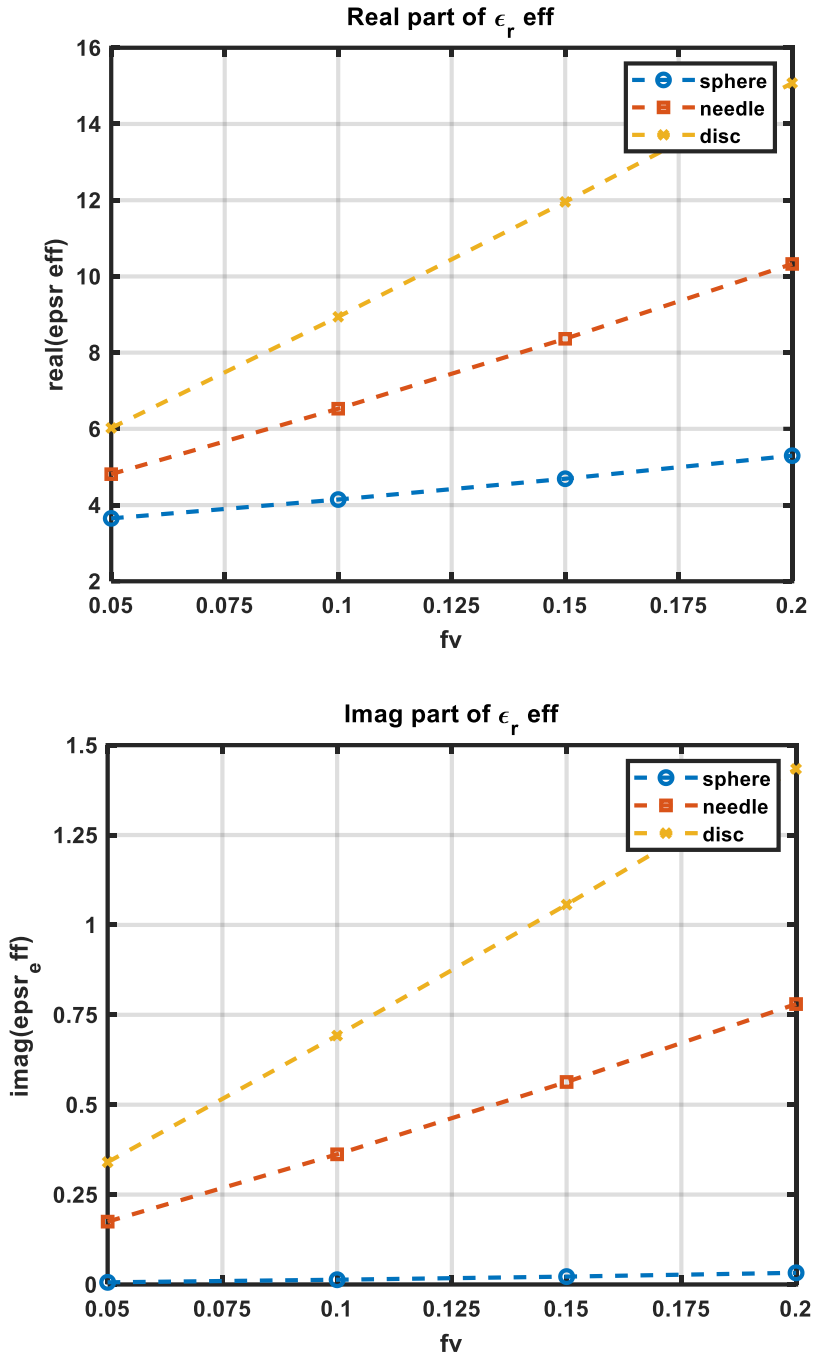

Figure 4-6 Effective permittivity plots of ice-water mixture using Maxwell Garnett mixing formula with the water inclusions shapes of spheres, needles, and discs. In the comparison of the different inclusions, the real part of disc inclusions can be three times that of the sphere inclusion case, and the imaginary part can have a 50 times difference.

$$\epsilon_{eff}^{disc} = \epsilon_b + f(\epsilon_p - \epsilon_b)\frac{2\epsilon_p + \epsilon_b}{(3-f)\epsilon_p + f\epsilon_b}$$

The effective permittivity values from the three shapes are plotted for the mixture of ice and water with the liquid water content of water from 0.05 to 0.2.

The different shapes of inclusions have major differences in evaluating the permittivity. As shown in Figure 4-6, there can be large differences in the predicted value of effective permittivity with different inclusion shapes used for the particles.

For the case of a mixture of multi-materials, formulas are available in [75].

4.3.2 Polder Van Santen/De Loor Formula

Different from the Maxwell Garnett mixing formula, where the holding media has a permittivity ϵ_b, the Polder-van Santen formula does not have a host-versus-guest hierarchy. Instead, mixed media itself is considered as the background for the two components.

For spherical inclusions, the permittivity is obtained by the following[77]:

$$\epsilon_{eff} = \epsilon_b + 3f\epsilon^* \frac{\epsilon_p - \epsilon_b}{\epsilon_p + 2\epsilon^*}$$

Where f is the volume fraction of inclusion. ϵ^* is the permittivity of material that immediately surrounds a particle. When the volume fraction is small ($f < 0.2$), ϵ^* is set as the background permittivity ϵ_b. For large volume fractions ($f > 0.8$), ϵ^* is set as ϵ_{eff}. For the range of $0.2 < f < 0.8$, the permittivity value is between the evaluations of using ϵ_b and ϵ_{eff}. Usually, setting $\epsilon^* = \epsilon_b$ tends to underestimate the value while $\epsilon^* = \epsilon_{eff}$ tends to overestimate the permittivity.

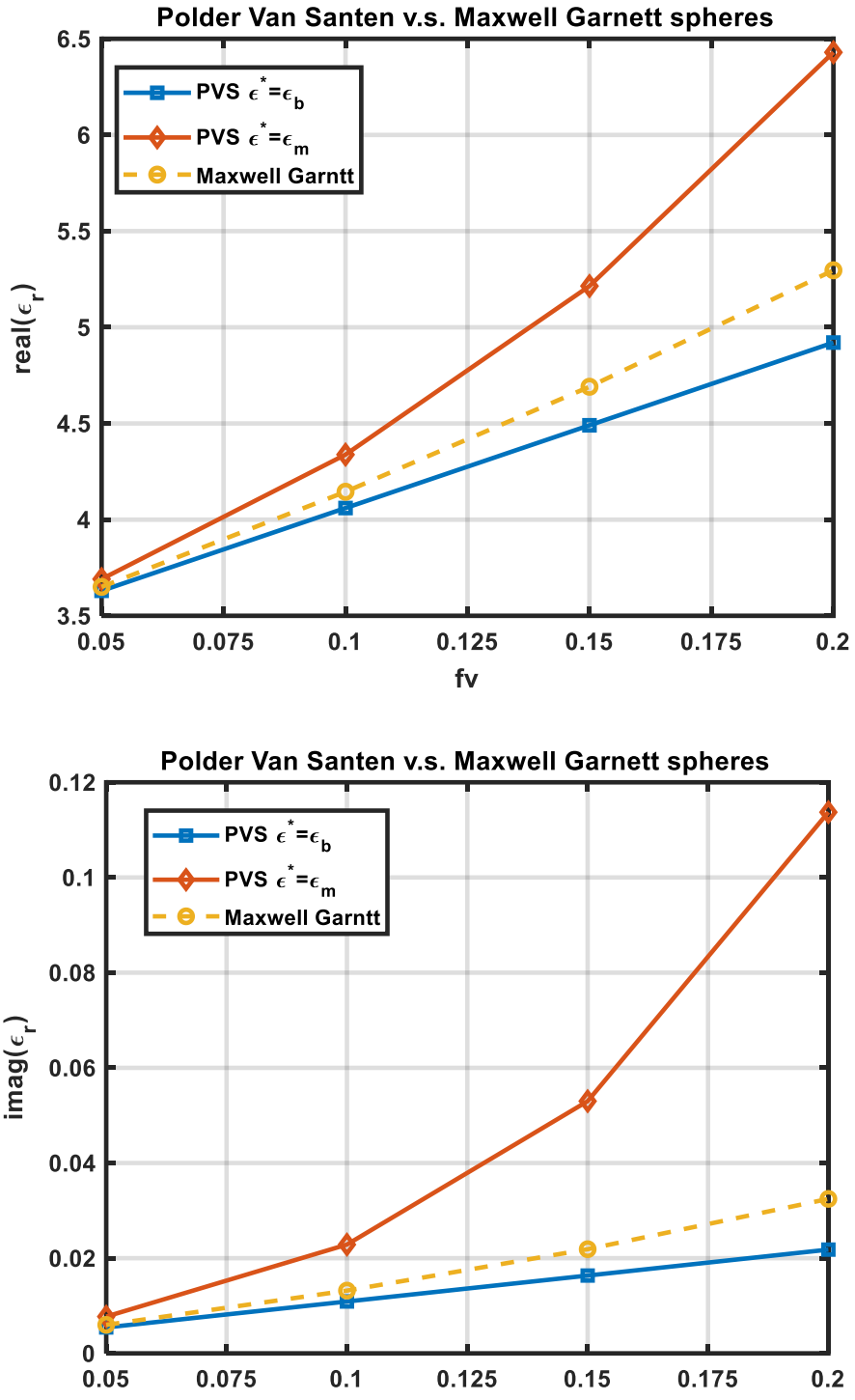

Figure 4-7 Polder Van Santen and Maxwell Garnett method for spherical inclusions. The Polder Van Santen formula has two curves; one is using $\epsilon^* = \epsilon_b$, which is more valid when f_v is small, and the other one is using $\epsilon^* = \epsilon_m$, which is more valid for large f_v. When $\epsilon^* = \epsilon_b$, the results are more close to Maxwell Garnett. For the other case, the predicted values are higher than the Maxwell Garnett formula results.

4.4 Numerical method for wave simulation

To solve the scattered field, we choose the three methods that are usually used. The three numerical methods are (1) the FEM solver in commercial software, the Ansys High-Frequency Structure Simulator (HFSS), (2) the Finite-Difference Frequency-Domain method, and (3) Volume integral equation with Discrete Dipole approximations. This section provides a brief review of the methods.

4.4.1 Finite Element Method

HFSS is a widely used commercial software in solving radiation and scattering problems. The functional of the fields is created based on the vector local basis functions. One of the major advantages of HFSS is that the software provides an adaptive mesh solution. The meshing of the problem geometry is refined each time until the convergence criterion of the two consecutive runs is met. In this paper, using a scattering boundary for the problem is sufficient. The scattered fields in all directions and the total absorption of the target are calculated and exported to compute Q_{scat} and Q_{abs} according to the equations (4-3) and (4-4).

4.4.2 Finite Difference Frequency Domain(FDFD)

The FDFD method seems to be the simplest numerical method in the frequency domain. It is similar to the Finite-Difference Time-Domain (FDTD) method, except it solves problems in the frequency domain. Compared to FEM, FDFD is naturally compatible with matrix-form geometry, and only a small effort is needed to incorporate such geometry. In addition, although it is convenient to use FDFD, a close result with FEM is expected under proper discretization size.

The wave equation is

$$\nabla^2 E + k^2 E = 0$$

After some derivations, the wave equation can be formatted into a matrix equation:

$$A_e x_e = b$$

$$A_e = D_e \mu - \epsilon$$

$$x_e = [e_x, e_y, e_z]$$

Where D_e is the spatial derivative matrix normalized by the wave number, x_e is the electric field vector to be solved, b is the source vector, μ is the permeability matrix, and ϵ is the permittivity matrix. Details can be found in [100]

To find the far-field value, the Stratton-Chu formula (Huygens' principle) is employed:

$$E_s^{far} = \frac{jk}{4\pi} \hat{r} \times \int [\hat{n} \times E - \eta \hat{r} \times (\hat{n} \times H)] \exp(jk\vec{r}) dS$$

Where $\hat{n}$ is the unit normal vector on the radiation boundary,$\hat{r}$ is the unit vector of propagation direction.

4.4.3 Volume integral equation method with Discrete Dipole approximation (DDA)

The DDA method is a technique for calculating scattering and absorption by targets of arbitrary geometry[86]. It has been used extensively in the study of bi-continuous media[85,103]. The underlying approximation for DDA is an array of polarizable points that are able to approximate a continuum target.

However, since the dimension of a discrete point has a minimum value, DDA cannot handle target boundaries. Although this problem can be relieved by decreasing discretization size, for large permittivity, DDA does not always converge. In the next section, we will present a divergent test case.

Different from FEM and FDFD, where different regions are assigned with different permittivity values, the volume integral equation method treats the permittivity in the region with complex structure as a function of positions:

$$\epsilon_p(\vec{r}) = \begin{cases} \epsilon_p, if\ in\ scatterer \\ \epsilon, if\ not\ in\ scatterer \end{cases}$$

The total field is expressed as:

$$\vec{E}(\vec{r}) = \vec{E}^{inc}(\vec{r}) + \frac{k^2}{\epsilon}\int d\vec{r}'\,\overleftrightarrow{G}(\vec{r},\vec{r}')[\epsilon_p(\vec{r}') - \epsilon]\vec{E}(\vec{r}')$$

We discretize the volume into small volumes with ΔV. The equation is changed into:

$$\bar{E}(\bar{r}_i) = \bar{E}^{\text{inc}}(\bar{r}_i) + k^2(\varepsilon_r(\bar{r}_i) - 1)s\bar{E}(\bar{r}_i) + \frac{k^2}{\varepsilon}\sum_{j\neq i}\overleftrightarrow{G}(\bar{r}_i,\bar{r}_j)\left[\varepsilon\left(\varepsilon_r(\bar{r}_j) - 1\right)\right]\bar{E}(\bar{r}_j)\Delta V$$

Where we have:

$$s = -\frac{1}{3k^2} + \frac{1}{k^2}\frac{1}{4\pi}\left[\left(\frac{4\pi}{3}\right)^{1/3}k^2d^2 + \frac{i2k^3d^3}{3}\right]$$

With the relation of:

$$\vec{p}_i = [\epsilon_p(\vec{r}_i) - \epsilon]\vec{E}(\vec{r}_i)$$

And the free space polarizability α_i:

$$\alpha_i = \frac{\Delta V\varepsilon\left(\varepsilon_r\left(\bar{r}_i\right) - 1\right)}{1 - \left(\varepsilon_r\left(\bar{r}_i\right) - 1\right)k^2s}$$

Therefore, the integral equation can be considered as:

$$\bar{p}_i = \alpha_i\left[\bar{E}^{\text{inc}}(\bar{r}_i) + \frac{k^2}{\varepsilon}\sum_{j\neq i}\overleftrightarrow{G}(\bar{r}_i,\bar{r}_j)\cdot\bar{p}_j\right]$$

The above equation is set for all of the small volumes with permittivity ϵ_p. Thus, a matrix equation is obtained for the dipole moments.

4.5 Validation of Numerical approaches

In this section, we first evaluate the three numerical approaches by comparing the scattering fields from the three methods to the analytical Mie scattering results. The diameter of the sphere is 10cm with a permittivity of 3.2, the permittivity of pure ice, and 85+10i, the permittivity of liquid water at 1.4 GHz. The background is set as air. We then use the full wave approach to calculate the permittivity of randomly positioned spheres. The results are compared to the predictions from Maxwell-Garnett and Polder Van Santen.

4.5.1 Comparison of Numerical methods

Figure 4-8 provides a comparison of different numerical methods with Mie scattering. For a small ϵ_p (e.g., 3.2) , all three methods perform well. The solutions all agree with the analytical calculations.

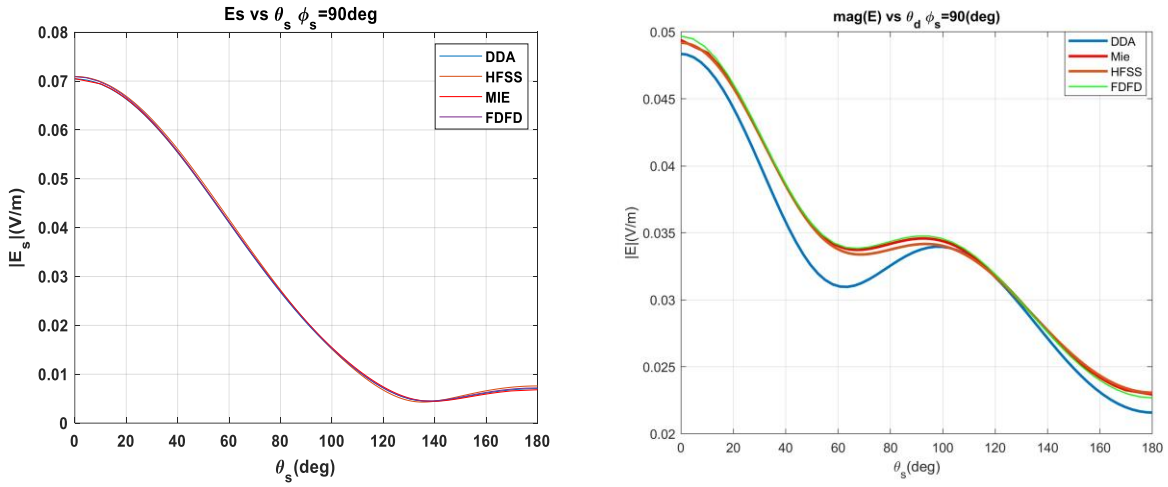

Figure 4-8 Scattered fields of a dielectric sphere from numerical approach and Mie theory. It is shown that all three methods work well when ϵ_p is small. However, the results of DDA becomes questionable for ϵ_p as large as 85+10i

However, when ϵ_p is large(85+10i), DDA cannot match analytical solution uses even with a much smaller democratization of 0.1mm, which is only 1/20λ of the wavelength in the water sphere. As a result of this, the scattered field calculated by DDA would be questionable for the study of

effective permittivity. In comparison with HFSS and FDFD, the two solvers have comparable accuracy in solving the scattered fields.

4.5.2 Validation of full wave approach for effective permittivity

Before the full wave approach can be applied to evaluate the effective permittivity of the complex structure of aquifer and wet snow, the approach needs to be validated by comparing it with the results of classical mixing formulas. We generate realizations of randomly positioned spheres using the Metropolis technique, as described in section III. Volumetric fractions of 10%, 15%, and 20% for water mixed with ice is used. For this part, we use HFSS to solve for the scattered field and absorbed energy. Spheres in the simulations are around 0.6mm, which is much smaller than the wavelength, such that the quasi-static approximation used in the Maxwell-Garnett equation can hold. An example of an HFSS simulation set-up is presented in the figure below:

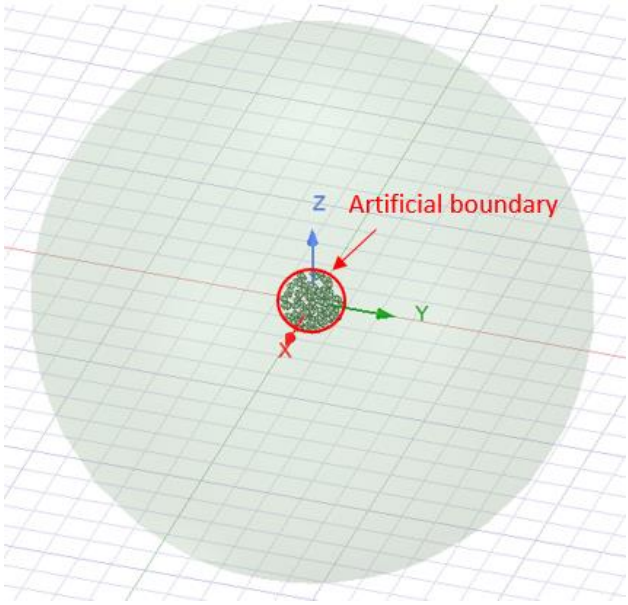

Figure 4-9 HFSS setup for the validation of Maxwell Garnett equation. The water spheres are placed in an artificial boundary with D=0.9cm. The outer sphere is the radiation boundary for the FEM simulation. The background is set as ice.

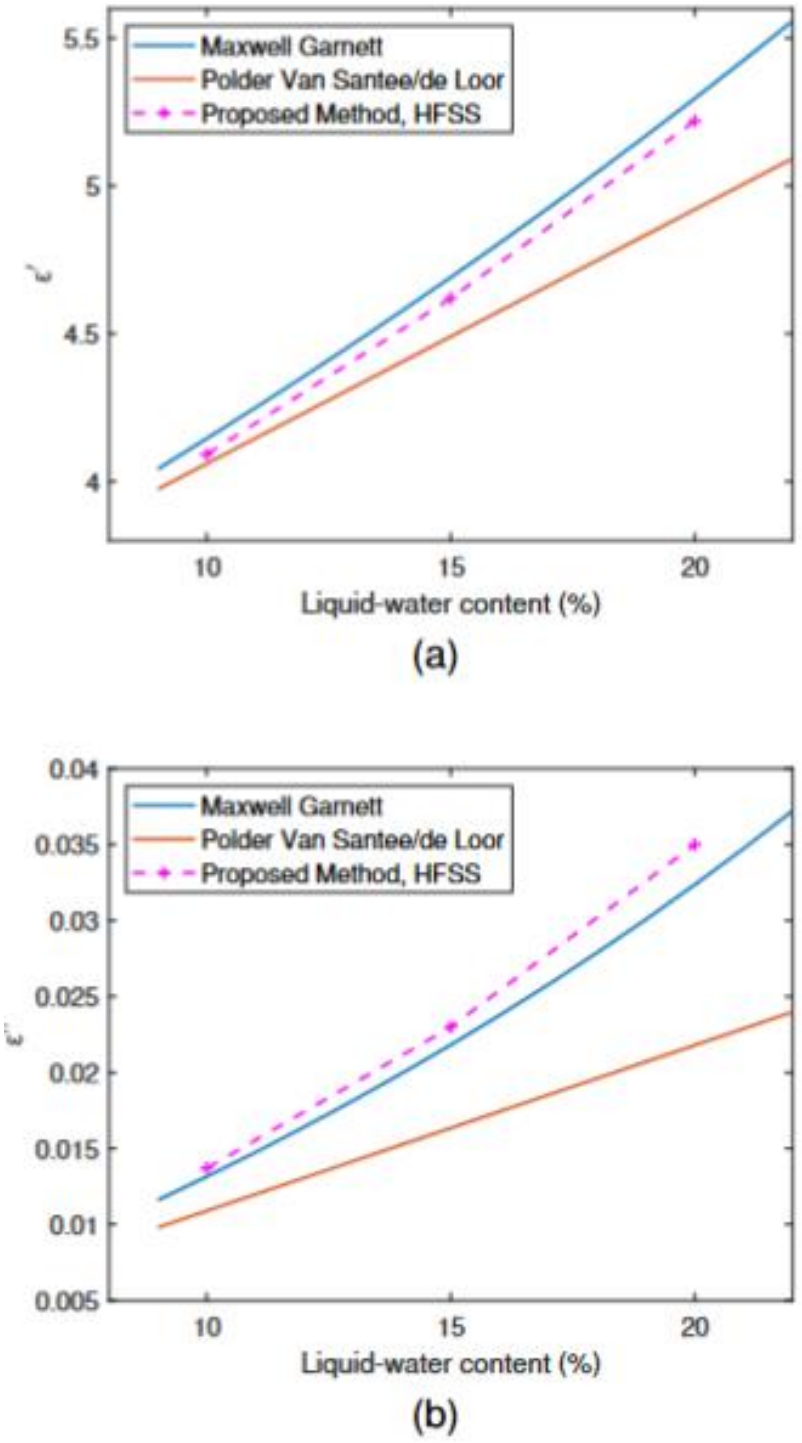

Figure 4-10 Effective permittivity of water-ice mixture with water particles as spheres. The effective permittivity from full wave simulations agrees well with the Maxwell-Garnett solutions but is different from the results of Polder Van Santen predictions, especially in the imaginary part.

Full wave simulation results for the real and imaginary parts are plotted in Figure 4-10, together with the predictions of Maxwell-Garnett and Polder Van Santen. Since the volume fraction $f < 0.2$, ϵ^* in the Polder Van Santen formula is set as ϵ_b.The real and imaginary parts are plotted in Figure 4-10 a and b, respectively. As is shown in the figure, full-wave simulation results show a good agreement with the Maxwell-Garnett formula for both the real and imaginary parts. On the other hand, the Polder-van Santen formula underestimates the permittivity for both the real and imaginary parts.

As the results from full wave simulations are in good agreement with the Maxwell-Garnett formula, the correctness of the approach is validated. We can thus perform the simulation of aquifer permittivity using this approach.

4.6 Full wave simulation of firn aquifer permittivity using bi-continuous media

In this section, we provide the permittivity simulation results using the full wave approach. The aquifer is simulated with bi-continuous media. The generation parameters are set as follows:

$$b = 5$$

$$\langle \zeta \rangle = 11000$$

This setup for the random media provides an effective mean diameter of $d = 1mm$ of the pores between ice, which is filled with water for the firn aquifer. In generating the random media, we use a discretization of 0.5mm to characterize the random media.

Due to the limitations of the CAD kernel, an artificial boundary of D=1 cm is the maximum sample that we can generate for the bi-continuous media geometry that is used for HFSS simulations. On the other hand, because of the advantages of the grid system, FDFD can easily deal with larger problems. Owing to the limitation of computation resources, only 3 cases have HFSS results.

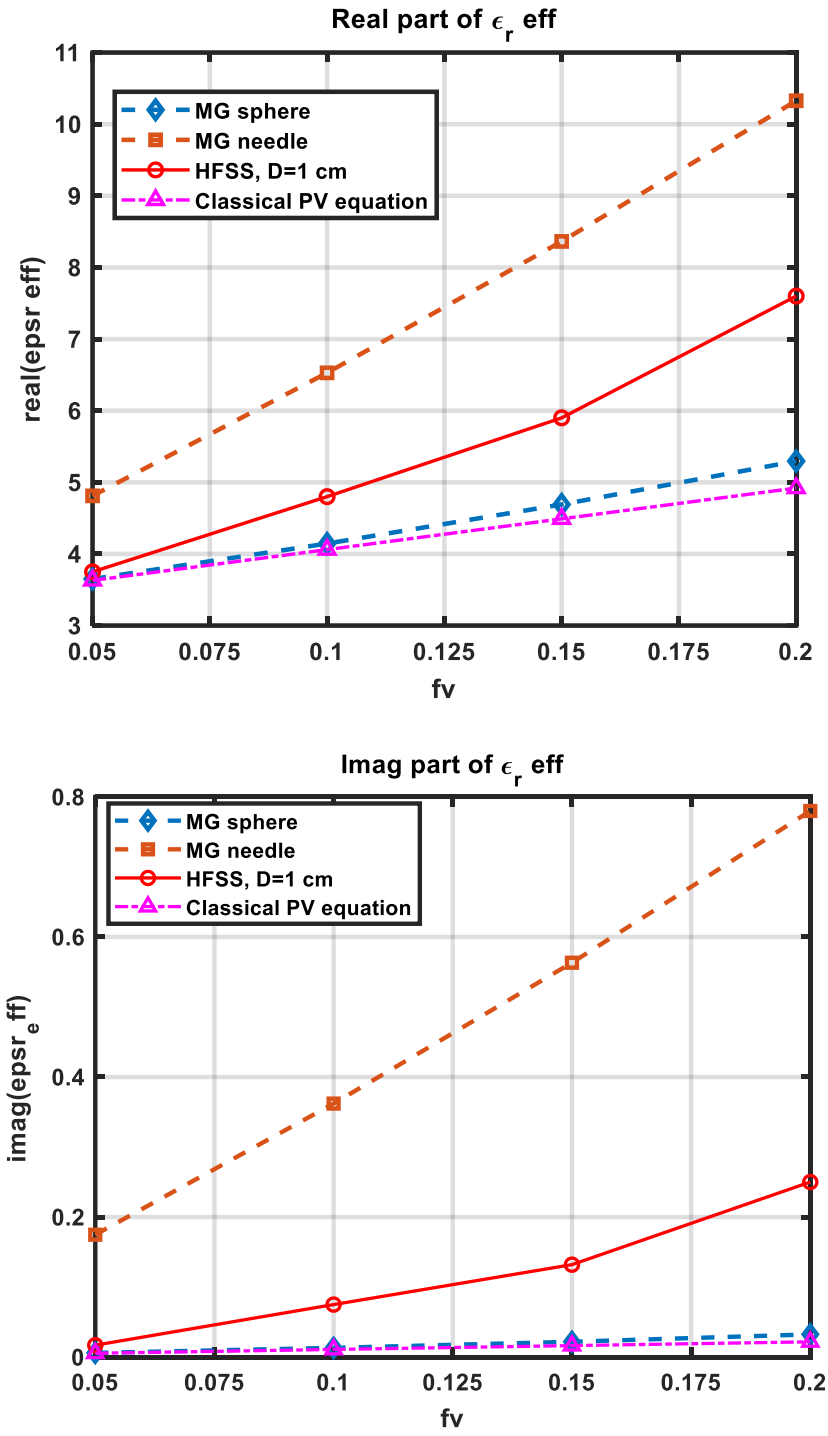

Figure 4-11 Effective permittivity from Full wave method using bi-continuous media simulated aquifer structure. The permittivity from

Figure 4-11 plots the full wave approach obtained permittivity for both the real and imaginary parts of HFSS and FDFD, together with the results of classical mixing formulas. Spheres and needles are used for the permittivity of the water-ice mixture. It can be observed that the simulation results from HFSS and FDFD compare well with each other both in the real and imaginary parts. This provides a cross-check of the two numerical methods and thus validates the correctness of the two numerical approaches. Between the two different approaches, there is only a 5-10% difference for the loss factor, while the real part has almost no difference between the two methods.

The results are plotted together with the Maxwell-Garnett formula with spheres, needles, and discs as inclusions. Obviously, inclusion shape is a major factor that affects the permittivity of the mixture. There can be three times differences in the permittivity of spherical inclusions and disc inclusions. This kind of difference will cause a major problem in the estimation of aquifer permittivity retrieval. Results show that the full wave approach has obtained a result that is very different from the classical mixing formulas with definite inclusion shapes. The predicted permittivity values are between the predictions of disc and spheres.

Figure 4-12 plots the results of permittivity with different artificial boundary sizes with D=1cm and D=2cm. Notice that the size of the artificial boundary should not affect the results of the permittivity as it is the inherent property of a material. As the volume is increased by eight times (D=1 cm to D=2 cm), the results remain unchanged for all the volume fractions. This is physically reasonable since the effective permittivity is the property of the material itself. It should be independent of the sample size that is taken out.

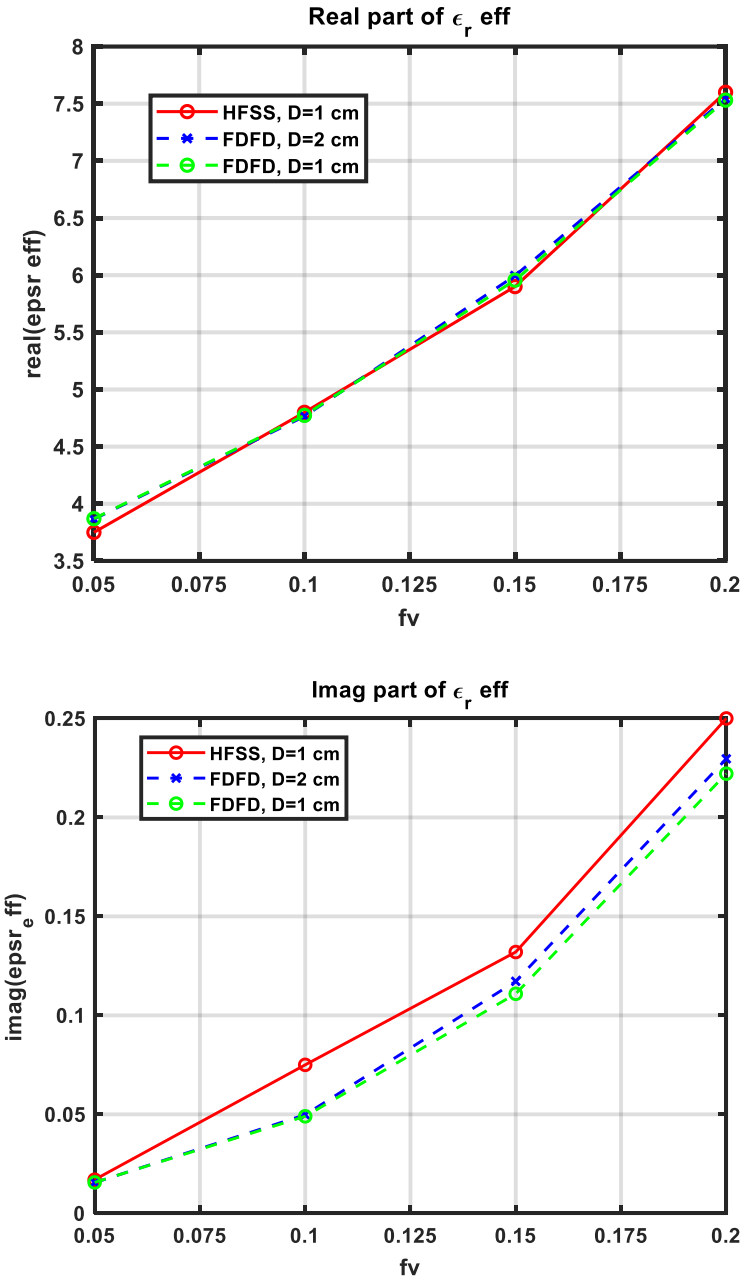

Figure 4-12 Full-wave simulation approach using HFSS FEM and FDFD. The HFSS results are only for a 1cm artificial boundary, while FDFD uses both 1cm and 2cm. The results indicate that the two numerical approaches have very good agreement in predicting the real part of

If we consider the dry firn above the aquifer has a permittivity of $\epsilon_r = 2$. The emission angle in the dry firn needs to be $27deg$ such that in the air, the emission angle is 40deg. We compare the

predicted emission across the boundary and assume a flat interface by using the 20% liquid water content permittivity from spheres and full-wave simulations.

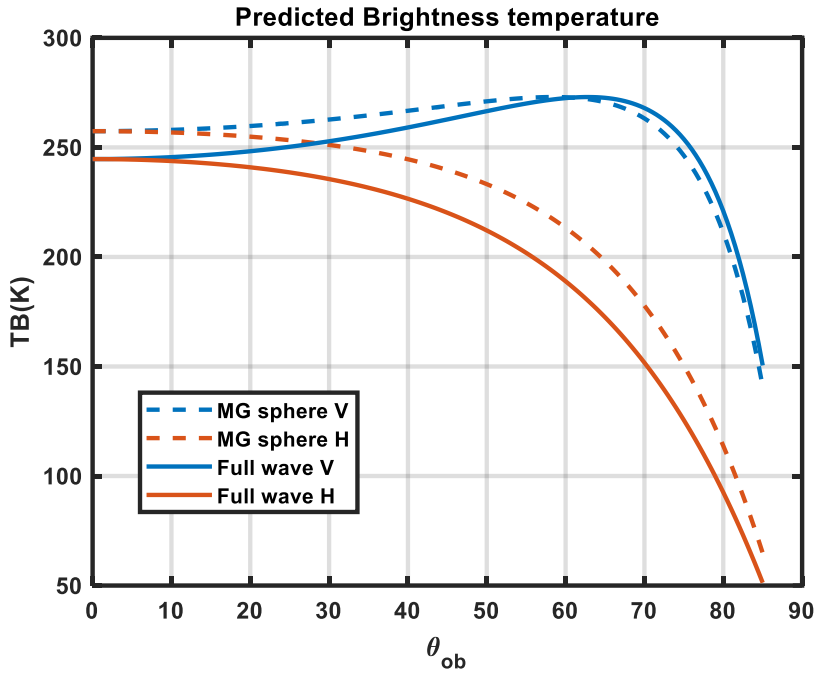

Figure 4-13 TB emitted from dry firn aquifer boundary assuming dry firn permittivity as 2.

4.7 Conclusions

A full wave approach is designed to find the equivalent permittivity of a mixture with complex inclusion structures, particularly for firn aquifer at 1.4GHz. The advantage of this method is that the mixture does not require to have a definite inclusion shape. The mixture is truncated into a sphere, and the mean normalized scattering cross-section and absorption cross-section are characterized. By fitting the same quantities of a homogeneous sphere of the same size using a changing permittivity, the effective permittivity of the mixture is obtained. The structure of the firn aquifer is characterized by bi-continuous media due to its resemblance to the real firn porous structure. Results have shown that the full-wave simulation approach can generate the same results as Maxwell Garnett formula, assuming spherical particle inclusions. The full wave approach has predicted a different permittivity from the classical mixing formulas using spheres, needles, and

discs. The proposed method allows the characterization of effective permittivity for complex natural media such as firn aquifer and wet snow. Liquid water content retrieval for the aquifer and wet snow will be benefited from the work.

Chapter 5 Radiative Transfer Modeling for the Thermal Emission of Aquifer Region

In this chapter, we discuss the radiative transfer approach that is used to model the thermal emission of the firn aquifer region. The model is targeted to model the V and H brightness temperature at 1.4GHz, which is the operating frequency of the SMAP radiometer. With the modeled permittivity and a radiative transfer model that can forward predict the emission, we can estimate the water content of the firn aquifer using the SMAP radiometer data

5.1 Radiative transfer model

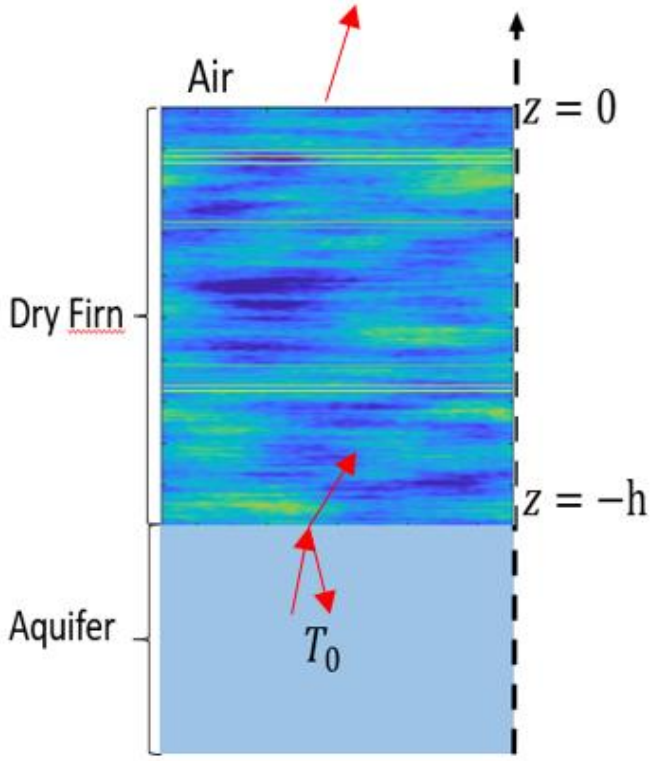

Figure 5-1 The Emission problem represents the emission from the firn aquifer region. The lower region is the aquifer, the middle region is dry firn with density variations, and the top region is air.

The emission problem is described in Figure 5-1. This figure indicates the case of later springs where the dry firn is completely frozen up. The lower region is the firn aquifer, which is a mixture of ice and water. The physical temperature of the aquifer is fixed at 273.15K, as indicated by the borehole measurements. The dry frin region has a slowly changing temperature profile and has a lot of density variations that are much more significant than the density variations in the dry zone, as indicated in Figure 5-2. The density measurement is taken in the borehole FA-13, which is close to the southeast coast of Greenland. The density is measured on a scale of around 20cm sampling. Given that the density measurements from the sampling will inevitably have a smoothing effect, the density fluctuation is still significant. Density change as high as 0.l5g/cm^3 can be observed.

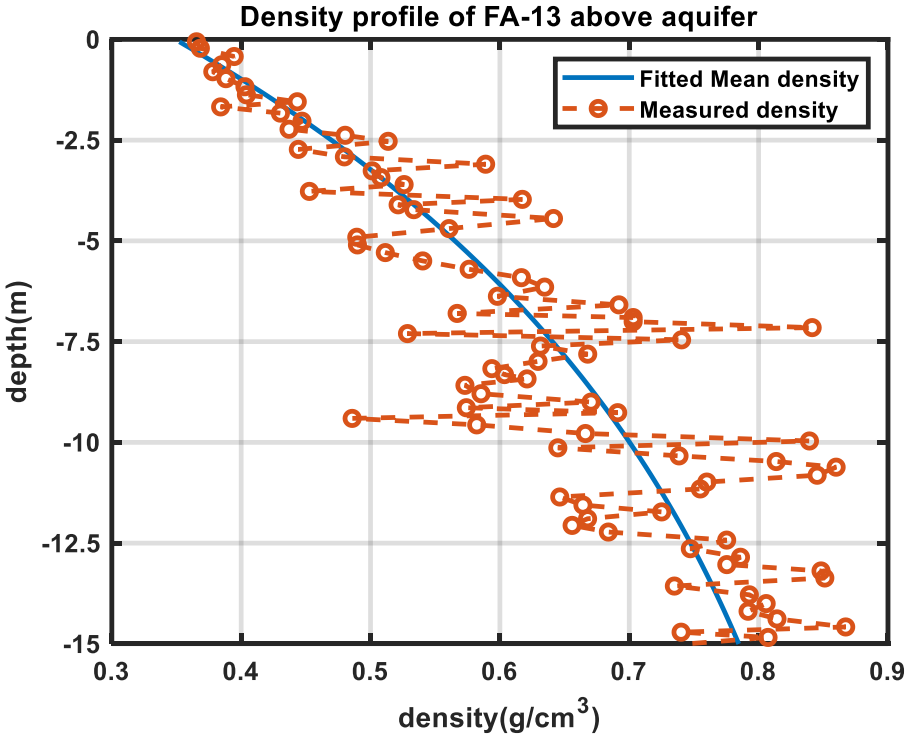

Figure 5-2 Measured density profile over FA-13 borehole, which has its water table at 12m from the surface. The mean density profile increases from about 0.35g/cm^3 to 0.8g/cm^3 from the top to the aquifer-dry firn interface. The density variation also changes along the depth.

We use a pair of radiative transfer equations with boundary conditions to characterize the thermal emission in the dry frin region, which is related to the brightness temperature that finally goes through the air-firn boundary and is received by the radiometer.

The radiative transfer equations that govern the brightness temperature in the dry firn region is provided as the following:

$$\cos\theta_i \frac{d}{dz}\vec{T}_u(\theta,z) = -\overleftrightarrow{\kappa_e}(\theta,z)\vec{T}_u(\theta,z) + \kappa_a(z)T_0(z) + \int_0^{\frac{\pi}{2}} d\theta' \sin\theta' \overleftrightarrow{P}(\theta,\theta',z)\vec{T}_u(\theta',z) + \overleftrightarrow{P}(\theta,\pi-\theta',z)\vec{T}_d(\theta',z)$$
$$-\cos\theta_i \frac{d}{dz}\vec{T}_d(\theta,z) = -\overleftrightarrow{k_e}(\theta,z)\vec{T}_d(\theta,z) + \kappa_a(z)T_0(z) + \int_0^{\frac{\pi}{2}} d\theta' \sin\theta' \left[\overleftrightarrow{P}(\pi-\theta,\theta',z)\vec{T}_u(\theta',z) + \overleftrightarrow{P}(\pi-\theta,\pi-\theta',z)\vec{T}_d(\theta',z)\right]$$

(5-1)

Where $\vec{T}_u$ is the upward-going brightness temperature, $\vec{T}_d$ is the downward-going brightness. Both V and H pol brightness temperatures are included in upward and downward going brightness temperatures. the $\overleftrightarrow{\kappa_e}(\theta,z)$ is the extinction coefficient as $\overleftrightarrow{\kappa_e}(\theta,z) = \overleftrightarrow{\kappa_s}(\theta,z) + \kappa_a(z)$ which is the sum of scattering and absorption loss. $\overleftrightarrow{P}(\theta,\theta')$ is the phase matrix that couples the brightness temperature in θ' direction into θ direction. Notice that the extinction coefficient and the phase matrix are functions of direction θ and depth z. This is due to the fact that the density properties of the dry firn are changing from the top to the interface of the aquifer, as can be observed in Figure 5-2.

The radiative transfer equation is subject to the boundary conditions at the top of the dry firn ($z = 0$) and the bottom of the dry firn($z = -d$), which is the aquifer-dry firn interface. The dry firn thickness is termed as d, and this parameter can be obtained from borehole measurements or from the Operation Ice Bridge GPR echogram.

The boundary conditions are provided as follows:

$$\vec{T}_u(\theta, z=-d) = \left(1 - \overleftrightarrow{r}_{12}(\theta)\right)T_2 + \overleftrightarrow{r}_{12}(\theta)\vec{T}_d(\theta, z=-d)$$
$$\vec{T}_d(\theta, z=0) = \overleftrightarrow{r}_{10}(\theta)\vec{T}_u(\theta, z=0)$$

Where $\overleftrightarrow{r}_{12}(\theta)$ is the matrix of reflectivity at the dry firn-aquifer interface, T_2 is the physical temperature of the aquifer. $\overleftrightarrow{r}_{10}(\theta)$ is the matrix of reflectivity of the firn-air boundary. We need to solve the radiative transfer equations according to these requirements.

Due to the inhomogeneous nature of the profile, we choose to use the iterative approach to solve for the upward and downward brightness temperatures.

We look at the upward specific intensity first. In the equation, z is changed into z', and a factor of $\exp\left(-\sec\theta \int_{z'}^{0} \overleftrightarrow{\kappa_e}(\theta, z'')dz''\right)$ is multiplied on both sides of the equation. After that, integration from $z' = -d$ to $z' = z$. With integral by parts to the left-hand side, we have the following expression:

$$\int_{-d}^{z} \cos\theta_i \frac{d}{dz'} \vec{T}_u(\theta, z') \exp\left(-\sec\theta \int_{z'}^{0} \overleftrightarrow{\kappa_e}(\theta, z'')dz''\right) =$$

$$\cos\theta_i \overrightarrow{T_u}(\theta, z) \exp\left(-\sec\theta \int_{z}^{0} \overleftrightarrow{\kappa}_e(\theta, z'')dz''\right)$$

$$-\cos\theta_i \vec{T}_u(\theta, z' = -d) \exp\left(-\sec\theta \int_{-d}^{0} \overleftrightarrow{\kappa}_e(\theta, z'')dz''\right)$$

$$-\int_{-d}^{z} dz' \cos\theta_i \overrightarrow{T_u}(\theta, z')[\sec\theta \overleftrightarrow{\kappa_e}(\theta, z')] \exp\left(-\sec\theta \int_{z'}^{0} \overleftrightarrow{\kappa_e}(\theta, z'')dz''\right)$$

The right-hand side is obtained as:

$$Right\ hand\ side = \int_{-d}^{z} -\overleftrightarrow{\kappa_e}(\theta, z)\overrightarrow{T_u}(\theta, z) \exp\left(-\sec\theta \int_{z'}^{0} \overleftrightarrow{\kappa_e}(\theta, z'')dz''\right)dz'$$

$$+\int_{-d}^{z} \kappa_a(z')T_0(z') \exp\left(-\sec\theta \int_{z'}^{0} \overleftrightarrow{\kappa_e}(\theta, z'')dz''\right)dz'$$

$$+\int_{-d}^{z} dz' \exp\left(-\sec\theta \int_{z'}^{0} \overleftrightarrow{\kappa_e}(\theta, z'')dz''\right) \int_{0}^{\frac{\pi}{2}} d\theta' \sin\theta' \left[\overleftrightarrow{P}(\theta, \theta', z)\vec{T}_u(\theta', z) + \overleftrightarrow{P}(\theta, \pi - \theta', z)\vec{T}_d(\theta', z)\right]$$

We may cancel out the third term on the left-hand side with the first term on the right-hand side. Moving the terms and dividing both sides with $cos\theta$, we can thus have the expression as follows:

$$\vec{T}_u(\theta,z)\exp\left(-\sec\theta\int_z^0 \overleftrightarrow{\kappa}_e(\theta,z'')dz''\right)=$$

$$\vec{T}_u(\theta,z'=-d)\exp\left(-\sec\theta\int_{-d}^0 \overleftrightarrow{\kappa}_e(\theta,z'')dz''\right)$$

$$+\sec\theta\int_{-d}^z \kappa_a(z')T_0(z')\exp\left(-\sec\theta\int_{z'}^0 \overleftrightarrow{\kappa}_e(\theta,z'')dz''\right)dz'$$

$$+\int_{-d}^z dz'\exp\left(-\sec\theta\int_{z'}^0 \overleftrightarrow{\kappa}_e(\theta,z'')dz''\right)\int_0^{\frac{\pi}{2}} d\theta'\sin\theta'\left[\overleftrightarrow{P}(\theta,\theta',z)\vec{T}_u(\theta',z)+\overleftrightarrow{P}(\theta,\pi-\theta',z)\vec{T}_d(\theta',z)\right]$$

We can multiply both sides of the equation with :

$$\exp\left(\sec\theta\int_z^0 \overleftrightarrow{\kappa}_e(\theta,z'')dz''\right)=\exp\left(-\sec\theta\int_0^z \overleftrightarrow{\kappa}_e(\theta,z'')dz''\right)$$

We finally have the expression of upward brightness temperature as:

$$\overrightarrow{T_u}(\theta,z)=\vec{T}_u(\theta,z'=-d)\exp\left(-\sec\theta\int_{-d}^z \overleftrightarrow{\kappa}_e(\theta,z'')dz''\right)$$

$$+\sec\theta\int_{-d}^z \kappa_a(z')T_0(z')\exp\left(-\sec\theta\int_{z'}^z \overleftrightarrow{\kappa}_e(\theta,z'')dz''\right)dz'$$

$$+\sec\theta\int_{-d}^z dz'\exp\left(-\sec\theta\int_{z'}^z \overleftrightarrow{\kappa_e}(\theta,z'')dz''\right)\int_0^{\frac{\pi}{2}} d\theta'\sin\theta'\left[\vec{P}(\theta,\theta',z')\vec{T}_u(\theta',z')+\vec{P}(\theta,\pi-\theta',z')\vec{T}_d(\theta',z')\right]$$

As indicated in the equation above, the upward-going brightness temperature is composed of three terms. The first term is the upward brightness temperature from the lower interface of the dry firn-aquifer boundary and is decayed by the dry firn. The second term is the contribution from the dry firn itself. The third term is the coupling contribution from other directions, θ', to the direction we are interested in, θ. For simplicity, the third term is expressed later as:

$$\mathrm{S}(\theta,z')=\sec\theta\int_{-d}^z dz'\exp\left(-\sec\theta\int_{z'}^z \overleftrightarrow{\kappa_e}(\theta,z'')dz''\right)\int_0^{\frac{\pi}{2}} d\theta'\sin\theta'\left[\vec{P}(\theta,\theta',z')\vec{T}_u(\theta',z')+\vec{P}(\theta,\pi-\theta',z')\vec{T}_d(\theta',z')\right]$$

For the downward going brightness temperature, the mathematical process is similar. The term $\exp\left(-\sec\theta\int_{-d}^{z'}\overleftrightarrow{\kappa_e}(\theta,z'')dz''\right)$ is multiplied to both sides of the equation, and integration is performed on z' from $z'=z$ to $z'=0$.

After some math and canceling out the same terms on both sides of the equation, an equation is obtained as follows:

$$\overrightarrow{T_d}(\theta,z)=\overrightarrow{T_d}(\theta,0)\exp\left(-\sec\theta\int_z^0\overleftrightarrow{\kappa_e}(\theta,z'')dz''\right)$$

$$+\sec\theta\int_z^0\kappa_a(z')T_0(z')\exp\left(-\sec\theta\int_z^{z'}\overleftrightarrow{\kappa_e}(\theta,z'')dz''\right)dz'$$

$$+\sec\theta\int_z^0 dz'\exp\left(-\sec\theta\int_z^{z'}\overleftrightarrow{\kappa_e}(\theta,z'')dz''\right)\int_0^{\frac{\pi}{2}}d\theta'\sin\theta'\left[\overleftrightarrow{P}(\pi-\theta,\theta')\vec{T}_u(\theta',z)+\overleftrightarrow{P}(\pi-\theta,\pi-\theta')\vec{T}_d(\theta',z)\right]$$

The downward brightness temperature also has three terms. The first term is from the upper boundary of $z=0$. The second term again is from the emission of dry firn itself. The last term is the coupling from different directions to the downward direction, $\pi-\theta$.

Also, for simplicity, we let:

$$W(\theta,z)=$$

$$\sec\theta\int_z^0 dz'\exp\left(-\sec\theta\int_z^{z'}\overleftrightarrow{\kappa_e}(\theta,z'')dz''\right)\int_0^{\frac{\pi}{2}}d\theta'\sin\theta'\left[\overleftrightarrow{P}(\pi-\theta,\theta')\vec{T}_u(\theta',z)+\overleftrightarrow{P}(\pi-\theta,\pi-\theta')\vec{T}_d(\theta',z)\right]$$

The above mathematical process has provided explicit expressions for the upward and downward brightness temperatures. However, in those equations, the boundary values of $\vec{T}_u(\theta,z'=-d)$ and $\overrightarrow{T_d}(\theta,0)$ are still unknown, which need to be solved using the boundary conditions.

For the upward and downward brightness temperature, we set $z=0$ and $z=-d$, respectively:

$$\overrightarrow{T_u}(\theta,0)=\vec{T}_u(\theta,-d)\exp\left(-\sec\theta\int_{-d}^{0}\overleftrightarrow{\kappa_e}(\theta,z'')dz''\right)$$

$$+\sec\theta\int_{-d}^{0}\kappa_a(z')T_0(z')\exp\left(-\sec\theta\int_{z'}^{0}\overleftrightarrow{\kappa_e}(\theta,z'')dz''\right)dz'+\vec{S}(\theta,0)$$

(5-2)

$$\overrightarrow{T_d}(\theta,-d)=\overrightarrow{T_d}(\theta,0)\exp\left(-\sec\theta\int_{-d}^{0}\overleftrightarrow{\kappa_e}(\theta,z'')dz''\right)$$

$$+\sec\theta\int_{-d}^{0}\kappa_a(z')T_0(z')\exp\left(-\sec\theta\int_{-d}^{z'}\overleftrightarrow{\kappa_e}(\theta,z'')dz''\right)dz'+\overrightarrow{W}(\theta,-d)$$

(5-3)

In this expression, we have the expressions $\overrightarrow{T_u}(\theta,0)$ and $\overrightarrow{T_d}(\theta,-d)$ which are not the boundary values that we are interested in. By using the boundary conditions, the following relations are obtained to cancel out the two terms:

$$\overleftrightarrow{r_{12}}(\theta)^{-1}\left\{\vec{T}_u(\theta,-d)-(1-\overleftrightarrow{r_{12}}(\theta))T_2\right\}=\vec{T}_d(\theta,-d)$$

$$\overleftrightarrow{r_{10}}(\theta)^{-1}\overrightarrow{T_d}(\theta,0)=\overrightarrow{T_u}(\theta,0)$$

The two equations ended up as follows:

$$\overleftrightarrow{r_{10}}(\theta)^{-1}\overrightarrow{T_d}(\theta,0)-\vec{T}_u(\theta,-d)\exp\left(-\sec\theta\int_{-d}^{0}\overleftrightarrow{\kappa_e}(\theta,z'')dz''\right)=$$

$$\sec\theta\int_{-d}^{0}\kappa_a(z')T_0(z')\exp\left(-\sec\theta\int_{z'}^{0}\overleftrightarrow{\kappa_e}(\theta,z'')dz''\right)dz'+\vec{S}(\theta,0)$$

$$\overleftrightarrow{r_{12}}(\theta)^{-1}\overrightarrow{T_u}(\theta,-d)-\overrightarrow{T_d}(\theta,0)\exp\left(-\sec\theta\int_{-d}^{0}\overleftrightarrow{\kappa_e}(\theta,z'')dz''\right)=$$

$$\overleftrightarrow{r_{12}}(\theta)^{-1}(1-\overleftrightarrow{r_{12}}(\theta))T_2+\sec\theta\int_{-d}^{0}\kappa_a(z')T_0(z')\exp\left(-\sec\theta\int_{-d}^{z'}\overleftrightarrow{\kappa_e}(\theta,z'')dz''\right)dz'+\overrightarrow{W}(\theta,-d)$$

(5-4)

The above two equations are now functions for $\overrightarrow{T_u}(\theta,-d)$ and $\overrightarrow{T_d}(\theta,0)$. We can thus solve for the two boundary values. After some math, we obtain the boundary value of $\overrightarrow{T_u}(\theta,-d)$:

$$\overrightarrow{T_u}(\theta,-d) = \left[I - \overleftarrow{r_{10}}(\theta)\overrightarrow{r_{12}}(\theta)\exp\left(-2\sec\theta\int_{-d}^{0}\overleftrightarrow{\kappa_e}(\theta,z'')dz''\right)\right]^{-1}$$

$$\left\{(1-\overrightarrow{r_{12}}(\theta))T_2 + \overrightarrow{r_{12}}(\theta)\sec\theta\int_{-d}^{0}\kappa_a(z')T_0(z')\exp\left(-\sec\theta\int_{-d}^{z'}\overleftrightarrow{\kappa_e}(\theta,z'')dz''\right)dz'\right.$$

$$+\overleftarrow{r_{10}}(\theta)\overrightarrow{r_{12}}(\theta)\sec\theta\exp\left(-\sec\theta\int_{-d}^{0}\overleftrightarrow{\kappa_e}(\theta,z'')dz''\right)\int_{-d}^{0}\kappa_a(z')T_0(z')\exp\left(-\sec\theta\int_{z'}^{0}\overleftrightarrow{\kappa_e}(\theta,z'')dz''\right)dz'$$

$$+\overleftarrow{r_{10}}(\theta)\overrightarrow{r_{12}}(\theta)\exp\left(-\sec\theta\int_{-d}^{0}\overleftrightarrow{\kappa_e}(\theta,z'')dz''\right)\vec{S}(\theta,0)$$

$$\left.+\overrightarrow{r_{12}}(\theta)\overrightarrow{W}(\theta,-d)\right\}$$

(5-5)

The terms in the boundary value can be interpreted as follows. The first term is the upward emission from region 2, the firn aquifer. The second term is the downward emission of the dry frin reflected up at the dry firn-aquifer interface. The third term is the double bounce of upward emission from dry firn; the brightness temperature first emits up and bounces back by the air-firn interface, then propagates back to the lower interface and bounces upward again. The fourth term is the double bounce term for the cumulative upward coupled power. Finally, the last term is the reflected term for the coupled downward propagating brightness temperature.

For the other boundary condition of $\overrightarrow{T_d}(\theta,0)$, we have the following:

$$\overrightarrow{T_d}(\theta,0) = \left[I - \overrightarrow{r_{12}}(\theta)\overrightarrow{r_{10}}(\theta)\exp\left(-2\sec\theta\int_{-d}^{0}\overleftrightarrow{\kappa_e}(\theta,z'')dz''\right)\right]^{-1}$$

$$\left\{\overrightarrow{r_{10}}(\theta)(1-\overrightarrow{r_{12}}(\theta))T_2\exp\left(-\sec\theta\int_{-d}^{0}\overleftrightarrow{\kappa_e}(\theta,z'')dz''\right)\right.$$

$$\left.+\overrightarrow{r_{10}}(\theta)\sec\theta\int_{-d}^{0}\kappa_a(z')T_0(z')\exp\left(-\sec\theta\int_{z'}^{0}\overleftrightarrow{\kappa_e}(\theta,z'')dz''\right)dz'\right.$$

$$+\sec\,\theta\overleftrightarrow{r}_{12}(\theta)\overleftrightarrow{r}_{10}(\theta)\exp\left(-\sec\,\theta\int_{-d}^{0}\overleftrightarrow{\kappa_e}(\theta,z'')dz''\right)\int_{-d}^{0}\kappa_a(z')T_0(z')\exp\left(-\sec\,\theta\int_{-d}^{z'}\overleftrightarrow{\kappa_e}(\theta,z'')dz''\right)dz'$$

$$+\overleftrightarrow{r}_{10}(\theta)\vec{S}(\theta,0)$$

$$+\overleftrightarrow{r}_{12}((\theta)\overleftrightarrow{r}_{10}(\theta)\exp\left(-\sec\,\theta\int_{-d}^{0}\overleftrightarrow{k_e}(\theta,z'')dz''\right)\overrightarrow{W}(\theta,-d)\Big\}$$

(5-6)

This boundary value also has five terms. The first term is from the emission of the aquifer and is reflected downward at the firn-air interface. The second and third terms are the reflected upward emission of dry firn and the double bounce term of the downward emission. The fourth term is the reflected upward coupled brightness temperature, and the last term is the double bounce of downward coupled brightness temperature.

Bring the boundary values into the expression of upward and downward brightness temperature, and finally, the expressions are obtained:

$$\overrightarrow{T_u}(\theta,z)=\left[I-\overleftrightarrow{r}_{10}(\theta)\overleftrightarrow{r}_{12}(\theta)\exp\left(-2\sec\,\theta\int_{-d}^{0}\overleftrightarrow{\kappa_e}(\theta,z'')dz''\right)\right]^{-1}\exp\left(-\sec\,\theta\int_{-d}^{z}\overleftrightarrow{\kappa_e}(\theta,z'')dz''\right)(1-\overleftrightarrow{r}_{12}(\theta))T_2$$

$$+\sec\,\theta\int_{-d}^{z}\kappa_a(z')T_0(z')\exp\left(-\sec\,\theta\int_{z'}^{z}\overleftrightarrow{\kappa_e}(\theta,z'')dz''\right)dz'$$

$$+\left[I-\overleftrightarrow{r}_{10}(\theta)\overleftrightarrow{r}_{12}(\theta)\exp\left(-2\sec\,\theta\int_{-d}^{0}\overleftrightarrow{\kappa_e}(\theta,z'')dz''\right)\right]^{-1}\exp\left(-\sec\,\theta\int_{-d}^{z}\overleftrightarrow{\kappa_e}(\theta,z'')dz''\right)\overleftrightarrow{r}_{12}(\theta)\sec\,\theta$$

$$\int_{-d}^{0}\kappa_a(z')T_0(z')\exp\left(-\sec\,\theta\int_{-d}^{z'}\overleftrightarrow{\kappa_e}(\theta,z'')dz''\right)dz'$$

$$+\left[I-\overleftrightarrow{r}_{10}(\theta)\overleftrightarrow{r}_{12}(\theta)\exp\left(-2\sec\,\theta\int_{-d}^{0}\overleftrightarrow{\kappa_e}(\theta,z'')dz''\right)\right]^{-1}\exp\left(-\sec\,\theta\int_{-d}^{z}\overleftrightarrow{\kappa_e}(\theta,z'')dz''\right)\overleftrightarrow{r}_{10}(\theta)\overleftrightarrow{r}_{12}(\theta)\sec\,\theta$$

$$\exp\left(-\sec\,\theta\int_{-d}^{0}\overleftrightarrow{\kappa_e}(\theta,z'')dz''\right)\int_{-d}^{0}\kappa_a(z')T_0(z')\exp\left(-\sec\,\theta\int_{z'}^{0}\overleftrightarrow{\kappa_e}(\theta,z'')dz''\right)dz'$$

$$+\vec{S}(\theta,z)$$

$$+\left[I-\overleftrightarrow{r}_{10}((\theta)\overleftrightarrow{r}_{12}(\theta)\exp\left(-2\sec\,\theta\int_{-d}^{0}\overleftrightarrow{\kappa_e}(\theta,z'')dz''\right)\right]^{-1}\overleftrightarrow{r}_{12}(\theta)\overrightarrow{W}(\theta,-d)\exp\left(-\sec\,\theta\int_{-d}^{z}\overleftrightarrow{\kappa_e}(\theta,z'')dz''\right)$$

$$+\left[I-\overrightarrow{r}_{10}(\theta)\overrightarrow{r}_{12}(\theta)\exp\left(-2\sec\theta\int_{-d}^{0}\overrightarrow{\kappa_e}(\theta,z'')dz''\right)\right]^{-1}$$

$$\overrightarrow{r}_{10}(\theta)\overrightarrow{r}_{12}(\theta)\exp\left(-\sec\theta\int_{-d}^{z}\overrightarrow{\kappa_e}(\theta,z'')dz''\right)\exp\left(-\sec\theta\int_{-d}^{0}\overrightarrow{\kappa_e}(\theta,z'')dz''\right)\vec{S}(\theta,0)$$

(5-7)

This equation can be classified into two parts: the first five terms are the direct emission from the dry firn and the firn aquifer. The rest of the terms include either the components of $\vec{S}(\theta,z)$ and $\overrightarrow{W}(\theta,z)$ are the contributions from the coupling of brightness temperatures from other directions to θ.

For the downward brightness temperature, we have the expression as:

$$\overrightarrow{T_d}(\theta,z)$$

$$=\left[I-\overrightarrow{r}_{12}(\theta)\overrightarrow{r}_{10}(\theta)\exp\left(-2\sec\theta\int_{-d}^{0}\overrightarrow{\kappa_e}(\theta,z'')dz''\right)\right]^{-1}\exp\left(-\sec\theta\int_{z}^{0}\overrightarrow{\kappa_e}(\theta,z'')dz''\right)\overrightarrow{r}_{10}(\theta)$$

$$(1-\overrightarrow{r}_{12}(\theta))T_2\exp\left(-\sec\theta\int_{-d}^{0}\overrightarrow{\kappa_e}(\theta,z'')dz''\right)$$

$$+\sec\theta\int_{z}^{0}\kappa_a(z')T_0(z')\exp\left(-\sec\theta\int_{z}^{z'}\overrightarrow{\kappa_e}(\theta,z'')dz''\right)dz'$$

$$+\left[I-\overrightarrow{r}_{12}(\theta)\overrightarrow{r}_{10}(\theta)\exp\left(-2\sec\theta\int_{-d}^{0}\overrightarrow{\kappa_e}(\theta,z'')dz''\right)\right]^{-1}\exp\left(-\sec\theta\int_{z}^{0}\overrightarrow{\kappa_e}(\theta,z'')dz''\right)\overrightarrow{r}_{10}(\theta)$$

$$\sec\theta\int_{-d}^{0}\kappa_a(z')T_0(z')\exp\left(-\sec\theta\int_{z'}^{0}\overrightarrow{\kappa_e}(\theta,z'')dz''\right)dz'$$

$$+\left[I-\overrightarrow{r}_{12}(\theta)\overrightarrow{r}_{10}(\theta)\exp\left(-2\sec\theta\int_{-d}^{0}\overrightarrow{\kappa_e}(\theta,z'')dz''\right)\right]^{-1}\exp\left(-\sec\theta\int_{z}^{0}\overrightarrow{\kappa_e}(\theta,z'')dz''\right)\overrightarrow{r}_{12}(\theta)$$

$$\overrightarrow{r}_{10}(\theta)\exp\left(-\sec\theta\int_{-d}^{0}\overrightarrow{\kappa_e}(\theta,z'')dz''\right)\sec\theta\int_{-d}^{0}\kappa_a(z')T_0(z')\exp\left(-\sec\theta\int_{-d}^{z'}\overrightarrow{\kappa_e}(\theta,z'')dz''\right)dz'$$

$$+\overrightarrow{W}(\theta,z)$$

$$+\left[I-\overleftrightarrow{r}_{12}(\theta)\overleftrightarrow{r}_{10}(\theta)\exp\left(-2\sec\theta\int_{-d}^{0}\overleftrightarrow{\kappa_e}(\theta,z'')dz''\right)\right]^{-1}\exp\left(-\sec\theta\int_{z}^{0}\overleftrightarrow{\kappa_e}(\theta,z'')dz''\right)\overleftrightarrow{r}_{10}(\theta)\vec{S}(\theta,0)$$

$$+\left[I-\overleftrightarrow{r}_{12}(\theta)\overleftrightarrow{r}_{10}(\theta)\exp\left(-2\sec\theta\int_{-d}^{0}\overleftrightarrow{\kappa_e}(\theta,z'')dz''\right)\right]^{-1}\exp\left(-\sec\theta\int_{z}^{0}\overleftrightarrow{\kappa_e}(\theta,z'')dz''\right)\overleftrightarrow{r}_{12}(\theta)$$

$$\overleftrightarrow{r}_{10}(\theta)\exp\left(-\sec\theta\int_{-d}^{0}\overleftrightarrow{\kappa_e}(\theta,z'')dz''\right)\vec{W}(\theta,-d)$$

(5-8)

The downward brightness temperature terms can also be classified into two kinds: the direct emission and the coupling terms.

Notice that both for the upward and downward expressions, we have the terms that are due to direct emission and terms that are due to the coupling. To solve for the brightness temperature, we iterative the solutions.

Let 0^{th} order solution be:

$$\overrightarrow{T_u}^{0}(\theta,z)=\left[I-\overleftrightarrow{r}_{10}(\theta)\overleftrightarrow{r}_{12}(\theta)\exp\left(-2\sec\theta\int_{-d}^{0}\overleftrightarrow{\kappa_e}(\theta,z'')dz''\right)\right]^{-1}\exp\left(-\sec\theta\int_{-d}^{z}\overleftrightarrow{\kappa_e}(\theta,z'')dz''\right)(1-\overleftrightarrow{r}_{12}(\theta))T_2$$

$$+\sec\theta\int_{-d}^{z}\kappa_a(z')T_0(z')\exp\left(-\sec\theta\int_{z'}^{z}\overleftrightarrow{\kappa_e}(\theta,z'')dz''\right)dz'$$

$$+\left[I-\overleftrightarrow{r}_{10}(\theta)\overleftrightarrow{r}_{12}(\theta)\exp\left(-2\sec\theta\int_{-d}^{0}\overleftrightarrow{\kappa_e}(\theta,z'')dz''\right)\right]^{-1}\exp\left(-\sec\theta\int_{-d}^{z}\overleftrightarrow{\kappa_e}(\theta,z'')dz''\right)\overleftrightarrow{r}_{12}(\theta)\sec\theta$$

$$\int_{-d}^{0}\kappa_a(z')T_0(z')\exp\left(-\sec\theta\int_{-d}^{z'}\overleftrightarrow{\kappa_e}(\theta,z'')dz''\right)dz'$$

$$+\left[I-\overleftrightarrow{r}_{10}(\theta)\overleftrightarrow{r}_{12}(\theta)\exp\left(-2\sec\theta\int_{-d}^{0}\overleftrightarrow{\kappa_e}(\theta,z'')dz''\right)\right]^{-1}\exp\left(-\sec\theta\int_{-d}^{z}\overleftrightarrow{\kappa_e}(\theta,z'')dz''\right)\overleftrightarrow{r}_{10}(\theta)\overleftrightarrow{r}_{12}(\theta)\sec\theta$$

$$\exp\left(-\sec\theta\int_{-d}^{0}\overleftrightarrow{\kappa_e}(\theta,z'')dz''\right)\int_{-d}^{0}\kappa_a(z')T_0(z')\exp\left(-\sec\theta\int_{z'}^{0}\overleftrightarrow{\kappa_e}(\theta,z'')dz''\right)dz'$$

(5-9)

for upward and

$$\overrightarrow{T_d}^0(\theta,z)$$

$$= \left[I - \overleftrightarrow{r}_{12}(\theta)\overleftrightarrow{r}_{10}(\theta)\exp\left(-2\sec\,\theta\int_{-d}^{0}\overleftrightarrow{\kappa_e}(\theta,z'')dz''\right)\right]^{-1}\exp\left(-\sec\,\theta\int_{z}^{0}\overleftrightarrow{\kappa_e}(\theta,z'')dz''\right)\overleftrightarrow{r}_{10}(\theta)$$

$$(1-\overleftrightarrow{r}_{12}(\theta))T_2\exp\left(-\sec\,\theta\int_{-d}^{0}\overleftrightarrow{\kappa_e}(\theta,z'')dz''\right)$$

$$+\sec\,\theta\int_{z}^{0}\kappa_a(z')T_0(z')\exp\left(-\sec\,\theta\int_{z}^{z'}\overleftrightarrow{\kappa_e}(\theta,z'')dz''\right)dz'$$

$$+\left[I - \overleftrightarrow{r}_{12}(\theta)\overleftrightarrow{r}_{10}(\theta)\exp\left(-2\sec\,\theta\int_{-d}^{0}\overleftrightarrow{\kappa_e}(\theta,z'')dz''\right)\right]^{-1}\exp\left(-\sec\,\theta\int_{z}^{0}\overleftrightarrow{\kappa_e}(\theta,z'')dz''\right)\overleftrightarrow{r}_{10}(\theta)$$

$$\sec\,\theta\int_{-d}^{0}\kappa_a(z')T_0(z')\exp\left(-\sec\,\theta\int_{z'}^{0}\overleftrightarrow{\kappa_e}(\theta,z'')dz''\right)dz'$$

$$+\left[I - \overleftrightarrow{r}_{12}(\theta)\overleftrightarrow{r}_{10}(\theta)\exp\left(-2\sec\,\theta\int_{-d}^{0}\overleftrightarrow{\kappa_e}(\theta,z'')dz''\right)\right]^{-1}\exp\left(-\sec\,\theta\int_{z}^{0}\overleftrightarrow{\kappa_e}(\theta,z'')dz''\right)\overleftrightarrow{r}_{12}(\theta)$$

$$\overleftrightarrow{r}_{10}(\theta)\exp\left(-\sec\,\theta\int_{-d}^{0}\overleftrightarrow{\kappa_e}(\theta,z'')dz''\right)\sec\,\theta\int_{-d}^{0}\kappa_a(z')T_0(z')\exp\left(-\sec\,\theta\int_{-d}^{z'}\overleftrightarrow{\kappa_e}(\theta,z'')dz''\right)dz'$$

(5-10)

For the downward.

To calculate the higher-order solutions, we would first need to evaluate the terms:

$$\mathrm{S^n}(\theta,z') = \sec\,\theta\int_{-d}^{z}dz'\exp\left(-\sec\,\theta\int_{z'}^{z}\overleftrightarrow{\kappa_e}(\theta,z'')dz''\right)\int_{0}^{\frac{\pi}{2}}d\theta'\sin\,\theta'\left[\vec{P}(\theta,\theta',z')\vec{T}_u^{n-1}(\theta',z')\right.$$
$$\left.+\,\vec{P}(\theta,\pi-\theta',z')\vec{T}_d^{n-1}(\theta',z')\right]$$

And

$$W^n(\theta,z) = \sec\,\theta\int_{z}^{0}dz'\exp\left(-\sec\,\theta\int_{z}^{z'}\overleftrightarrow{\kappa_e}(\theta,z'')dz''\right)\int_{0}^{\frac{\pi}{2}}d\theta'\sin\,\theta'\left[\overleftrightarrow{P}(\pi-\theta,\theta')\vec{T}_u^{n-1}(\theta',z)\right.$$
$$\left.+\,\overleftrightarrow{P}(\pi-\theta,\pi-\theta')\vec{T}_d^{n-1}(\theta',z)\right]$$

The higher-order brightness temperatures can be obtained through the following:

$$\overrightarrow{T_u}^{n+1}(\theta,z) = \vec{S}^{n+1}(\theta,z)$$

$$+\left[I-\overleftrightarrow{r}_{10}((\theta)\overleftrightarrow{r}_{12}(\theta)\exp\left(-2\sec\theta\int_{-d}^{0}\overleftrightarrow{\kappa_e}(\theta,z'')dz''\right)\right]^{-1}\overleftrightarrow{r}_{12}(\theta)\overrightarrow{W}^{n+1}(\theta,-d)\exp\left(-\sec\theta\int_{-d}^{z}\overleftrightarrow{\kappa_e}(\theta,z'')dz''\right)$$

$$+\left[I-\overleftrightarrow{r}_{10}(\theta)\overleftrightarrow{r}_{12}(\theta)\exp\left(-2\sec\theta\int_{-d}^{0}\overleftrightarrow{\kappa_e}(\theta,z'')dz''\right)\right]^{-1}$$

$$\overleftrightarrow{r}_{10}(\theta)\overleftrightarrow{r}_{12}(\theta)\exp\left(-\sec\theta\int_{-d}^{z}\overleftrightarrow{\kappa_e}(\theta,z'')dz''\right)\exp\left(-\sec\theta\int_{-d}^{0}\overleftrightarrow{\kappa_e}(\theta,z'')dz''\right)\vec{S}^{n+1}(\theta,0)$$

(5-11)

And for the downward:

$$\overrightarrow{T_d}^{n+1}(\theta,z)=\overrightarrow{W}^{n+1}(\theta,z)$$

$$+\left[I-\overleftrightarrow{r}_{12}(\theta)\overleftrightarrow{r}_{10}(\theta)\exp\left(-2\sec\theta\int_{-d}^{0}\overleftrightarrow{\kappa_e}(\theta,z'')dz''\right)\right]^{-1}\exp\left(-\sec\theta\int_{z}^{0}\overleftrightarrow{\kappa_e}(\theta,z'')dz''\right)$$

$$\overleftrightarrow{r}_{10}(\theta)\vec{S}^{n+1}(\theta,0)$$

$$+\left[I-\overleftrightarrow{r}_{12}(\theta)\overleftrightarrow{r}_{10}(\theta)\exp\left(-2\sec\theta\int_{-d}^{0}\overleftrightarrow{\kappa_e}(\theta,z'')dz''\right)\right]^{-1}\exp\left(-\sec\theta\int_{z}^{0}\overleftrightarrow{\kappa_e}(\theta,z'')dz''\right)\overleftrightarrow{r}_{12}(\theta)$$

$$\overleftrightarrow{r}_{10}(\theta)\exp\left(-\sec\theta\int_{-d}^{0}\overleftrightarrow{\kappa_e}(\theta,z'')dz''\right)\overrightarrow{W}^{n+1}(\theta,-d)$$

(5-12)

The solution of the downward and upward brightness temperatures is the sum of the multiple orders:

$$\vec{T}_u(\theta,z)=\overrightarrow{T_u}^{0}(\theta,z)+\overrightarrow{T_u}^{1}(\theta,z)+\overrightarrow{T_u}^{2}(\theta,z)+\cdots$$

$$\vec{T}_d(\theta,z)=\overrightarrow{T_d}^{0}(\theta,z)+\overrightarrow{T_d}^{1}(\theta,z)+\overrightarrow{T_d}^{2}(\theta,z)+\cdots$$

The iteration continues until the increment of the next order is smaller than 0.5K.

To obtain the brightness temperature that is measured by the radiometer with the antenna having an observation of θ_{ob}, we have:

$$\vec{T}(\theta_{ob})=(1-r_{10}(\theta))\vec{T}(\theta)$$

5.2 Single homogeneous layer case

In this section, we compare the results of the iterative approach with the eigenvalue approach for a single homogenous layer of density variations. The dry firn is set with a thickness of 10m with a physical temperature of 265K. The aquifer permittivity is set as 7.6+0.25i. The dry firn is set as a permittivity of 1.64+0.01i with density fluctuations of 0.03g/cm^3, the vertical correlation length is 2cm, and the horizontal correlation length is 50cm. The two results agree with each other.

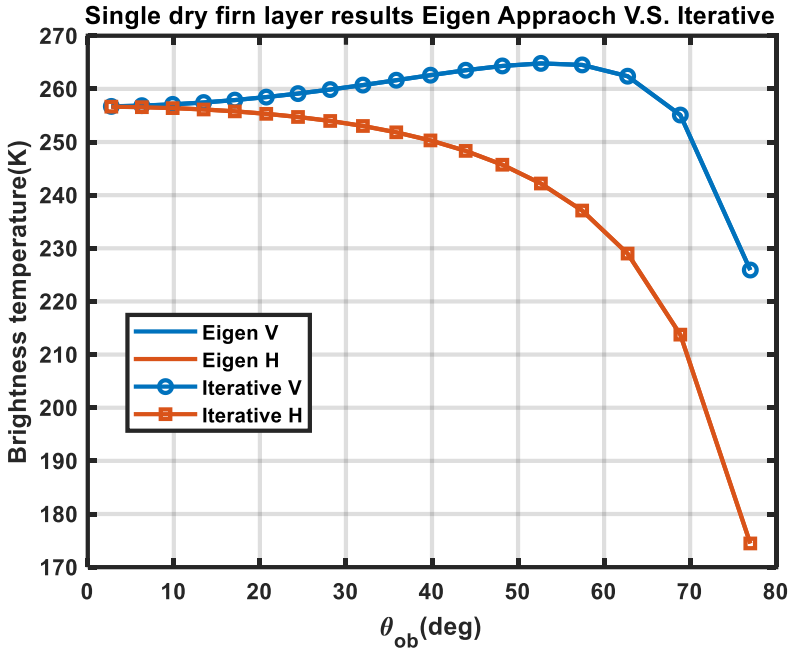

Figure 5-3 Iterative approach and Eigenvalue approach in comparison with Eigen value approach

5.3 Forward simulation for the measurement over FA-13 in April 2016

SMAP data collected in mid-April 2016 was used for comparison. The temperature profile of the dry firn we use is from interpolating the measurement results and extrapolating it to cover the range of 0-2m. The mean density profile is provided in Figure 5-2. The temperature profile is provided in Figure 5-4. The standard deviation of density variation measured in Figure 5-2 is about 0.055g/cm^3. Given that the measurement in the density would perform an averaging by itself, we

use a larger density variation of 0.085g/cm^3 for the whole layer of dry firn. The vertical and horizontal correlation

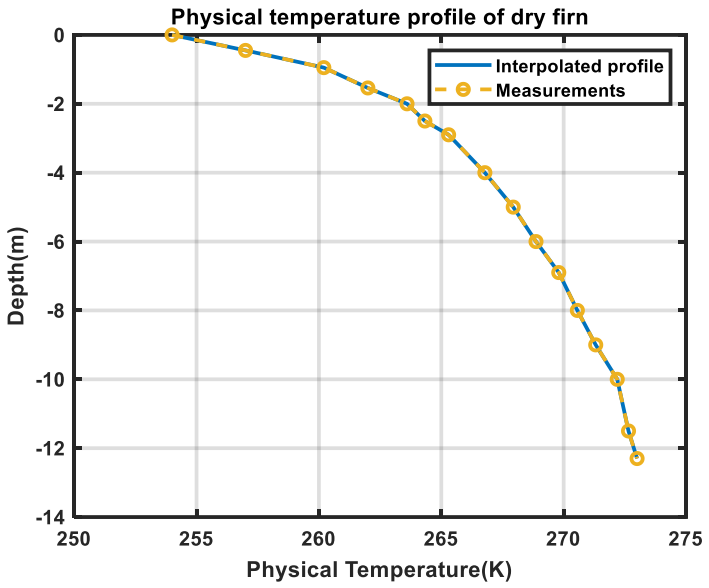

Figure 5-4 Physical temperature profile. The measured temperature is interpolated for the modeling

lengths are both set as 8cm and 15cm, respectively. For the permittivity of firn-aquifer, we use the permittivity value using the full wave approach from the last chapter. The value of $7.6 + 0.25i$ for 20% of water content is used. The forward simulation results for both V and H polarizations are presented in Figure 5-5. The forward modeling approach provides a value of 221K for V pol and 200.3K for H pol in contrast with the SMAP measurements with 220.3K and 199K. The method provides predictions that can agree with the measurements well.

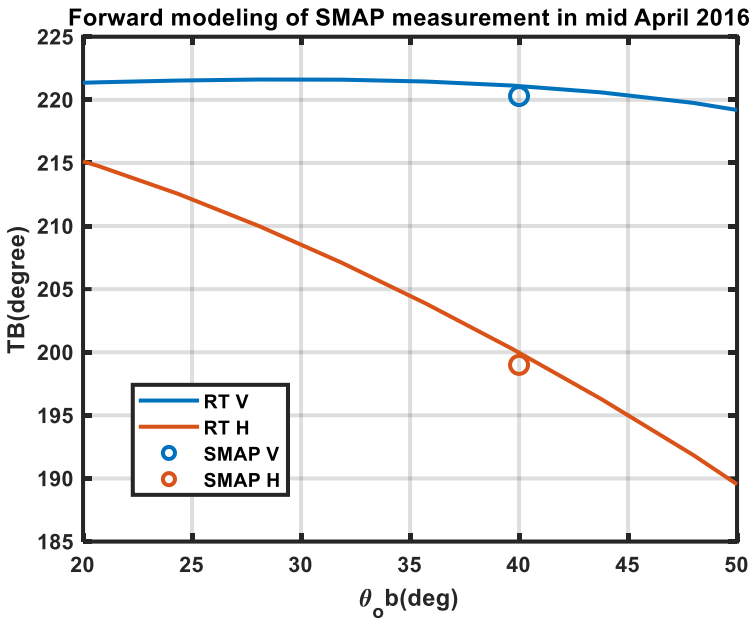

Figure 5-5 Forward simulation of Brightness temperature of FA-13 in comparison with SMAP measurements

5.4 Conclusions

In this chapter, we use the radiative transfer method to characterize the thermal emission from the firn aquifer region. The interface of air-dry firn and dry firn-aquifer is modeled as reflective. The emission problem is solved based on an iterative approach. Using the temperature profile and mean density profile provided by the borehole measurements, the proposed radiative transfer model can match well with the SMAP observations. The model developed in this chapter provides a physical basis for the retrieval of firn aquifer liquid water content using the SMAP radiometer data. The climate change and mass balance studies will be helped by the retrieval work of the liquid water content.

Chapter 6 Conclusions

The research in this thesis includes two major topics. The first topic is the modeling of near specular incoherent bistatic scattering coefficient for P-band SoOp. The second topic focuses on the remote sensing of Polar ice sheets. The RT model was built for the study of firn density. The full wave approach is used for the characterization of firn aquifer permittivity as a function of liquid water content. RT method is also implemented for the forward simulation of the brightness temperature of the firn aquifer region.

For the SoOp work, bistatic scattering coefficients simulation parameters are obtained from the Lidar measurements over Grand Mesa. 30m planar patches f_3 size is an appropriate choice for approximating land topography in Grand Mesa. Using the lidar data, we calculate the correlation function of f2 for each 30-meter by 30-meter patch for the 3.6km by 3.6 km scene. AKS results are calculated for each 30-meter by 30m patch using the 14,400 calculated correlation functions.

Simulation results show that γ_v is of the highest significance: the value can be as large as 10 dB over a wide range of azimuth angles. The value decreases as ϕ_s increases but can still be significant with a value greater than 0 dB. The choice of f3 can be adjusted based on the topography as f_3 profile is composed of multiple planar patches, which approximate the topography. The size of f3 can be larger when the topography has a smaller slope than Grand Mesa. The size of f3 can be smaller when the topography has a larger slope than Grand Mesa. The same AKS model can still be applied to such cases. The strong surface scattering shown by this simulation study loosen

the requirements of antenna design of the receiver. Thus a large swath imaging of the terrestrial snow can be achieved.

The work of dry firn over Greenland suggests a combined active and passive method for sensing long-scale fluctuations in the firn density. These fluctuations contain information on accumulation and densification within the firn. The Community Firn Model was used to generate profiles for comparison and was shown to produce simulated profiles having a reasonable agreement with in situ measurements provided that appropriate high-resolution forcing data was available. Snow Radar echo measurements were shown to provide information on refrozen layers within the firn, which could then be accounted for in analyzing 0.5-2 GHz brightness temperature datasets. The analytical partially coherent model reported was found to provide reasonable agreement with measured 0.5-2 GHz brightness temperatures by including the effects of refrozen layers and long-scale density fluctuations. Comparisons with SMOS measurements at Dome-C, in particular, demonstrate the coupling between H and V polarizations that is captured by the continuous random medium description used in the model. This work shows that the co-located active and passive microwave data can be used to infer the polar firn properties that can further be compared with CFM predictions.

A full wave approach is designed to find the equivalent permittivity of a mixture with complex inclusion structures, particularly for firn aquifer at 1.4GHz. The advantage of this method is that the mixture does not require to have a definite inclusion shape. The mixture is truncated into a sphere, and the mean normalized scattering cross-section and absorption cross-section are characterized. By fitting the same quantities of a homogeneous sphere of the same size using a changing permittivity, the effective permittivity of the mixture is obtained. The structure of the firn aquifer is characterized by bi-continuous media due to its resemblance to the real firn porous

structure. Results have shown that the full-wave simulation approach can generate the same results as Maxwell Garnett formula, assuming spherical particle inclusions. The full wave approach has predicted a different permittivity from the classical mixing formulas using spheres, needles, and discs. The proposed method allows the characterization of effective permittivity for complex natural media such as firn aquifer and wet snow. Liquid water content retrieval for the aquifer and wet snow will be benefited from the work

Finally, in the last chapter, we use the radiative transfer method to characterize the thermal emission from the firn aquifer region. The interface of air-dry firn and dry firn-aquifer is modeled as reflective. The emission problem is solved based on an iterative approach. Using the temperature profile and mean density profile provided by the borehole measurements, the proposed radiative transfer model can match well with the SMAP observatins. The model developed in this chapter provides a physical basis for the retrieval of firn aquifer liquid water content using the SMAP radiometer data. The climate change and mass balance studies will be helped by the retrieval work of the liquid water content.

Bibliography

[1]A. Etminan, A. Tabatabaeenejad, and M. Moghaddam, "Retrieving Root-Zone Soil Moisture Profile From P-Band Radar via Hybrid Global and Local Optimization," in IEEE Transactions on Geoscience and Remote Sensing, vol. 58, no. 8, pp. 5400-5408, Aug. 2020, doi: 10.1109/TGRS.2020.2965569.

[2] Le Toan et al., "The BIOMASS mission: Mapping global forest biomass to better understand the terrestrial carbon cycle," Remote Sens. Environ., vol. 115, no. 11, pp. 2850–2860, Nov. 2011.

[3] Satellite Mission page of Biomass, Available: https://directory.eoportal.org/web/eoportal/satellite-missions/b/biomass

[4] Shah, R., X. Xu, S. Yueh, C. S. Chae, K. Elder, B. Starr, and Y. Kim, "Remote sensing of snow water equivalent using P-band coherent reflection," IEEE Geoscience and Remote Sensing Letters, Vol. 14, No. 3, 309-313, 2017.

[5] K. C. Jezek et al., "500–2000-MHz Brightness Temperature Spectra of the Northwestern Greenland Ice Sheet," in IEEE Transactions on Geoscience and Remote Sensing, vol. 56, no. 3, pp. 1485-1496, March 2018, doi: 10.1109/TGRS.2017.2764381.

[6]C. Hall and R. Cordey, "Multistatic scatterometry," in Geoscience and Remote Sensing Symposium, 1988. IGARSS'88. Remote Sensing: Moving Toward the 21st Century., International, 1988, pp. 561-562.

[7] M. Martin-Neira, "A passive reflectometry and interferometry system (PARIS): Application to ocean altimetry," ESA journal, vol. 17, pp. 331-355, 1993.

[8] J. L. Garrison, S. J. Katzberg, and M. I. Hill, "Effect of sea roughness on bistatically scattered range coded signals from the Global Positioning System," Geophysical research letters, vol. 25, pp. 2257-2260, 1998.

[9] Unwin, M., P. Jales, J. Tye, C. Gommenginger, G. Foti, and J. Rosello, "Spaceborne GNSS-reflectometry on TechDemoSat-1: Early mission operations and exploitation," Sep 28, 2016 in IEEE Journal of Selected Topics in Applied Earth Observations and Remote Sensing DOI:10.1109/JSTARS.2016.2603846

[10] Ruf, C., A. Lyons, M. Unwin, J. Dickinson, R. Rose, D. Rose, and M. Vincent, "CYGNSS: Enabling the future of hurricane prediction [Remote Sensing Satellites]," IEEE Geoscience and Remote Sensing Magazine, Vol. 1, No. 2, 52-67, 2013.

[11] C. Jing, X. Niu, C. Duan, F. Lu, G. Di, and X. Yang, "Sea surface wind speed retrieval from the first Chinese GNSS-R mission: Technique and preliminary results", Remote Sens., vol. 11, no. 24, pp. 3013, Dec. 2019.

[12] Clarizia, M. P. and C. S. Ruf, "Wind speed retrieval algorithm for the cyclone global navigation satellite system (CYGNSS) mission," IEEE Transactions on Geoscience and Remote Sensing, Vol. 54, No. 8, 4419-4432, 2016.

[13] Li, W., E. Cardellach, F. Fabra, A. Rius, S. Ribo, and M. Martin-Neira, "First spaceborne phase altimetry over sea ice using TechDemoSat-1 GNSS-R signals," Geophysical Research Letters, Vol. 44, No. 16, 8369-8376, 2017.
[14] Nghiem, S. V., C. Zuffada, R. Shah, C. Chew, S. T. Lowe, A. J. Mannucci, E. Cardellach, G. R.Brakenridge, G. Geller, and A. Rosenqvist, "Wetland monitoring with global navigation satellite system reflectometry: Wetland monitoring with GNSS-R," Earth and Space Science, Vol. 4, No. 1,16-39, Hoboken, N.J., 2017.
[15] Kim, H. and V. Lakshmi, "Use of cyclone global navigation satellite system (CYGNSS) observations for estimation of soil moisture," Geophysical Research Letters, Vol. 45, No. 16, 8272-8282, 2018.
[16] Chew, C. C. and E. E. Small, "Soil moisture sensing using spaceborne GNSS reflections: Comparison of CYGNSS reflectivity to SMAP soil moisture," Geophysical Research Letters, Vol. 45, No. 9, 4049-4057, 2018.
[17] Clarizia, M. P., N. Pierdicca, F. Costantini, and N. Floury, "Analysis of CYGNSS data for soil moisture retrieval," IEEE Journal of Selected Topics in Applied Earth Observations and Remote Sensing, Vol. 12, No. 7, 2227-2235, 2019.
[18]A. Camps et al., "Sensitivity of GNSS-R Spaceborne Observations to Soil Moisture and Vegetation," in IEEE Journal of Selected Topics in Applied Earth Observations and Remote Sensing, vol. 9, no. 10, pp. 4730-4742, Oct. 2016, doi: 10.1109/JSTARS.2016.2588467.
[19]X. Chu et al., "Multimodal Deep Learning for Heterogeneous GNSS-R Data Fusion and Ocean Wind Speed Retrieval," in IEEE Journal of Selected Topics in Applied Earth Observations and Remote Sensing, vol. 13, pp. 5971-5981, 2020, doi:10.1109/JSTARS.2020.3010879.
[20] Simon Yueh, et al., "A Satellite Synthetic Aperture Radar Concept Using P-Band Signals of Opportunity," IEEE Journal of Selected Topics in Applied Earth Observations and Remote Sensing, Vol. 28, pp. 2796-2816, 18 Feb 2021. DOI: 10.1109/JSTARS.2021.3059242.
[21] J. D. Oetting and T. Jen. "The mobile user objective system." Johns Hopkins Apl Technical Digest 30, no. 2 (2011): 103-112. (http://techdigest.jhuapl.edu/TD/td3002/Oetting.pdf)
[22] B.Ren, J. Zhu, L. Tsang, and H. Xu, "Analytical Kirchhoff Solutions (AKS) and Numerical Kirchhoff Approach (NKA) for First-Principle Calculations of Coherent Waves and Incoherent Waves at P Band and L Band in Signals of Opportunity (SoOp)," Progress In Electromagnetics Research, Vol. 171, 35-73, 2021
[23]Painter, T. H. and K. J. Bormann. (2020). ASO L4 Lidar Point Cloud Digital Terrain Model 3m UTM Grid, Version 1 [Data Set]. Boulder, Colorado, USA. NASA National Snow and Ice Data Center Distributed Active Archive Center. https://doi.org/10.5067/2EHMWG4IT76O. Date Accessed 10-14-2022.
[24]Tsang, L.; Liao, T.-H.; Gao, R.; Xu, H.; Gu, W.; Zhu, J. Theory of Microwave Remote Sensing of Vegetation Effects, SoOp and Rough Soil Surface Backscattering. Remote Sens. 2022, 14, 3640. https://doi.org/10.3390/rs14153640
[25] Al-Khaldi, M. M., J. T. Johnson, A. J. O'Brien, A. Balenzano, and F. Mattia, Time-series retrieval of soil moisture using CYGNSS," IEEE Transactions on Geoscience and Remote Sensing, Vol. 57, No. 7, 4322{4331, 2019.
[26] J. D. Campbell, A. Melebari and M. Moghaddam, "Modeling the Effects of Topography on Delay-Doppler Maps," in IEEE Journal of Selected Topics in Applied Earth Observations and Remote Sensing, vol. 13, pp. 1740-1751, 2020, doi: 10.1109/JSTARS.2020.2981570.
[27] Zavorotny, V. and A. Voronovich, Scattering of GPS signals from the ocean with wind remote

sensing application," IEEE Transactions on Geoscience and Remote Sensing, Vol. 38, No. 2, 951-964, 2000.

[28] Thompson, D., T. Elfouhaily, and J. Garrison, An improved geometrical optics model for bistatic GPS scattering from the ocean surface," IEEE Transactions on Geoscience and Remote Sensing, Vol. 43, No. 12, 2810-2821, Dec. 2005.

[29] Dente, L., L. Guerriero, D. Comite, and N. Pierdicca, \Space-borne GNSS-R signal over complex topography: Modeling and validation," IEEE Journal of Selected Topics in Applied Earth Observations and Remote Sensing, Vol. 13, 1218{1233, 2020.

[30] Gu, W., H. Xu, and L. Tsang, A numerical Kirchhoff simulator for GNSS-R land applications," Progress In Electromagnetics Research, Vol. 164, 119~133, 2019.

[31] J. D. Campbell et al., "Intercomparison of Electromagnetic Scattering Models for Delay-Doppler Maps along a CYGNSS Land Track with Topography," in IEEE Transactions on Geoscience and Remote Sensing, 2022, doi: 10.1109/TGRS.2022.3210160.

[32] Frederikse, T., Landerer, F., Caron, L. et al. The causes of sea-level rise since 1900. Nature 584, 393–397 (2020). https://doi.org/10.1038/s41586-020-2591-3

[33] Oppenheimer, M. et al. in IPCC Special Report on the Ocean and Cryosphere in a Changing Climate (eds Pörtner, H.-O. et al.) Ch.4 (2019).

[34] A. Shepherd, E. R. Ivins, G. A, V. R. Barletta, M. J. Bentley, S. Bettadpur, K. H. Briggs, D. H. Bromwich, R. Forsberg, N. Galin, M. Horwath, S. Jacobs, I. Joughin, M. A. King, J. T. M. Lenaerts, J. Li, S. R. M. Ligtenberg, A. Luckman, S. B. Luthcke, M. McMillan, R. Meister, G. Milne, J. Mouginot, A. Muir, J. P. Nicolas, J. Paden, A. J. Payne, H. Pritchard, E. Rignot, H. Rott, L. S. Sørensen, T. A. Scambos, B. Scheuchl, E. J. O. Schrama, B. Smith, A. V. Sundal, J. H. van Angelen, W. J. van de Berg, M. R. van den Broeke, D. G. Vaughan, I. Velicogna, J. Wahr, P. L. Whitehouse, D. J. Wingham, D. Yi, D. Young, H. J. Zwally, A reconciled estimate of ice-sheet mass balance. Science 338, 1183–1189 (2012).

[35]Slater, T., Lawrence, I. R., Otosaka, I. N., Shepherd, A., Gourmelen, N., Jakob, L., Tepes, P., Gilbert, L., and Nienow, P.: Review article: Earth's ice imbalance, The Cryosphere, 15, 233–246, https://doi.org/10.5194/tc-15-233-2021, 2021.

[36] Dangendorf, S. et al. Persistent acceleration in global sea-level rise since the 1960s. Nat. Clim. Change 9, 705–710 (2019).

[37]Gregory, J. M. et al. Twentieth-century global-mean sea level rise: is the whole greater than the sum of the parts? J. Clim. 26, 4476–4499 (2013).

[38] Shepherd, A., Gilbert, L., Muir, A. S., Konrad, H., McMillan, M., Slater, T., ... & Engdahl, M. E. (2019). Trends in Antarctic Ice Sheet elevation and mass. Geophysical Research Letters, 46(14), 8174-8183.

[39] Bamber, J.L., R. M. Westaway, B. Marzeion, B. Wouters, The land ice contribution to sea level during the satellite era. *Environ. Res. Lett.* 13, 63008 (2018).

[40] Smith, B., Fricker, H. A., Gardner, A. S., Medley, B., Nilsson, J., Paolo, F. S., ... & Harbeck, K. (2020). Pervasive ice sheet mass loss reflects competing ocean and atmosphere processes. Science, 368(6496), 1239-1242.

[41] Shepherd, A., Gilbert, L., Muir, A. S., Konrad, H., McMillan, M., Slater, T., Briggs, K. H., Sundal, A.V., Hogg, A. E., and Engdahl, M. E. Trends in Antarctic Ice Sheet elevation and mass. Geophysical Research Letters, vol 46 Issue 14, pp. 8174-8183. https://doi.org/10.1029/2019GL082182 ,2019

[42] Ligtenberg, S. R. M., Helsen, M. M., and Van den Broeke, M. R. An improved semi-empirical model for the densification of Antarctic firn. The Cryosphere, 5, vol.5 Issue 4, pp. https://doi.org/10.5194/tc-5-809-2011 809-819. 2011

[43] Kuipers Munneke, P., Ligtenberg, S. R. M., Noël, B. P. Y., Howat, I. M., Box, J. E., Mosley-Thompson, E., McConnell, J.R., Steffen, K., Harper, J.T., Das, S.B., and Van Den Broeke, M. R. Elevation change of the Greenland Ice Sheet due to surface mass balance and firn processes, The Cryosphere, vol, 9, Issue 6, pp. 2009-2025. https://doi.org/10.5194/tc-9-2009-2015 2015

[44] Medley, B., Neumann, T. A., Zwally, H. J., Smith, B. E., and Stevens, C. M.: Simulations of firn processes over the Greenland and Antarctic ice sheets: 1980–2021, The Cryosphere, vol., 16, pp.3971–4011, https://doi.org/10.5194/tc-16-3971-2022, 2022.

[45] Stevens, M., Emmakahle, H. V., and Jboat: UWGlaciology/CommunityFirnModel: Version 1.1.6, Zenodo, https://doi.org/10.5281/ZENODO.5719748, zenodo, 2021.

[46] Montgomery, L., Koenig, L., and Alexander, P. The SUMup Dataset: Compiled measurements of surface mass balance components over ice sheets and sea ice with analysis over Greenland, Earth Syst. Sci. Data, vol.,10, pp.1959–1985. https://doi.org/10.5194/essd-10-1959-2018, 2018

[47] Li, J., and Zwally, H. J., Modeling of firn compaction for estimating ice-sheet mass change from observed ice-sheet elevation change. Annals of Glaciology, vol., 52 Issue 59, pp. 1-7. https://doi.org/10.3189/172756411799096321 2011

[48] Koenig, L. S., Steig, E. J., Winebrenner, D. P., and Shuman, C. A. A link between microwave extinction length, firn thermal diffusivity, and accumulation rate in West Antarctica. Journal of Geophysical Research: Earth Surface, vol, 112 Issue F3. https://doi.org/10.1029/2006JF000716 2007

[49] Brucker, L., Picard, G., and Fily, M. Snow grain-size profiles deduced from microwave snow emissivities in Antarctica. Journal of Glaciology, Vol 56, Issue 197, pp514-526. doi:10.3189/002214310792447806 2010

[50] Champollion, N., Picard, G., Arnaud, L., Lefebvre, E., and Fily, M.: Hoar crystal development and disappearance at Dome C, Antarctica: observation by near-infrared photography and passive microwave satellite, The Cryosphere, 7, 1247–1262, https://doi.org/10.5194/tc-7-1247-2013, 2013

[51] Medley, B., Ligtenberg, S. R. M., Joughin, I., Van den Broeke, M. R., Gogineni, S., and Nowicki, S. Antarctic firn compaction rates from repeat-track airborne radar data: I. Methods. Annals of Glaciology, vol 56 Issue 70, pp. 155-166. https://doi.org/10.3189/2015AoG70A203,2015

[52] Jezek, K. C., Gogineni, P., and Shanableh, M., Radar Measurements of Melt Zones on the Greenland Ice Sheet, Geophysical Research Letters, vol., 21 Issue 1, pp. 33-36. https://doi.org/10.1029/93GL03377, 1994

[53] Zabel, I.H.H., Jezek, K.C., Baggeroer, P.A., and Gogineni, S.P., Radar Observations of Snow Stratigraphy and Melt Processes on the Greenland Ice Sheet. Annals of Glaciology. Vol 21, p. 40-44. https://doi.org/10.3189/S0260305500015573 1995

[54] Medley, B., Joughin, I., Das, S. B., Steig, E. J., Conway, H., Gogineni, S., Criscitiello, A.S., McConnel, R., Smith, B.E., van den Broeke, M. R., Lenaerts, J. T., Bromwich, D. H., and Nicolas, J.P. Airborne ‐ radar and ice ‐ core observations of annual snow accumulation over Thwaites Glacier, West Antarctica confirm the spatiotemporal variability of global and regional atmospheric models. Geophysical Research Letters, vol. 40 Issue 14, pp. 3649-3654. https://doi.org/10.1002/grl.50706 2013

[55]Medley, B., Joughin, I., Smith, B. E., Das, S. B., Steig, E. J., Conway, H., Gogineni, S., Lewis, C., Criscitiello, A.S., McConnell, J. R., Van den Broeke, M. R., Lenaerts, J.T.M, Bromwich, D. H., Nicolas, J.P., Leuschen, C., Constraining the recent mass balance of Pine Island and Thwaites glaciers, West Antarctica, with airborne observations of snow accumulation. The Cryosphere, vol., 8, 1375-1392. https://doi.org/10.5194/tc-8-1375-2014.2014.

[56] Koenig, L. S., Ivanoff, A., Alexander, P. M., MacGregor, J. A., Fettweis, X., Panzer, B., Paden, J.D., Forster, R.R., Das, I., McConnell, J.R., Tedesco, M., Leuschen, C., Gognineni, P., Annual Greenland accumulation rates (2009–2012) from airborne snow radar. The Cryosphere, vol.10, pp 1739-1752, https://doi.org/10.5194/tc-10-1739-2016. 2016

[57] Dattler, M. E., Lenaerts, J. T., and Medley, B. Significant Spatial Variability in Radar-Derived West Antarctic Accumulation Linked to Surface Winds and Topography. Geophysical Research Letters, Vol. 46, Issue 22, pp. 13126-13134. https://doi.org/10.1029/2019GL085363,2019

[58] Brogioni, M., Macelloni, G., Montomoli, F., and Jezek, K.C., Simulating Multifrequency Ground-Based Radiometric Measurements at Dome C—Antarctica, IEEE Journal of Selected Topics in Applied Earth Observations and Remote Sensing, vol. 8, no. 9, pp. 4405-4417, doi: 10.1109/JSTARS.2015.2427512. 2015

[59] Tan S., Tsang L., Xu, H., Johnson, J.T., Jezek, K.C., Yardim, C., Durand, M., Duan, Y., "A Partially Coherent Approach for Modeling Polar Ice Sheet 0.5–2-GHz Thermal Emission," in IEEE Transactions on Geoscience and Remote Sensing, vol. 59, no. 10, pp. 8062-8072, doi: 10.1109/TGRS.2020.3039057. 2021

[60] Yardim, C., Johnson, J. T, Jezk, K.C., Andrews, M. J., Durand, M., Duan, Y., Tan, S., Tsang, L., Brogioni, M., Macelloni, G., Bringer, A., Greenland Ice Sheet Subsurface Temperature Estimation Using Ultrawideband Microwave Radiometry IEEE Transactions on Geoscience and Remote Sensing, vol. 60, pp. 1-12, , Art no. 4300312, doi: 10.1109/TGRS.2020.3043954. 2022

[61] Tsang, L., J.A. Kong, and K.H. Ding, Scattering of Electromagnetic Waves, Vol. 1: Theory and Applications, Wiley Interscience, 2000, 426 pages 2000,

[62] CReSIS. 2021. Snow radar Data, Lawrence, Kansas, USA. Digital Media. http://data.cresis.ku.edu/.

[63] Tan S., Aksoy, M., Brogioni, M., Macelloni, G., Durand, M., Jezek, K. C., Wang, T.-L, Tsang, L., Johnson, J. T., Drinkwater, M. R., and Brucker, L., Physical Models of Layered Polar Firn Brightness Temperatures From 0.5 to 2 GHz, IEEE J. Sel. Topics Appl. Earth Observ. Remote Sens., vol. 8, no. 7, pp. 3681-3691, 10.1109/JSTARS.2015.2403286, 2015.

[64] Nghiem, S. V., Hall, D. K., Mote, T. L., Tedesco, M., Albert, M. R., Keegan, K., Shuman, C. A., DiGirolamo, N. E., and Neumann, G. (2012), The extreme melt across the Greenland ice sheet in 2012, Geophys. Res. Lett., 39, L20502, doi:10.1029/2012GL053611.

[65] Koenig, L. S., Miège, C., Forster, R. R., and Brucker, L. (2014), Initial in situ measurements of perennial meltwater storage in the Greenland firn aquifer, Geophys. Res. Lett., 41, 81–85, doi:10.1002/2013GL058083

[66]] Miller, O., Solomon, D. K., Miège, C., Koenig, L., Forster, R., Schmerr, N., et al. (2020). Hydrology of a perennial firn aquifer in southeast Greenland: An overview driven by field data. *Water Resources Research*, 56, e2019WR026348. https://doi.org/10.1029/2019WR026348

[67] Miller, O., Solomon, D. K., Miège, C., Koenig, L., Forster, R., Schmerr, N., … Montgomery, L. (2018). Direct evidence of meltwater flow within a firn aquifer in southeast Greenland. *Geophysical Research Letters*, 45, 207–215. https://doi.org/10.1002/2017GL075707

[68] Miège, C., Forster, R. R., Brucker, L., Koenig, L. S., Solomon, D. K., Paden, J. D., et al. (2016). Spatial extent and temporal variability of Greenland firn aquifers detected by ground and airborne radars. Journal of Geophysical Research: Earth Surface, 121, 2381–2398. https://doi.org/10.1002/2016JF003869

[69] Chu, W., Schroeder, D. M., & Siegfried, M. R. (2018). Retrieval of englacial firn aquifer thickness from ice-penetrating radar sounding in southeastern Greenland. Geophysical Research Letters, 45, 11,770–11,778. https://doi.org/10.1029/2018GL079751

[70] Brangers, I., Lievens, H., Miège, C., Demuzere, M., Brucker, L., and De Lannoy, G. J. M.: Sentinel-1 detects firn aquifers in the Greenland ice sheet, Geophys. Res. Lett., 47, e2019GL085192, https://doi.org/10.1029/2019GL085192, 2020.

[71] D. Entekhabi et al., "The soil moisture active passive (SMAP) mission," Proc. IEEE, vol. 98, no. 5, pp. 704–716, May 2010.

[72] D. G. Long, M. Brodzik, and M. Hardman, "Enhanced resolution SMAP brightness temperature image products," IEEE Trans. Geosci. Remote Sens., vol. 57, no. 7, pp. 4151–4163, Jul. 2019.

[73] J. Z. Miller et al., "Brief communication: Mapping Greenland's perennial firn aquifers using enhanced-resolution L-band brightness temperature image time series," Cryosphere, vol. 14, no. 9, pp. 2809–2817, 2020.

[74] J. Z. Miller, R. Culberg, D. G. Long, and C. A. Christopher, D. M. Schroeder, and M. J. Brodzik, "An empirical algorithm to map perennial firn aquifers and ice slabs within the Greenland ice sheet using satellite L-band microwave radiometry," Cryosphere, vol. 16, no. 1, pp. 103–125, 2022.

[75] Sihvola, A. H. *Electromagnetic Mixing Formulas and Applications*. IEE. (1999).

[76]M. Garnett, J.C." Colours in the metal glasses and metal films," Trans of the Royal Society, Vol. CCIII, 1904, PP.385-420

[77] David Long; Fawwaz Ulaby et al., *Microwave Radar and Radiometric Remote Sensing*, Artech, 2015.

[78]Polder, D. and Van Saten, J.H."The effective permeability of mixtures of solids, Physica,1946, XII,(5), pp.257-271.

[79]De Loor, G.P.:" Dielectric properties of heterogeneous mixtures containing water," The Journal of Microwave Power, 1968, 3, pp.67-73

[80] Dobson, M. C., F. T. Ulaby, M. T. Hallikainen & M. A. El-Rayes (1985). Microwave Dielectric Behavior of Wet Soil-Part II: Dielectric Mixing Models. IEEE Transactions on Geoscience and Remote Sensing, 23(1), 35–46.

[81] V. L. Mironov, M. C. Dobson, V. H. Kaupp, S. A. Komarov, and V. N. Kleshchenko, "Generalized refractive mixing dielectric model for moist soils," in *IEEE Transactions on Geoscience and Remote Sensing*, vol. 42, no. 4, pp. 773-785, April 2004, doi: 10.1109/TGRS.2003.823288.

[82] Hallikainen, Martti, F. Ulaby, and Mohamed Abdelrazik. "Dielectric properties of snow in the 3 to 37 GHz range." *IEEE transactions on Antennas and Propagation* 34.11 (1986): 1329-1340.

[83] R. Lomonaco, M. Albert, and I. Baker, "Microstructural evolution of fine-grained layers through the firn column at Summit, Greenland," *Journal of Glaciology*, vol. 57, no. 204, pp. 755–762, 2011.

[84] Baker, Ian. "Microstructural characterization of snow, firn and ice." *Philosophical Transactions of the Royal Society A* 377, no. 2146 (2019): 20180162.

[85] K.H. Ding, X. Xu, and L. Tsang, "Electromagnetic Scattering by Bicontinuous Random Microstructures with Discrete Permittivities," *IEEE Trans. Geosci. Remote Sens.*, 48(8), 3139-3151, August 2010.

[86] Tsang, L., J. A. Kong, K. H. Ding and C.O.Ao, Scattering of Electromagnetic waves: Numerical Simulations, Wiley series in remote sensing, Wiley, 2001

[87] Andrews, M., Li, H., Johnson, J.T., Jezek, K.C., Bringer, A., Yardim, C., Chen, C.C., Belgiovane, D., Leuski, V., Durand, M., Duan, Y., Macelloni, G., Brogioni, M., Tan, S., Tsang, L., The Ultra-

Wideband Software-Defined Microwave Radiometer (UWBRAD) for Ice sheet subsurface temperature sensing: Calibration and campaign results, 2017 IEEE International Geoscience and Remote Sensing Symposium (IGARSS), Fort Worth, TX, USA, July 23-28, pp. 237-240, doi: 10.1109/IGARSS.2017.8126938., 2017

[88] Panzer, B., Leuschen, C., Patel, A., Markus, T., and Gogineni, S. Ultra-wideband radar measurements of snow thickness over sea ice 2010 IEEE International Geoscience and Remote Sensing Symposium, Honolulu, HI, USA, 25-30 July pp. 3130-3133, doi: 10.1109/IGARSS.2010.5654342. 2010

[89] Gelaro, R., McCarty, W., Suárez, M. J., Todling, R., Molod, A., Takacs, L., Randles, C. A., Darmenov, A., Bosilovich, M. G., Reichle, R., Wargan, K., Coy, L., Cullather, R., Koster, R., Luccheis, R., Merkova, D., Nielsen, J. e., Partyka, G., Pawson, S., Putman, W., Rienecker, M., Schuber, S. D., Sienkiewicz, M., and Zhao, B., The modern-era retrospective analysis for research and applications, version 2 (MERRA-2), J. Clim., Vol, 30, pp.5419–5454, https://doi.org/10.1175/JCLI-D-16-0758.1 2017

[90] Morris, E. M., and Wingham, D. J. The effect of fluctuations in surface density, accumulation, and compaction on elevation change rates along the EGIG line, central Greenland. J. Glaciology, vol., 57, no. 203. p. 416-430. https://doi.org/10.3189/002214311796905613 2011

[91] Baker, I., NEEM Firn Core 2009S2 Density and Permeability: https://arcticdata.io/catolog/view/doi:10.18739/A2Q88G, 2012

[92]Vallelonga, P Northeast Greenland Ice Stream (NEGIS) 2012 Ice Core Chemistry and Density https://www1.ncdc.noaa.gov/pub/data/paleo/icecore/greenland/negis2012dens.txt ,2016

[93] Matzler, C. Microwave permittivity of dry snow, IEEE Trans. Geosci. Remote Sens., vol. 34, no. 2, pp. 573–581, 10.1109/36.485133, 1996.

[94] Tiuri, M., Sihvola, A., Nyfors, E., and Hallikaiken, M., The complex dielectric constant of snow at microwave frequencies, IEEE J. Ocean. Eng., vol. 9, no. 5, pp. 377–382, Dec. 10.1109/JOE.1984.1145645 1984.

[95] Schaller, C. F., Freitag, J., Kipfstuhl, S., Laepple, T., Steen-Larsen, H. C., and Eisen, O.: A representative density profile of the North Greenland snowpack, The Cryosphere, vol,10, pp.1991–2002, https://doi.org/10.5194/tc-10-1991-2016, 2016

[96] Brogioni, M., Macelloni, G., Montomoli, F., and Jezek, K.C., Simulating Multifrequency Ground-Based Radiometric Measurements at Dome C—Antarctica, IEEE Journal of Selected Topics in Applied Earth Observations and Remote Sensing, vol. 8, no. 9, pp. 4405-4417, doi: 10.1109/JSTARS.2015.2427512. 2015

[97] Leduc-Leballeur., M. Picard, G., Mialon, Arnaud., Arnaud, L., Lefebvre, E., Possenti, P., and Kerr, Y., Modeling L-Band Brightness Temperature at Dome C in Antarctica and Comparison With SMOS Observations, IEEE Transactions on Geoscience and Remote Sensing, vol. 53, no. 7, pp. 4022-4032, , doi: 10.1109/TGRS.2015.2388790. 2015

[98] Bringer, A., Miller, J., Johnson, J. T., and Jezek, K. C.: Radiative transfer modeling of the brightness temperature signatures of firn aquifers, American Geophysical Union Fall Meeting, New Orleans, LA, USA, https://agu.confex.com/agu/fm17/meetingapp.cgi/Paper/283159, 11–15 December 2017.

[99] Jin, Jian-Ming. *The finite element method in electromagnetics*. John Wiley & Sons, 2015.

[100] R. C. Rumpf, "Simple implementation of arbitrarily shaped total-field/scattered-field regions in finite-difference frequency-domain," Progress In Electromagnetics Research B, vol. 36, no. 36, pp. 221–248,2011.

[101] ANSYS HFSS software. http://www.ansoft.com/products/hf/hfss/

[102] Landau, L. D., E. M. Lifshitz, J. B. Sykes, J. S. Bell & M. J. Kearsley (1975). *Electrodynamics of Continuous Media*. New York: Pergamon Press.

[103] S. Tan, J. Zhu, L. Tsang, and S. V. Nghiem, "Microwave Signatures of Snow Cover Using Numerical Maxwell Equations Based on Discrete Dipole Approximation in Bicontinuous Media and Half-Space Dyadic Green's Function," in *IEEE Journal of Selected Topics in Applied Earth Observations and Remote Sensing*, vol. 10, no. 11, pp. 4686-4702, Nov. 2017, doi: 10.1109/JSTARS.2017.2703602.

[104] Fausto, R. S., Box, J. E., Vandecrux, B., Van As, D., Steffen, K., MacFerrin, M. J., Machguth, H., Colgan, W., Koenig, L. S., McGrath, D. Charalampidis, C., and Braithwaite, R. J., A snow density dataset for improving surface boundary conditions in Greenland ice sheet firn modeling, Front. Earth Sci., vol. 6, https://doi.org/10.3389/feart.2018.00051, 2018.